Title	Environmental Transmission Electron Microscopy Studies on Morphology of Catalytically Active Supported Gold Nanoparticles
Author(s)	内山, 徹也
Citation	大阪大学, 2016, 博士論文
Version Type	VoR
URL	https://doi.org/10.18910/59619
rights	
Note	

Doctoral Dissertation

Environmental Transmission Electron Microscopy Studies on Morphology of Catalytically Active Supported Gold Nanoparticles

Tetsuya Uchiyama

July 2016

Graduate School of Engineering

Osaka University

Abstract

This dissertation presents experimental studies on morphology of catalytically active supported gold nanoparticles by means of environmental transmission electron microscopy (ETEM).

Background and overview of this dissertation are explained in chapter 1. Metal nanoparticle catalysts are explained in chapter 2. The history of ETEM and review of the study of catalysts using ETEM are shown in chapter 3.

For accurate ETEM observations, influence of electron irradiation on Au nanoparticles (AuNPs) and CeO_2 support and sample contaminations from CO-rich gas are examined in chapter 4 and 5. ETEM observations and electron energy loss spectroscopy (EELS) measurements in vacuum, O_2 and CO/air have shown that electron beam gives little influence on AuNPs and CeO_2 support when the electron beam flux is smaller that 5 A/cm^2. Additionally, desorptions of CO molecules from the surface of AuNPs by electron beam are estimated. From the estimations, CO molecules are most likely adsorbed at the surface of AuNPs under 5 A/ cm^2 electron flux. From these results, it is concluded that proper flux in ETEM observations is smaller than 5 A/ cm^2. In chapter 5, sample contaminations from CO-rich gas are examined. It is known that CO gas of high pressure reacts with the inside wall of cylinders and gas supply lines, forming corrosive products (CPs). These CPs may be mixed within the gas being delivered to the ETEM and decomposed by electron irradiation in the ETEM, forming contamination on samples. After examining the contamination process by ETEM, it is

demonstrated that gas purification is crucially important to observe intrinsic phenomena in CO-rich gases by ETEM and thus to improve the accuracy of ETEM experiments.

In chapter 6, systematic ETEM observations of active Au/CeO$_2$ catalysts in various partial pressures of CO and O$_2$ are carried out for the first time. Morphology of AuNPs on CeO$_2$ changes depending on partial pressure of CO and O$_2$ gases. Establishing morphology diagram, we have concluded that 1) CO molecules are adsorbed on the surface of AuNPs, stabilizing AuNPs of polyhedral shape enclosed by the major {111} and {100} facet surfaces, 2) O$_2$ molecules possibly dissociate into O atoms, resulting in round morphology of AuNPs.

In chapter 7, to examine whether AuNPs behavior in gases differ depending on support materials and catalytic activity, ETEM observations of AuNPs on CeO$_2$, SiO$_2$, TiC supports, which is known as reducible oxide, irreducible oxide and carbide respectively, in O$_2$ and CO/air were carried out. ETEM observations of AuNPs on the support in O$_2$ and CO/air have shown the tendency that morphology changes of AuNPs differ depending on support materials. The ratio of AuNPs which show round morphology in O$_2$ and facet morphology in CO/air tends to high in highly active catalysts. On the other hand, the ratio tends to low in low active catalysts. Round morphology in O$_2$ possibly correlates to O atoms adsorptions on AuNP surface. It is considerable from these results that not all AuNPs but parts of AuNPs contribute to catalytic reactions, and the ratio of AuNPs which take part in catalytic reactions affects catalytic activity. Interfacial structure of AuNPs and supports possibly relate to the

ratio.

In chapter 8, considering our experimental results shown in chapter 6 and 7 and previous reports, CO oxidation reaction mechanism of Au catalysts is discussed in terms of adsorptions of CO and O_2 molecules, dissociations of O_2 molecules.

Application of ETEM to understanding the growth mechanism of carbon nanotubes (CNTs) is shown in chapter 9. ETEM observations clearly showed that (1) nanoparticle catalysts (NPCs) are fluctuating crystalline nanoparticles, (2) the NPCs are cementite Fe_3C and (3) carbon atoms migrate through NPC bulk and (4) nucleation of inactive iron silicate was suppressed by Mo addition, resulting in increase in CNTs yield.

Our observations will induce further experiments and computer simulations to elucidate the reaction mechanism of Au catalysts. Furthermore, we have shown an effective approach of the ETEM to study the reaction mechanism of metal nanoparticle catalysts. We are convinced that this work stimulates the study to reveal various solid-gas reactions at atomic scale.

Acknowledgement

Finally, I would like to express my sincere gratitude to my family and friends. In particular, my parents and my wife have helped me in all respects.

Contents

x

Chapter 1

General introduction

1.1 Background

Environment around human beings has greatly changed by scarce of resources and global warming. Human beings stand at a critical junction to develop industries in a different manner. It is desired to minimize the influence to the ecological system in the cycle of manufactures and disposal of chemical products. To accomplish this, low environmental load and high efficiency chemical processes are required. Especially, in environmental purification, energy and electric device fields which strongly affect the environment of the earth, expectations to metal catalysts have risen. For example, Pt has been used in fuel cells and as exhaust gas catalysts [1–4]. Fe-Cr catalysts and Cu-Zn catalysts show high catalytic activity in water-gas shift reactions [5] which is very important in hydrogen productions for fuel cells. Fe, Ni and Co show high catalytic activity in the growth of carbon nanotubes (CNTs) [6,7] which is expected to future nanostructure materials of devices. Recently, Au nanoparticle catalysts gather much attention among metal catalysts. The property of Au nanoparticles (AuNPs) is quite different from that of bulk gold (Fig.1.1). For example, the melting point of AuNPs is lower than that of bulk (size effect) [8]. Bulk gold shows diamagnetism. On the other hand, the surface of AuNPs shows ferromagnetism and inside of AuNPs shows

paramagnetism [9]. Unlike bulk gold, AuNPs illuminate [10]. AuNPs show high catalytic activity in chemical reactions [11] and work as catalysts in the growth of nanostructure materials such as CNTs [12] and silicon nanowires (SiNWs) [13].
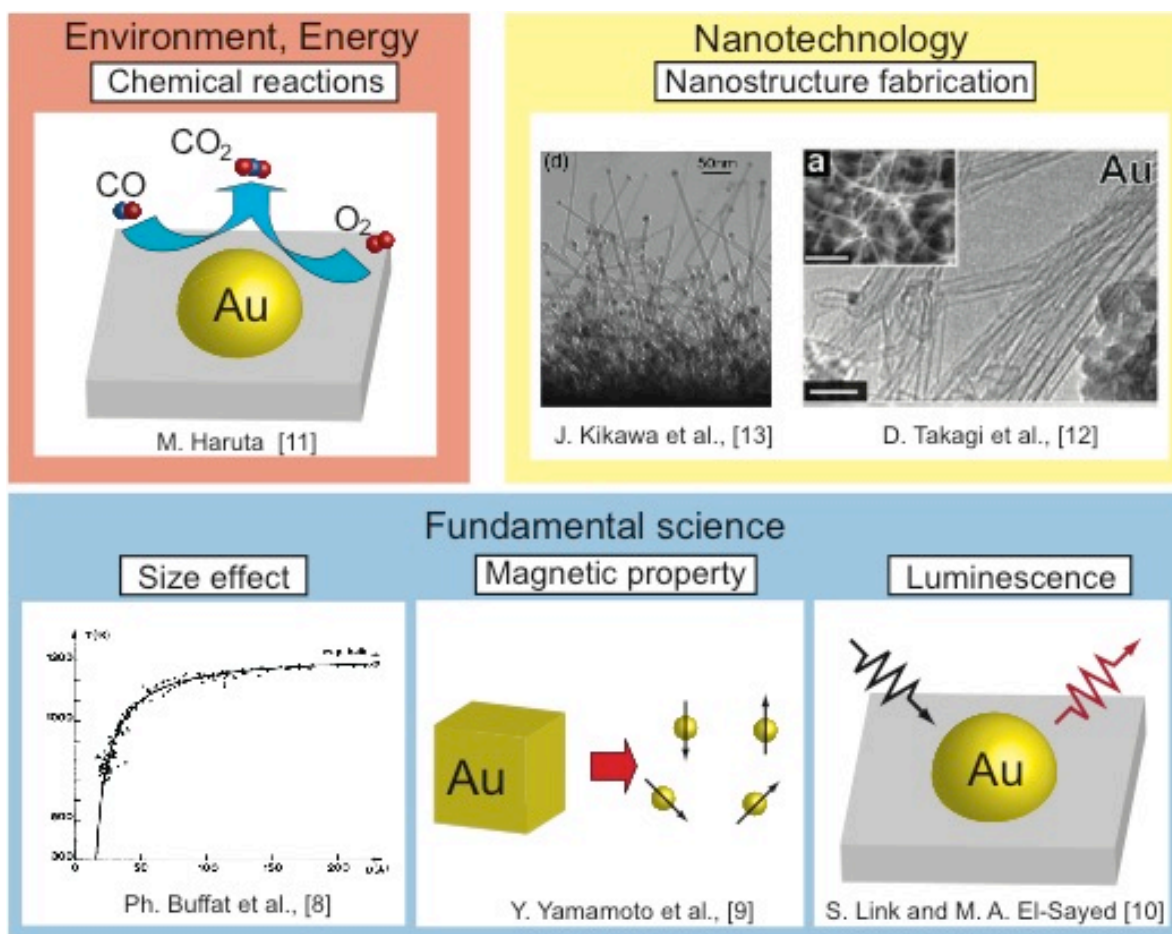
Figure 1.1: Various properties of AuNPs. In fundamental science such as environment, energy and nanotechnology regions, much attention is paid to AuNPs.

Among various properties of AuNPs, our group especially pays much attention to solid-gas reactions. Among solid-gas reactions

of AuNPs, we focus on CO oxidation reaction which gathers attention from environmental purification and energy fields. The reactions between AuNPs and gases are explained in more detail below. Additionally, missing piece of the puzzle and problems of conventional experimental method in studying the reactions will be explained.

Unlike bulk gold, AuNPs on metal oxide show high catalytic activity in many kinds of reaction [14]. For example, AuNPs supported on CeO_2 show high catalytic activity in CO oxidation and water-gas shift reaction [15-17]. AuNPs on TiO_2 show high catalytic activity in direct epoxidation of propylene [18]. Current industrial processes for epoxidation of propylene need two-stage reactions. Arisings created in the processes came to an issue. If Au/TiO_2 catalysts are put into practical use in chemical industries, they will contribute to the realization of a low environment load and continued growth society. As we mentioned, catalysts, especially metal nanoparticle catalysts, gather a lot of expectations from environmental purification, energy and electric device fields.

Transmission electron microscopy (TEM), scanning tunneling microscopy (STM), photoemission electron microscopy (PEEM) and infrared spectroscopy (IR) are used in the study of catalysts. These methods achieved significant results in the study of Pt catalysts [19,20]. As adsorptions and reactions of gases occur at the surface of Pt catalysts, the reaction mechanism has been revealed successfully by combining these methods. However, it is difficult to clarify the reaction mechanism of all metal catalysts just using same methods. When reactions occur not on the whole surface but

at the local domain of metal catalysts, it is essential to observe the reactions between metal catalysts and gases with high spatial resolution and high temporal resolution. Recently, environmental TEM (ETEM) [21–30] has been developed. This is a special TEM which is possible to introduce gas into it. Using differential pumping system, only surrounds of a specimen is high pressure and other regions are high vacuum. Therefore, we can observe solid-gas reactions with high spatial resolution in real time. ETEM has been used in in situ observations of the growth of CNT and solid-gas reactions of catalysts. For example, Helveg *et al*. observed the growth of a carbon nanofiber (CNF) from a Ni nanoparticle in CH_4 [23]. Yoshida *et al*. observed the growth of multi-walled carbon nanotubes (MWNT) from Fe nanoparticles. They clarified that Fe nanoparticles become Fe_3C in the creation of MWNTs [28]. In the study of catalysts, Hansen *et al*. observed Cu nanoparticles on ZnO in H_2, H_2-H_2O mixture and H_2-CO mixture [29]. Giorgio observed AuNPs on TiO_2 and Pd nanoparticles on TiO_2 in H_2 and O_2 [30]. However, they only calculated surface and interface energies from equilibrium shapes of metal nanoparticles. They did not observe metal nanoparticles in reaction condition. They could not relate ETEM images to the reaction mechanism.

In this dissertation, we studied morphology of AuNPs on various support materials in CO oxidation reaction and discussed the reaction mechanism. Au catalysts are expected as a newly developed catalysts relating with environmental purification and energy fields. Features of Au catalysts are explained in more depth below.

Catalytic activity of Au catalysts depend both on AuNP size and support materials. Three models about reaction mechanism of CO oxidation are proposed (Fig.1.2) [11,31-34]. (1) Perimeter interface between a AuNP and the support is active site (Fig.1.2 (a)) [11]. (2) Au cations induce reactions (Fig.1.2 (b)) [31, 32]. (3) Non metallic nature of Au two layers relates with the reaction mechanism (Fig.1.2(c)) [33, 34]. However, there is argumentation on the reaction mechanism. The reaction mechanism, i.e. where are adsorption sites, where are active sites and how adsorbed molecules react, is not clarified yet. To understand the reaction mechanism, ETEM observation of Au catalyst in reaction conditions is a useful method. To investigate AuNPs behavior in CO oxidation, we carried out systematic ETEM observations of morphology of AuNPs in various partial pressure of CO and O_2 for the first time. Additionally, to investigate support effect on catalytic activities of Au catalysts, ETEM observations of AuNPs on CeO_2, SiO_2, TiC supports, which is known as reducible oxide, irreducible oxide and carbide respectively, in O_2 and CO/air were carried out.
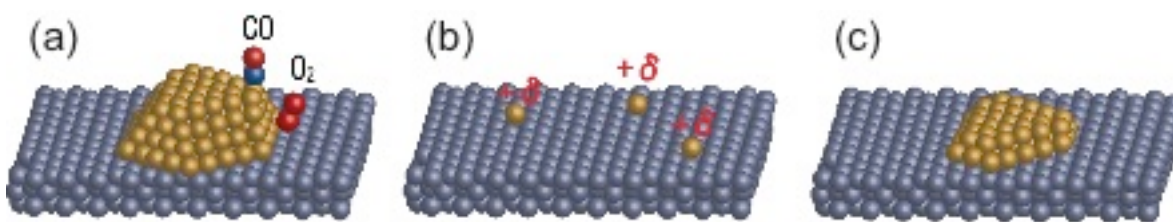
Figure 1.2: Reaction models. (a) Perimeter interface model [11], (b) Au cation model [31,32] and (c) Two layers model [33,34].

1.2 Overview

First, metal nanoparticle catalysts are explained in chapter 2. The history of ETEM and review of the study of catalysts using ETEM are shown in chapter 3.

In chapters 4 and 5, precautions for ETEM observations are described. The influence of electron beam on AuNPs and CeO_2 support is shown in chapter 4. Desorptions of CO and O_2 molecules from the surface of AuNPs by electron irradiation are also estimated. From the results and the estimation, proper flux of electron beam for observations is discussed. In chapter 5, sample contaminations from CO-rich gases are examined. It is demonstrate that gas purification is crucially important to observe intrinsic phenomena in CO-rich gases by ETEM and thus to improve the accuracy of ETEM experiments.

Chapter 6 presents the results of in situ observations of active Au/CeO_2 in CO/air, air, O_2 and N_2. AuNPs change their shape depending on gas species. Systematic observations in various ratio of CO and O_2 partial pressure are also carried out. Morphology diagram of AuNPs with respect to partial pressure of CO and O_2 is examined for the first time. In chapter 7, AuNPs on CeO_2, SiO_2, TiC supports are observed in O_2 and CO/air by means of ETEM. Comparing morphology of AuNPs on each support, the origin of support effects on the catalytic activities of Au catalysts is discussed. In chapter 8, the mechanism of CO oxidation of Au catalysts is discussed considering experimental results shown in chapter 6 and 7 and previous studies.

Chapter 9 presents the application of ETEM to understanding the growth mechanism of CNTs from nanoparticles catalysts (NPCs). ETEM observations clearly showed that NPCs are fluctuating crystalline Fe_3C nanoparticles.

In chapter 10, my dissertation is summarized.

Chapter 2

Metal nanoparticle catalysts

As we mentioned in chapter 1, metal nanoparticle catalysts show high catalytic activity in various reactions. In this chapter, we will explain how metal nanoparticle catalysts are used in society. Nowadays, among metal nanoparticle catalysts, Au catalysts are getting a lot of attentions for their special characteristics. We will also explain Au catalysts from the point of view of their history and properties. Then, we focus on low temperature CO oxidation reaction of Au catalysts which is a specific feature of them. In the end of this chapter, we list up missing piece of puzzle of the reaction mechanism of CO oxidation of Au catalysts.

2.1 Metal nanoparticle catalysts used in industries

Now, we explain how the metal nanoparticle catalysts are used in society. They are used in environmental purification, energy and electronic device regions (Fig.2.1).

2.1.1 Environmental purification

Typical catalysts for environmental purification are three-way catalysts. Three-way catalysts consist of Pt, Rh and Pd nanoparticles supported on CeO_2 and Al_2O_3 monolith [1, 2].
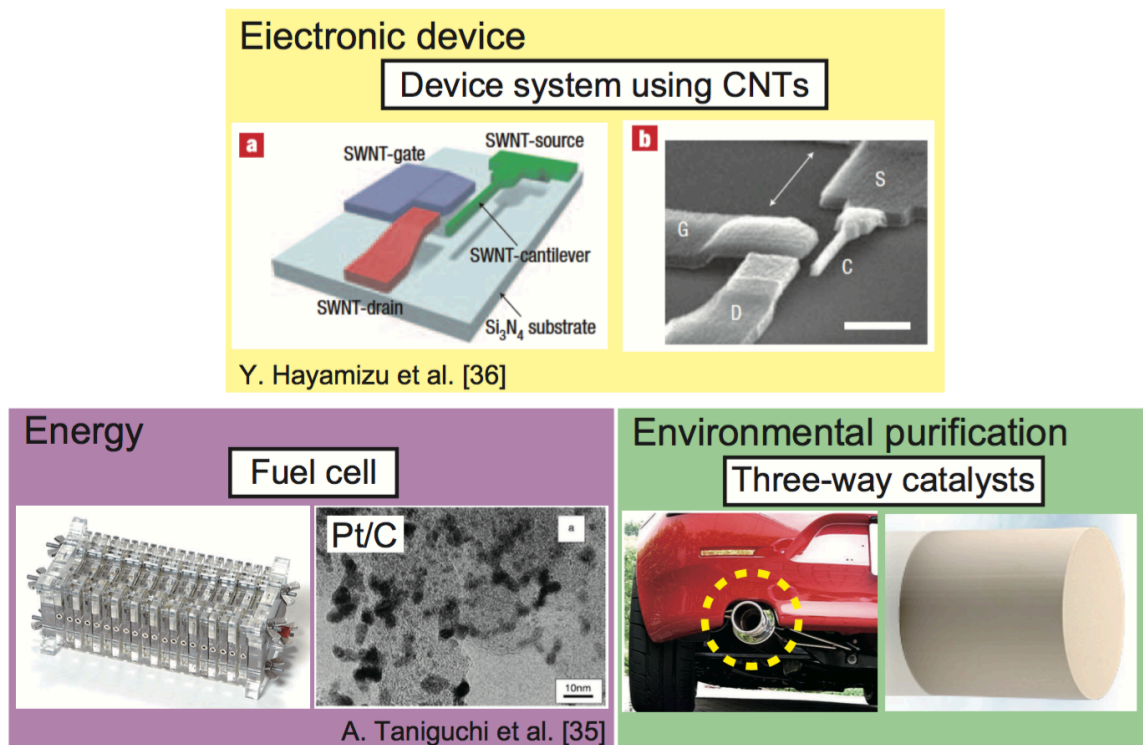
Figure 2.1: Examples of usage of metal nanoparticle catalysts in society.

Three-way catalysts are used to render vehicle emission harmless. Three reactions proceed at the same time in three-way catalysts. 1. Reduction of NO_x to N_2 and O_2. 2. Oxidation of CO to CO_2. 3. Oxidation of HC to CO_2 and H_2O. Other metal nanoparticle catalysts used for environmental purification are Au catalysts. They decompose trimethylamine which causes foul smell.

2.1.2 Energy

New technologies to generate energy have been sought concerning about running out of oil in the future. Nowadays, fuel cell gathers much attention [3,4,35]. A fuel cell is some kinds of generator. In a fuel cell, a fuel source is converted into an electric current via an electro-chemical process. Fuel cell is made up of three segments i.e. anode, cathode and electrolyte. Pt nanoparticles are used in both anode and cathode. H_2 and an oxidant react at anode, cathode and generates electricity inside a cell.

In fuel cells, H_2 molecules are used as a fuel. Currently, H_2 molecules are made by conversions of hydrocarbon gases. However, CO molecules are also involved in this conversion processes. It is well known that CO inactivates Pt catalysts. To avoid deactivation, water-gas shift reactions are used. CO molecules react with H_2O molecules selectively in CO, H_2 and H_2O mixture, resulting in CO_2 and H_2 production. Cu-Zn catalysts show catalytic activity in water-gas shift reaction [5]. Recently, it has been reported that Au catalysts also show high catalytic activity in water-gas shift reaction [17].

2.1.3 Electronic devices

To develop electronic devices, minimizing electronic circuits is needed. There are two different techniques for nanodevices fabrications. One of them is the 'top-down' technique, i.e. lithographies. Block material is whittled away with electron beam to desired shape. The other is the 'bottom-up' approach, which is a

self-assembled growth of materials. CNTs and SiNWs are expected as nano components for 'bottom-up' process. SiNWs grow from AuNP catalysts. CNTs grow from Fe, Co and Ni nanoparticle catalysts. Recently, growth of CNTs from AuNP catalysts has been reported [12]. For electronic devices, hierarchically assembling CNTs into closely packed and highly aligned three-dimensional wafer films were lithographically fabricated from three-dimensional nanotube structures [36].

2.2 Pt catalysts

Various materials show catalytic activity in catalytic reactions. In these catalysts, Pt catalyst is one of the most important catalysts in industry. Both Pt catalysts and Au catalysts show catalytic activity in CO oxidation. In this section, details about CO oxidation of Pt catalysts are explained.

2.2.1 CO oxidation at the surface of Pt

CO oxidation proceeds as follows. Here, CO(a), O(a) and S represent an adsorbed CO molecule, an adsorbed O atom and an adsorption site on Pt surface. Fig. 2.2(a), (b) show schematic illustration of the reaction and energy profile [37]. It is well known that CO molecules are adsorbed as molecular state. On the other hand, O_2 molecules dissociate into O atoms in adsorption. The reaction mechanism of adsorbed species is called as

$$CO + S \; \rightleftharpoons \; CO(a) \qquad\qquad (1)$$
$$O_2 + 2S \; \rightleftharpoons \; 2O(a) \qquad\qquad (2)$$
$$CO(a) + O(a) \; \longrightarrow \; CO_2 + 2S \qquad\qquad (3)$$
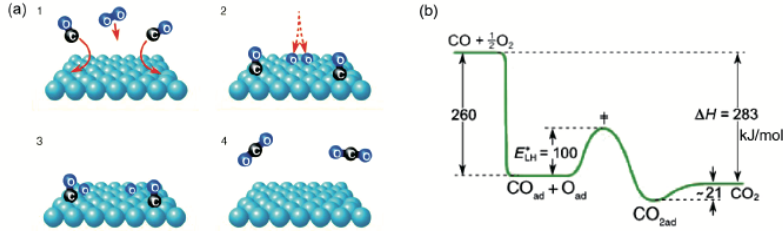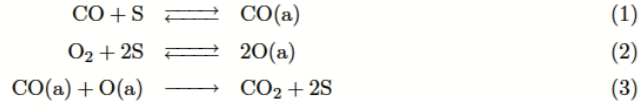
Figure 2.2: Schematic illustration of CO oxidation and energy profile on Pt [37].

Langmuir-Hinshelwood mechanism. Fig. 2.3(a) shows ordered structure of Pt (111) surface with CO coverage θ_{CO} =0.75 [38]. CO molecules are adsorbed at on-top site and bridge site of Pt surface and become c(4 x 2) structure. As coverage of CO molecules is high, O atoms cannot be adsorbed at the surface. After raising temperature up to 227 ℃, CO molecules desorb from the surface and O atoms can be adsorbed at the surface.

The adsorptions of O atoms are quite different from those of CO molecules. As shown in Fig. 2.3(b), when O coverage θ_O =0.25, O atoms are adsorbed at threefold coordinated sites and become (2 x 2) structure. Additional O atoms cannot be adsorbed at the surface [38]. On the other hand, CO molecules are possibly adsorbed at on-top sites. As a result, mixed phase shown in Fig. 2.3(c) is created [38].

Wintterlin *et al.* examined reaction mechanism of CO oxidation at the surface of Pt(111) model catalysts using STM [20]. Their results are summarized as follows. They first covered the sample with submonolayers of oxygen atoms, resulting in appearance of island of the (2 x 2) structure of chemisorbed O atoms on Pt(111). After that, CO gas was introduced. As reaction proceeded, the area of the (2 x 2) structure began to decrease and c(4 x 2) CO structure appeared and grew. They suggested that the reaction proceed at the frontiers between the (2 x 2) and the c(4 x 2) CO regions.

c(4x2) – CO   2x2 – O   2x2 – O + CO
(a)   (b)   (c)
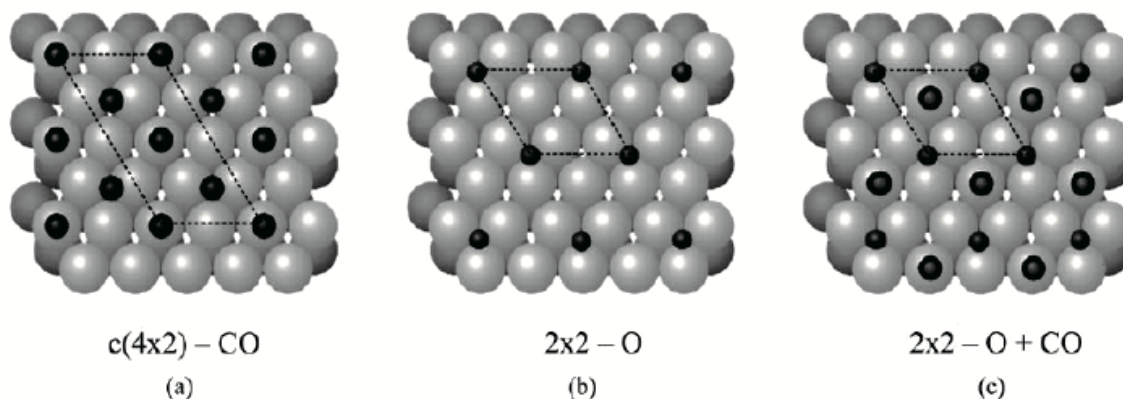
Figure 2.3: Ordered structure created on Pt (111) surface caused by adsorptions of CO molecules and O atoms [38].
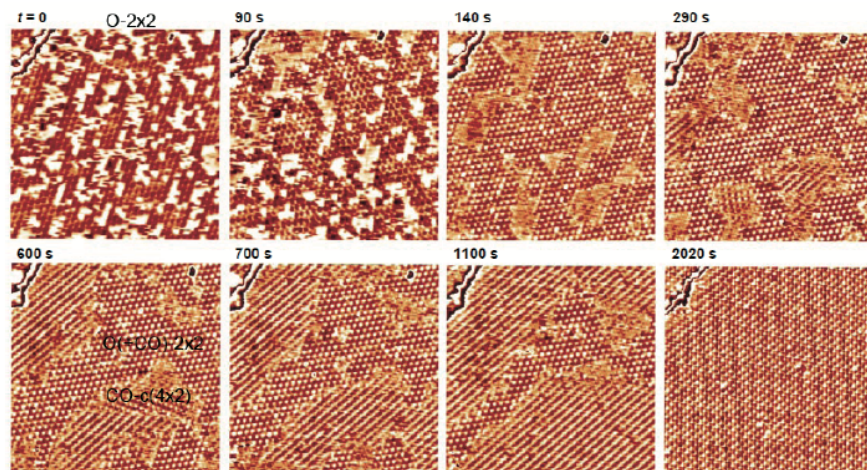
Figure 2.4: STM images acquired during reaction of adsorbed oxygen atoms with CO molecules on a Pt(111) surface. Image size is 18 nm x 17 nm. T=-26 ℃, P_{CO}=5 x 10^{-8} mbar [20].

2.3 Au catalysts

The properties of AuNPs are quite different from those of bulk gold. For example, the melting temperature of AuNPs is lower than bulk gold. Furthermore, Au catalysts show catalytic activity in various reactions. In this section, first, the specific properties of Au nanoparticle are shown. Then, brief history of Au catalysts and reaction mechanism of CO oxidation are introduced.

2.3.1 Properties of Au nanoparticle

Metal nanoparticles show some kinds of structures inhibited in the crystallographic translational-symmetry rules [39]. AuNPs tend to become fcc (truncated octahedron) structure. However, AuNPs change their shape depending on their size and temperature. Koga *et al*. have studied structural stability of AuNPs in relation to both size and temperature systematically [40]. Iijima *et al*. examined

the stability of AuNPs and reported dynamic behavior of AuNPs around 2 nm in size was observed at the level of atomic resolution by TEM [41]. The shape of the particles changed continually during the observations.

AuNPs show various properties which are quite different from bulk one. Buffat *et al*. have employed a scanning electron diffraction technique to deduce the melting temperature of AuNPs in the range of particle size greater than 2nm. They showed that the melting point of AuNPs is lower than that of bulk (size effect) [8]. Using element-specific magnetization (ESM) measurements, Yamamoto *et al*. reported the intrinsic magnetic polarization in AuNPs which is different from bulk one [9]. Link *et al*. reported that optical absorption spectra of AuNPs in colloidal solution changes depending on the size and shape of AuNPs[10].

In addition, AuNPs show high catalytic activity in chemical reactions [11] and work as catalysts in the growth of nanostructure materials such as CNTs [12] and SiNWs [13]. Catalytic activities of AuNPs will be described more precisely in the next section.

2.3.2 Brief history of Au catalysts

Brief history of Au catalysts is shown in Table 2.1. The clue that Au dispersed as small nanoparticles may show catalytic activity was presented by Bond and Sermon for oxygen and hydrogen transfer reactions over Au/MgO and Au/Al$_2$O$_3$ catalysts [42,43] and for hydrogenation over Au/SiO$_2$ and by Paravano *et al*. [44,45].

15

Haruta *et al*. found in 1983 that AuNPs on selected metal oxides show surprisingly high catalytic activity for CO oxidation, even at -73 ℃ [14]. This finding has motivated further work on Au catalysts.

Au catalysts show high catalytic activity in various reactions. Hayashi *et al*. reported the direct epoxidation of propylene over Au/anatase-TiO_2 [46]. The direct epoxidation of propylene is very important in chemical industries because current processes need two-stage reactions accompanying arisings. Au catalysts also show catalytic activity in selective oxidation of D-glucose to D-gluconic acid [47] and water-gas shift reaction [17]. AuNPs on TiO_2, Fe_2O_3, ZnO and $ZnFe_2O_4$ was found to be active for the hydrogenation of both carbon dioxide and carbon monoxide [14]. Especially, Au/ZnO and Au/$ZnFe_2O_4$ performed high methanol selectivity from carbon dioxide. Okumura *et al*. reported direct synthesis of H_2O_2 from O_2 and H_2 [48].

2.3.3 Reaction mechanism of CO oxidation

Many researchers have examined the reaction mechanism of CO oxidation of Au catalysts. Things to be solved are as follows.

1. Adsorption sites of CO molecules

2. Adsorption sites of O_2 molecules

3. O_2 molecules dissociate into O atoms in adsorption

4. Active sites

5. Charge transfer

6. O vacancies

Both experimental results and calculation results support that adsorption sites of CO molecules are edges and corners of AuNPs. However, the other things are under discussion. To clarify reaction mechanism of Au catalysts, we observed Au catalysts in CO/air and other kinds of gases. ETEM observations are shown in Chapter 7 and 8. Then, we will discuss reaction mechanism considering experimental results and three models in chapter 9.

Table 2.1: Brief history of Au catalyststs.

Year	Researchers [References]	Discovery
1970	D. Y. Cha *et al.* [44]	Hydrogenation reaction over Au/SiO_2
1973	G. Bond *et al.* [42,43]	Oxygen and hydrogen transfer reaction over Au/MgO and Au/Al_2O_3
1983	M. Haruta *et al.* [14]	CO oxidation over Au/Fe_2O_3, Au/Co_3O_4 and Au/NiO
1995	W. Liu *et al.* [17]	Water-gas shift reaction over Au/CeO_2
1998	T. Hayashi *et al.* [46]	The direct epoxidation of propylen over $Au/anatase-TiO_2$
1998	M. Valden *et al.* [49]	Two layers model
2002	M. Haruta *et al.* [11]	Perimeter model
2002	S. Biella *et al.* [47]	Selective oxidation of D-glucose to D-gluconic acid
2003	M. Okumura *et al.* [48]	Direct synthesis of H_2O_2 from O_2 and H_2
2003	Q. Fu *et al.* [16]	Au cation model

Chapter 3

History of Environmental Transmission Electron Microscopy (ETEM)

TEM is a useful method to observe various materials at atomic scale in vacuum. Morphology and structure of materials and defects in them have been observed using TEM. Using specific specimen holders, we can heat up and cool down specimen. In addition to a high spatial resolution, TEM has a high temporal resolution, which enables us to observe dynamic behavior of reactions. For example, dynamic behavior of defects in crystal induced by electron irradiation was observed in situ. However, as industrial materials are fabricated and used in gas or liquid environment, demands to observe specimens in gas and liquid are growing. To satisfy these requirements, ETEM has been developed. Recently, the shape change of metal nanoparticle catalysts in gas [29,30] and the growth process of carbon nanofiber and CNT [23,28] are observed using ETEM. Much attention is paid to ETEM from nanotechnology, material science and environment-energy field. In this chapter, first, we will explain E-cell which is very important to keep inside of the column high vacuum and space around specimen high pressure. Then, we will review the studies on catalysts using ETEM briefly.

3.1 Type of E-cell

Two types of E-cell, i.e. the window type and the aperture type, have been developed. The window type consists of two electron transparent windows placed above and below the specimen (Fig. 3.1(a)). These windows prevent the gas from diffusing to the column. Disadvantage of the window type is scattering of electron beam by the windows, resulting in decrease in resolution. The aperture type consists of two apertures placed above and below the specimen (Fig. 3.1(b)). These apertures prevent the gas from diffusing to the column. Electron beam go through holes of the apertures. Therefore, there is little decrease in resolution unlike the window type. However, there is a leakage of gas from the holes of the apertures. Evacuating the leakage gas and keep the column high vacuum are desirable. For this aim, the differentially pumped aperture type has been developed (Fig.3.1(c)). Using additional turbo molecular pumps, the leakage gas is evacuated, which leads to improvement of degree of column vacuum.
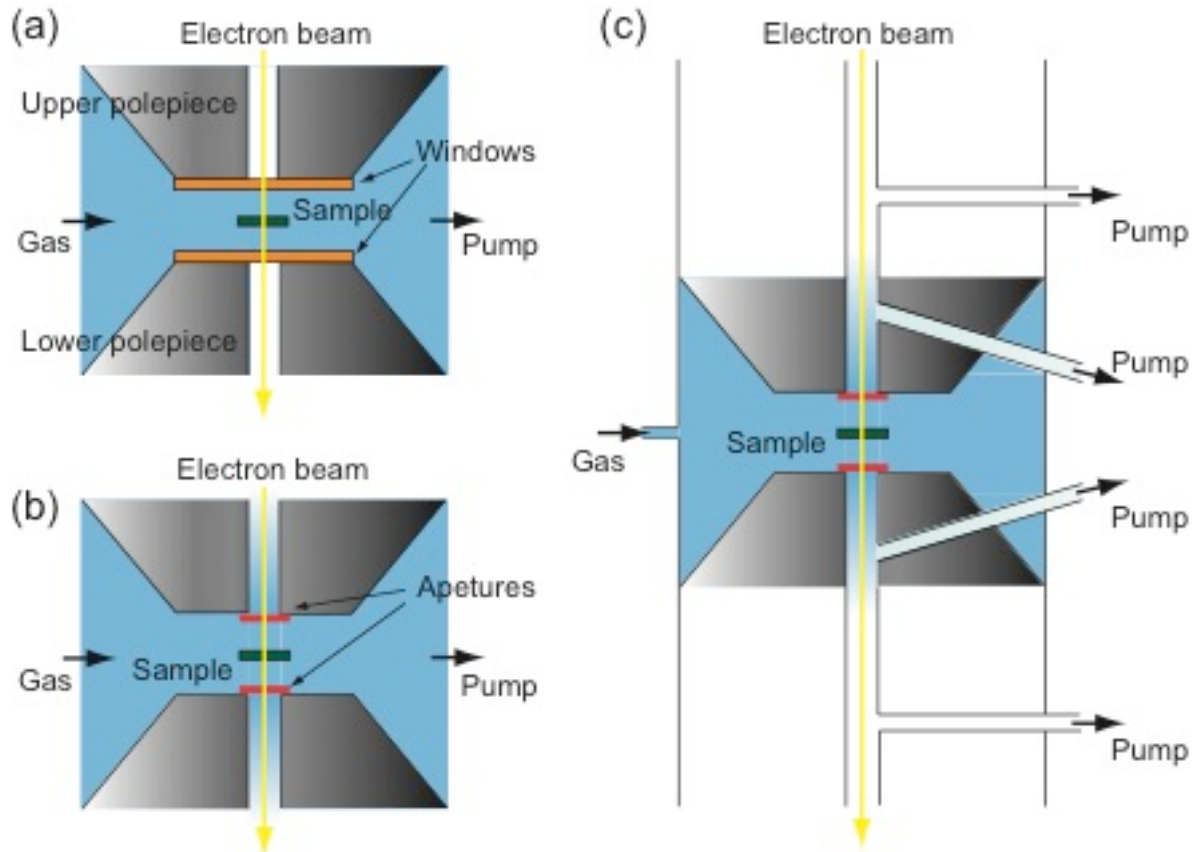
Figure 3.1: (a) the window type, (b) the aperture type and (c) the differentially pumped aperture type of E-cell.

3.2 Brief review of the studies on catalysts using ETEM

Hansen *et al*. have observed Ba-promoted Ru catalysts in H_2-N_2 mixture of 5.2 mbar at atomic resolution [22]. Ba-Ru catalysts show catalytic activity in ammonia synthesis reactions. Ru nanoparticles are covered with BN a few layers in vacuum. In

the mixture of H_2:N_2 =3:1 of 5.2 mbar at 552 °C, surface of Ru nanoparticles are covered with amorphous layers which contain Ba (Fig. 3.2(a)). Moreover, a monolayer of barium oxide exists at the edge of Ru nanoparticles (Fig. 3.2(b)). However, the factor that Ba promotes catalytic activity has not been clarified yet. Hansen *et al*. observed Cu clusters supported on ZnO in H_2, H_2-H_2O mixture and H_2-CO mixture [29]. Cu/ZnO catalysts show high catalytic activity in metanol synthesis and conversion of hydrocarbons and alcohols for fuel cells. Cu nanoparticles changed their shape depending on atmosphere (Fig. 3.3). They examined surface and interface energy from the equilibrium shape of Cu nanoparticles. Yoshida *et al*. investigated the morphology of Pt nanoparticles supported on CeO_2 in CO oxidation reaction using ETEM [50]. Pt nanoparticles in CO/air showed round morphology at room temperature, while they become partially faceted morphology at 100 ºC (Fig. 3.4). Based on the observations, they proposed that the morphology change of the Pt nanoparticles is induced by adsorptions of CO molecules and O atoms. Giorgio *et al*. observed Au clusters supported on TiO_2 and amorphous carbon and Pd clusters supported on TiO_2 in H_2 and O_2 (Fig. 3.5) [30]. They also observed Au/amorphous carbon in H_2 and O_2 and Au/TiO_2 in H_2, O_2 and CO/air (Fig. 3.6) [51]. AuNPs on amorphous carbon show (111) and (100) planes in H_2 of 2 mbar clearly. On the other hand, they become round in O_2 of 2 mbar. They observed Au/TiO_2 in vacuum, H_2 and O_2 of 2 mbar. AuNPs show facets in vacuum and H_2 and become round in O_2. They accounted for the reason of the morphology change in O_2 that the oxygen interacts with the outer surface including low coordinate

sites like edges and steps. They also observed Au/TiO$_2$ in CO/air of 4 mbar. They reported that AuNPs became round in CO/air. However, there was no ETEM image of Au/TiO$_2$ in CO/air. From these results, they concluded that the shape evolution in reaction condition is a key factor in the CO oxidation. Kuwauchi *et al*. examined electron irradiation effect on a Au/TiO$_2$ catalyst systematically (Fig. 3.7) [52]. They revealed the intrinsic structure of Au/TiO$_2$ catalysts. Under reaction conditions i.e. CO/air 1 mbar, gold nanoparticles show the major {111} and {100} facets.
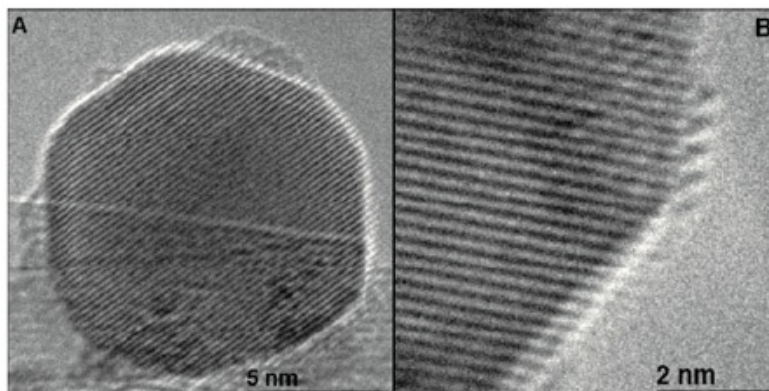
Figure 3.2: ETEM images of a Ba-promoted Ru catalyst observed at 552 °C and 5.2 mbar in H$_2$/N$_2$ mixture [22].
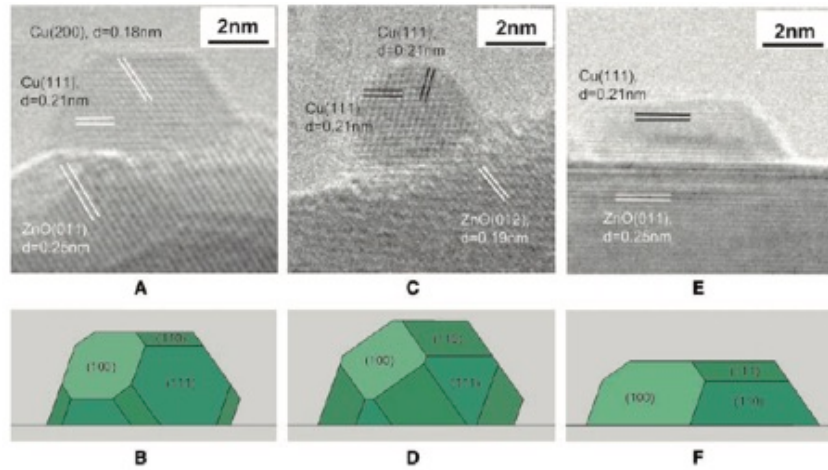
Figure 3.3: ETEM images of a Cu/ZnO catalyst in various gas (A, C and E) and corresponding Wulff constructions of the Cu nanoparticles (B, D and F) [29].
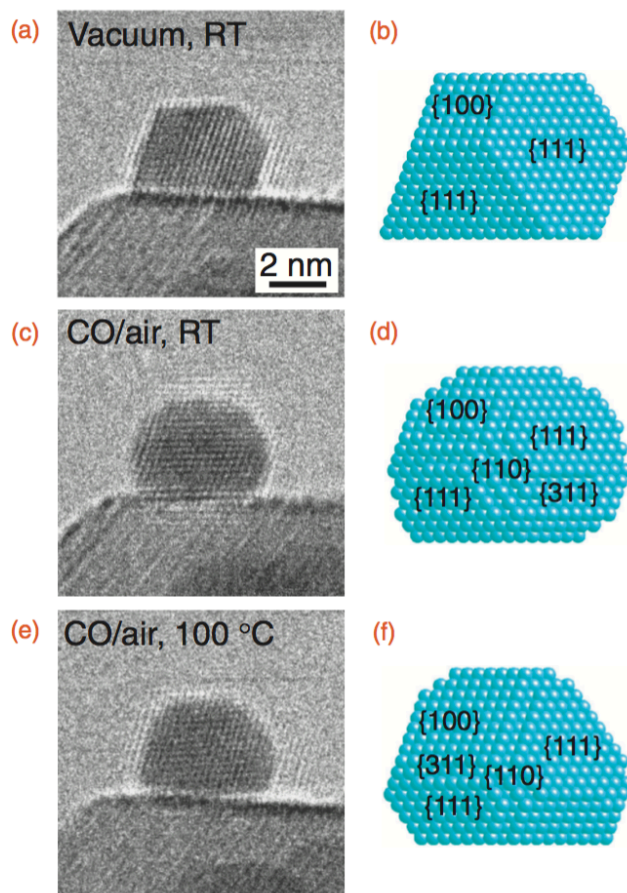
Figure 3.4: (a), (c), (e) In situ observations of a Pt nanoparticle supported on CeO_2 in different conditions and (b, d, f) the corresponding models of the Pt nanoparticle [50].
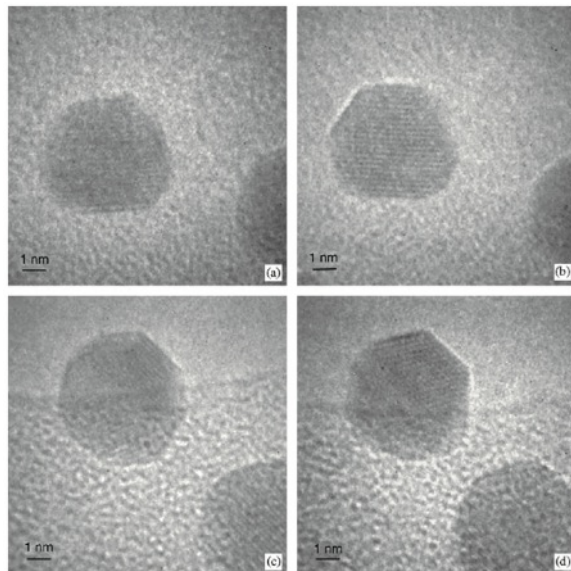
Figure 3.5: A Au nanoparicle on amorphous carbon observed in (a) vacuum, (b, d) H$_2$ at 2 mbar, and (c) O$_2$ at 2 mbar [30].
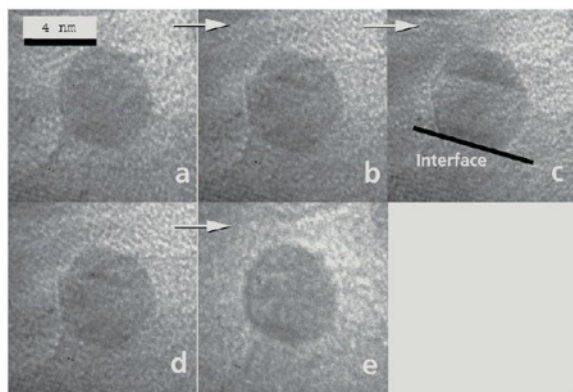
Figure 3.6: ETEM images of Au nanoparticle supported on TiO$_2$ (a) in vacuum, (b, c) in H$_2$ (b,c) and (d, e) in O$_2$ at 2 mbar at room temperature [51].
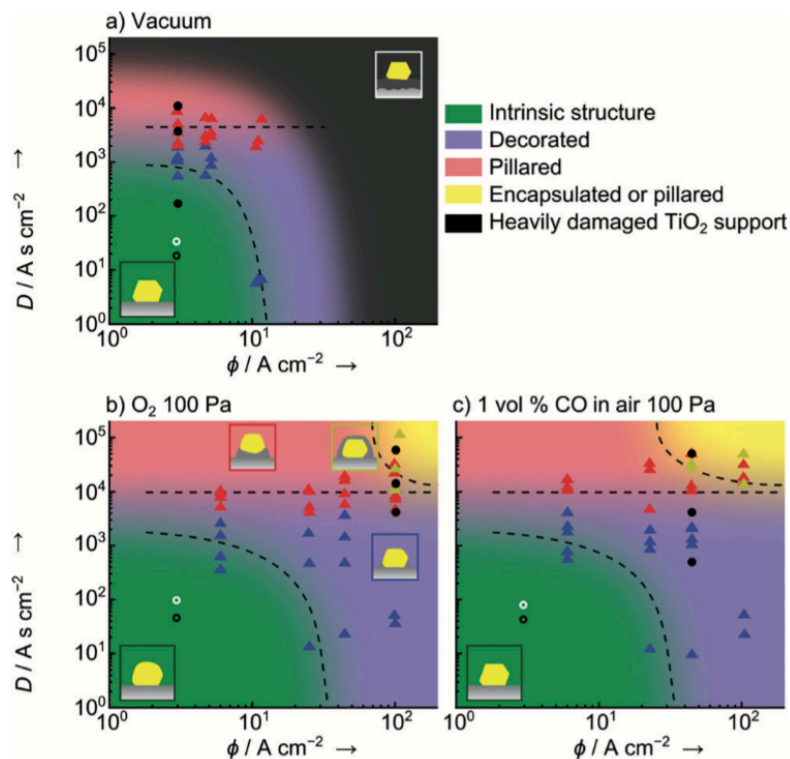
Figure 3.7: Electron irradiation effect on Au/TiO$_2$ catalysts in a) vacuum, b) O$_2$ (1 mbar), and c) 1 vol% CO in air (1 mbar) at room temperature. [52].

More recently, aberration-corrected ETEM has been developed [53].   Without aberration-correction, surface of nanoparticles is not clear with Fresnel fringe.   Aberration-correction resolves this problem and enables us to observe surface structure of materials clearly at atomic scale.   In situ observation results of metal nanoparticulate catalysts using aberration-corrected ETEM were reported.   Yoshida *et al*. visualized CO molecules adsorbed at the surface of AuNPs and corresponding surface reconstructions of Au {100} plane (Fig. 3.8) [54].   In addition, Kuwauchi *et al*. observed a stepwise lateral displacement of the AuNPs on ceria even at room temperature, which suggests these AuNPs are weakly bonded to an O terminated surface (Fig. 3.9) [55].   Yoshida *et al*. examined oxidation and reduction of the surfaces of Pt nanoparticles using aberration-corrected ETEM (Fig. 3.10) [56].   Pt nanoparticles surface is oxidized in O_2 at room temperature.   In both vacuum and CO/O_2 gas mixture, the surface Pt oxides were reduced to Pt. They also showed that H_2O vapor inhibited the surface oxidation.
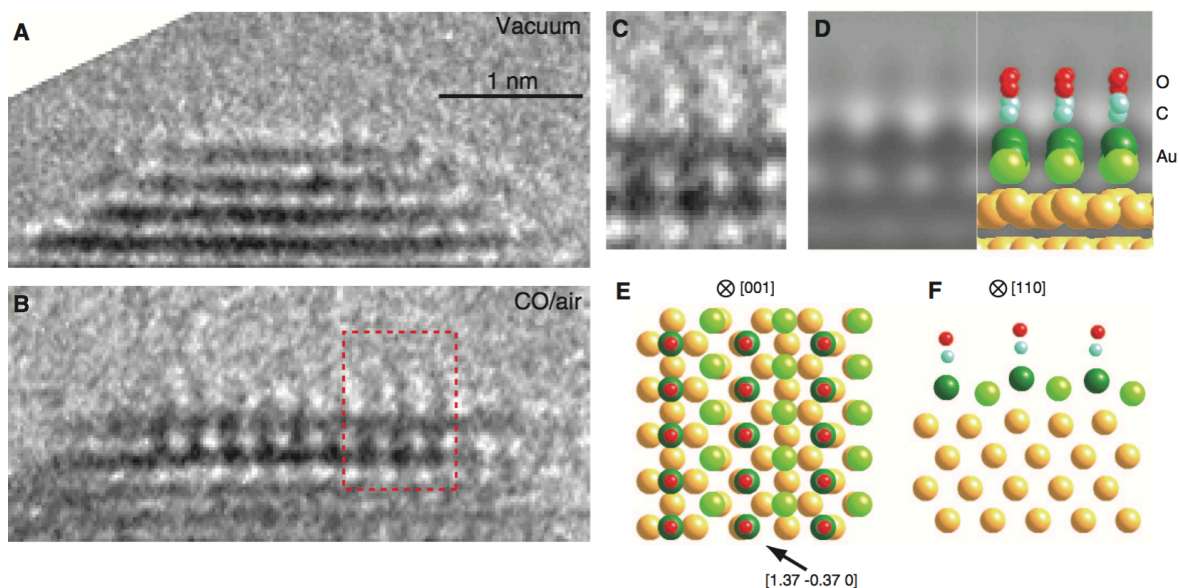
Figure 3.8: Aberration-corrected ETEM images of adsorbed CO molecules on a Au {100} in (A) a vacuum and (B) 1 volume % CO in air at 1 mbar at room temperature. (C) A magnification image in the rectangular region in (B). (D) A image simulation [54].
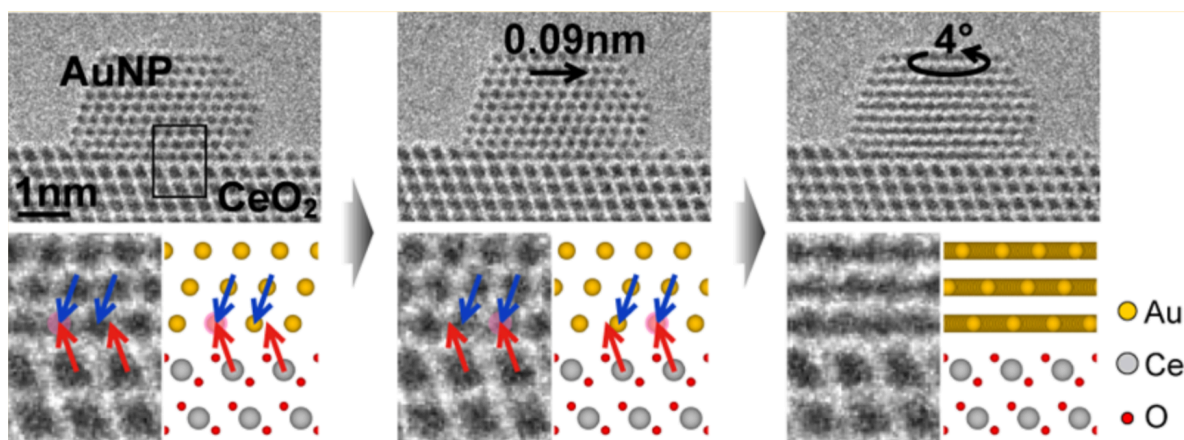
Figure 3.9: A stepwise lateral displacement of the AuNPs on ceria at room temperature [55].
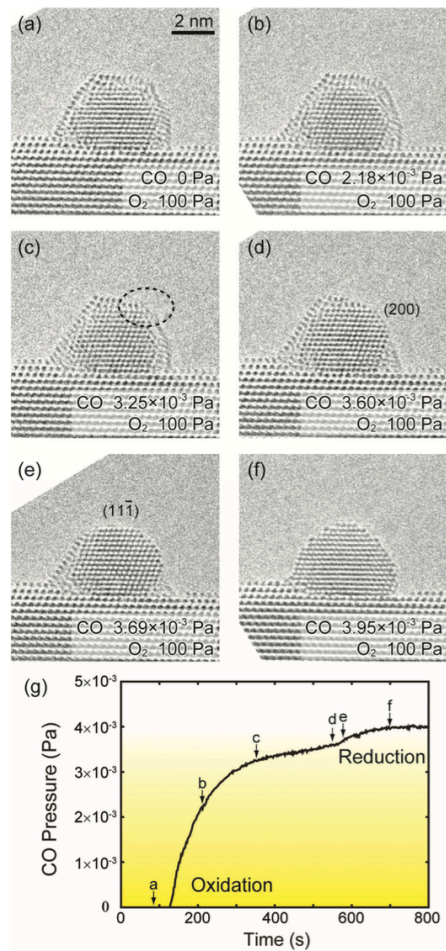
Figure 3.10: Aberration-corrected ETEM images of an oxidized Pt nanoparticle reduction in different partial pressure of CO. The partial pressure was (a) 0, (b) 2.18×10^{-5}, (c) 3.25×10^{-5}, (d) 3.60×10^{-5}, (e) 3.69×10^{-5} and (f) 3.95×10^{-5} mbar respectively [56].

Now we want to summarize the recent studies of catalysts using ETEM and show the point of issue. In the study of catalysts using ETEM, there are two problems as follows.

1. Relating ETEM images with catalytic reactions is challenging.

2. Behavior of Au catalysts is unclear in reaction conditions.

In most cases, catalytic reactions occur in the mixture of gases. Therefore, the ratio of the partial pressure of each gas is very important to relate the morphology of metal nanoparticles with catalytic reactions. However, systematic observations in different ratio of the partial pressure of each gas have never been carried out. Taking these problems into consideration, we observed Au catalysts in reaction conditions. Furthermore, we carried out systematic observations for the first time changing the ratio of the partial pressure of CO and O_2 (Chapter 6). We found that AuNPs change their shape depending on gas species and the ratio of the partial pressure of CO and O_2. We also considered reaction models in CO/air and O_2 from these results. Details are shown in Chapter 8.

Chapter 4

Effects of electron beam irradiation

4.1 Introduction

In TEM observation, it is impossible to get rid of the influence of electron beam completely. To examine the changes of AuNPs and supports derived from catalytic reactions, it is essential to determine the observation conditions that the influence of electron beam on AuNPs and CeO_2 supports is negligible. For this purpose, TEM and ETEM observations and electron energy loss spectroscopy (EELS) were held in vacuum, O_2 under low flux and high flux of electron beam.

4.2 Interaction of accelerated electrons with materials

In this section, before introducing experimental results, interactions of accelerated electrons with materials [57, 58] are shown briefly. When electrons enter a material, they interact with the constituent atoms via electrostatic (Coulomb) force. Interacting with these forces, some of the electrons are scattered. The scattering is divided into two categories, that is, elastic and inelastic scattering.

Elastic scattering involves Coulomb interaction with an atomic nucleus. Each nucleus has a high concentration of charge. Incident electron which approaches closely to the nucleus can be deflected with a large angle. The high-angle scattering is called as Rutherford scattering. If the scattering angle exceeds 90°, the scattering is called backscattered.

Inelastic scattering caused by Coulomb interaction between an incident electron and the electrons surrounding each nucleus. One of inelastic process is electron excitation. The electron in an orbital with lower energy is excited into other orbit with higher energy. Other inelastic processes are known as plasmon excitation which is collective oscillations of free electrons and phonon excitation which is vibration of atoms in crystals.

Inelastic collisions cause electron beam damages such as radiolysis, knock-on damage and heating. Radiolysis is the braking chemical bonds of certain materials, especially polymers, induced by electron-electron interactions such as ionization. Knock-on damage is the atomic displacement from the crystal lattice point, accompanying point defects. Heating means that phonons heat specimens.

For in situ observations, interactions of accelerated electrons on adsorbed molecules are important. There are two major processes in the desorptions of adsorbed molecules by electron irradiation. One is the desorptions by electronic excitation, which is well known as electron stimulated desorption (ESD), and the other is knock-on sputtering (Fig. 4.1). In section 4.4, we will explain the probability of these desorptions and discuss whether CO oxidation possibly

proceeds or not even under electron irradiation in observation conditions.
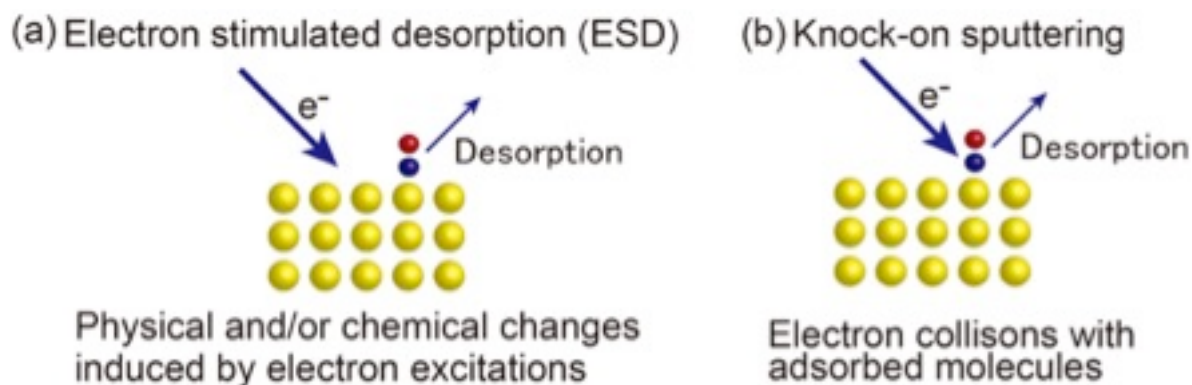
Figure 4.1: (a) Electron stimulated desorption (ESD) and (b) knock-on sputtering.

4.3 Experimental procedure

A Au/CeO$_2$ catalyst were prepared by a deposition precipitation (DP) method. It contains 5 wt% Au. The sample was dispersed on carbon microgrids. Then, it was set in an ETEM (FEI Tecnai F20 equipped with an E-cell) operated at 200 kV. We observed the sample in vacuum at room temperature. We carried out EELS measurements in vacuum, O$_2$ of 1 mbar. Successive ETEM images were recorded at a rate of 1 frame per 0.38 s or 0.43 s using a CCD camera of 2048 × 2048 pixels.

4.4 Results and discussion

As shown in Fig. 4.2(a), AuNPs are dispersed on CeO_2 support of several hundred nm in diameter. Fig. 4.2(b) shows a typical high resolution image of AuNPs on the CeO_2. The shape of Au nanoparticles is a nearly truncated octahedron enclosed by {100} and {111} facets. The <110> direction of Au and CeO_2 are nearly parallel.
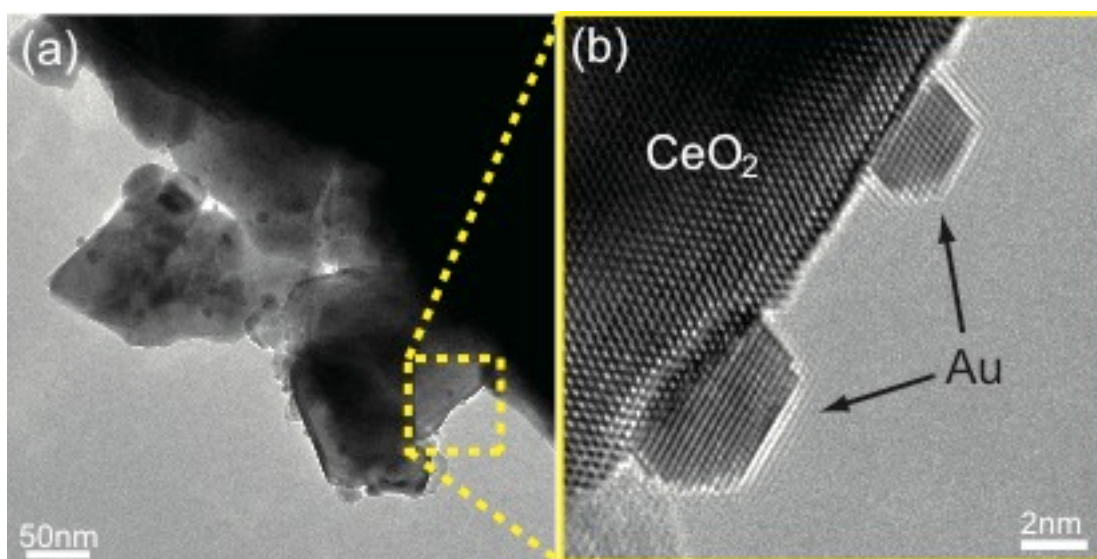
Figure 4.2: (a) Low magnification image and (b) high resolution image of Au/CeO_2 catalysts.

4.4.1 Effects of electron beam on AuNPs and CeO_2

At first, in order to examine the influence of electron irradiation to the sample, Au/CeO_2 catalysts were observed under electron

irradiation at 5 A/ cm^2 and 100 A/ cm^2.   Fig. 4.3 shows successive images of a AuNP on CeO$_2$ during electron beam irradiation at 100 A/ cm^2.   AuNPs changes its shape with time (Fig. 4.3(a)-(d)). Finally, it disappears (Fig. 4.3(e)).   It is confirmed that large electron flux affects the shape of AuNPs.   This phenomenon was reported by Akita *et al*. [59].   They explained that the shape change and diffusion of AuNPs depend on the density of oxygen vacancies in CeO$_2$ produced by electron beam irradiation.   They also suggested that this phenomenon is caused by the change of the interface energy of AuNPs and CeO$_2$.   Therefore, the phenomenon does not relate to catalytic reactions.   In investigating the effect of gases on the metal nanoparticles, it is necessary to observe under proper electron beam flux.
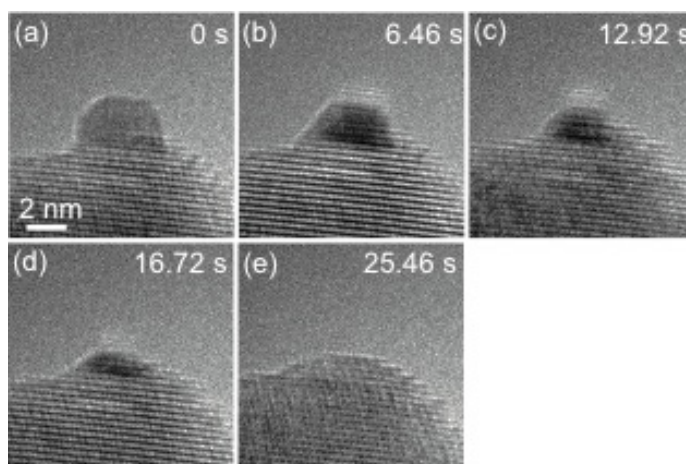
Figure 4.3: (a)-(e) Successive ETEM images of a AuNP on CeO$_2$ under 100 A/ cm^2 electron beam irradiation.   The recording time is shown in each image.

The effects of electron irradiation on CeO$_2$ supports were also examined.   Fig. 4.4(a) shows a TEM image of CeO$_2$ acquired

shortly after irradiation at 5A/ cm^2. Fourier transforms of the image correspond to the [011] zone-axis pattern from the fluorite structure of CeO$_2$. Fig. 4.4(b) shows a TEM image of CeO$_2$ acquired after 5 minutes irradiation at 5A/ cm^2. Comparing Fig. 5.4(a) with Fig. 4.4(b), there is little difference. After 5 minutes irradiation at 100 A/ cm^2, the extra spots are observed (Fig. 4.4(c)). Then waiting 90 minutes without irradiation, the extra spots disappear (Fig. 4.4 (d)). These phenomena were also reported by Akita *et al*. [59]. The extra spots arise from the ordered O vacancies made by electron beam irradiation. O vacancies are recovered reversibly with the influence of residual gases [59]. From these results, it can be said that there is little damage in CeO$_2$ during electron beam irradiation at 5 A/ cm^2.
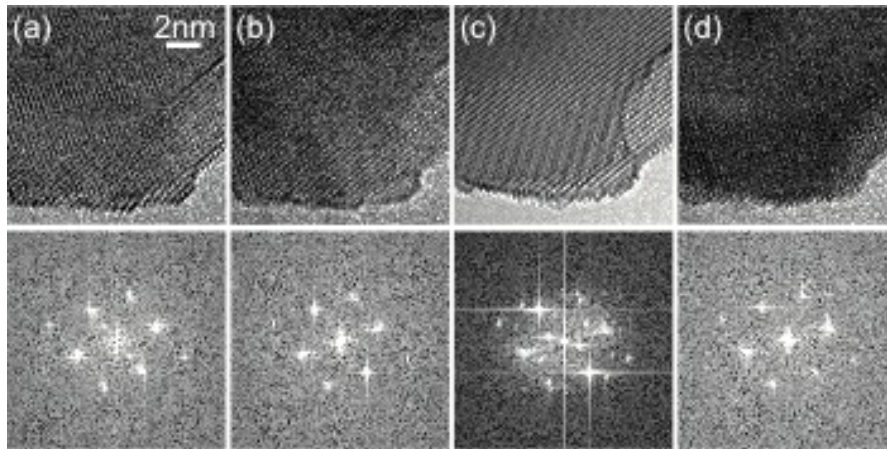
Figure 4.4: TEM images of CeO$_2$ acquired (a) shortly after irradiation at 5 A/ cm^2, (b) after 5 minutes irradiation at 5 A/ cm^2, (c) after 5 minutes irradiation at 100 A/ cm^2, (d) after 90 minutes without irradiation. Fourier transforms of the images are shown below.

4.4.2 EELS analysis of electron irradiation effects on CeO$_2$

To examine influences of electron beam, same site was irradiated for more than ten minutes. TEM images and EELS spectra at 0 minute and 10 minute irradiation were acquired. The peaks of Ce M edge appear at 885 eV and 900 eV. These peaks correspond to Ce^{3+} and Ce^{4+} individually. Ideally, start time of electron beam irradiation should be defined as 0 minute. However, from experimental difficulties, finish time of measurement of EELS spectrum was defined as 0 minute. TEM images and EELS spectra obtained after 0 and 12 minutes irradiation at 50 A/ cm^2 and 5 A/ cm^2 are shown in Fig. 4.5.   In the case of 5 A/ cm^2, there is little difference between a TEM image of 0 minute irradiation and that of 12 minutes irradiation (Fig. 4.5(a), (b)). Additionally, there is little difference between an EELS spectrum of 0 minute irradiation and that of 12 minutes irradiation (Fig. 4.5(e)). In the case of 50 A/cm^2, there is little difference between a TEM image of 0 minute irradiation and that of 12 minutes irradiation (Fig. 4.5(c), (d)). However, there are remarkable differences in EELS spectra (Fig. 4.5(f)). The ratio of the two peaks and the peak positions changed under electron irradiation of 50 A/ cm^2. These changes are caused by changes of electronic state from Ce^{4+} to Ce^{3+} [60, 61]. From these results, the amount of oxygen in CeO$_2$ does not decrease under 5 A/ cm^2 irradiation. On the other hand, it decreases under 50 A/ cm^2 irradiation.

Influences of electron beam were examined more precisely using EELS in vacuum, O_2 (Fig.4.6). Horizontal axis of the graph is irradiation time. Vertical axis of the graph is a ratio of the peak intensity of Ce^{4+} and Ce^{3+}. When the value of Ce^{4+}/Ce^{3+} is small, the amount of oxygen in CeO_2 is small. In vacuum, under 5 A/ cm^2 irradiation, the ratio of Ce^{4+}/Ce^{3+} is nearly constant. That is, the amount of oxygen in CeO_2 does not decrease in this condition. On the other hand, under 50 A/cm^2 and 100 A/cm^2 irradiation, the ratio of Ce^{4+}/Ce^{3+} become smaller as time goes by. This shows that the amount of oxygen in CeO_2 decreases in these conditions. Under 5 A/ cm^2 irradiation in O_2, oxygen in CeO_2 does not decrease. Under 5 A/ cm^2 irradiation, the ratio of Ce^{4+}/Ce^{3+} decrease not so much in O_2 as in vacuum. It seems that CeO_2 absorb oxygen molecules and compensate the irradiation damage. From these results, it seems that electron beam at 5 A/ cm^2 gives little damage to CeO_2 support in both vacuum and O_2. To confirm the electron flux does not influence on AuNPs, AuNPs on CeO_2 were observed for 20 minutes (Fig. 4.7). There is little change in AuNPs and CeO_2. Therefore, in examining Au/CeO_2 catalysts, suitable electron flux for ETEM observations is smaller than 5 A/ cm^2.
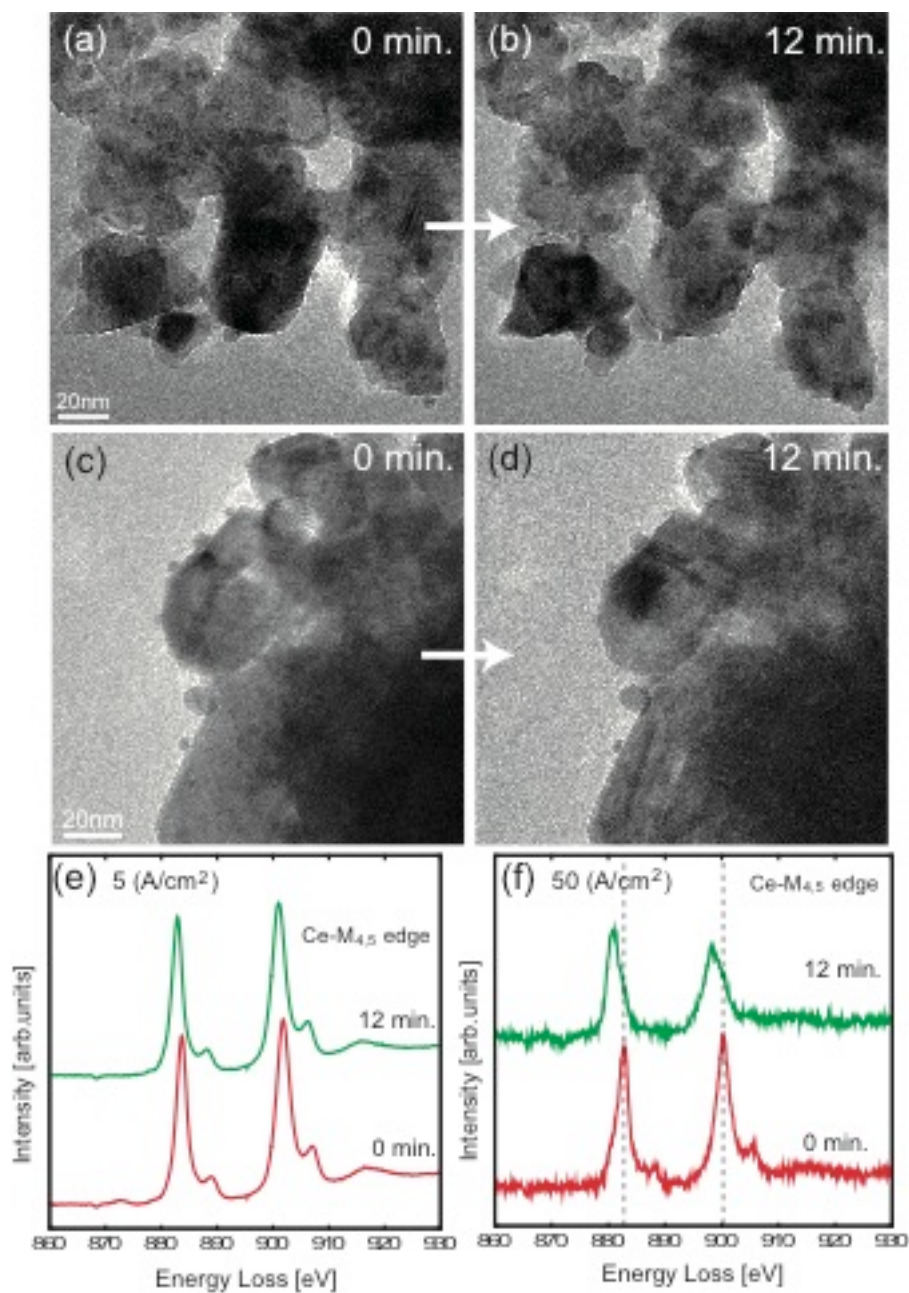
Figure 4.5: TEM images of Au/CeO$_2$ catalysts obtained at (a), (b) 5 A/ cm^2 and (c), (d) 50 A/ cm^2. EELS spectra of Ce-M edge of CeO$_2$ obtained at (e) 5 A/ cm^2 and (f) 50 A/ cm^2 .
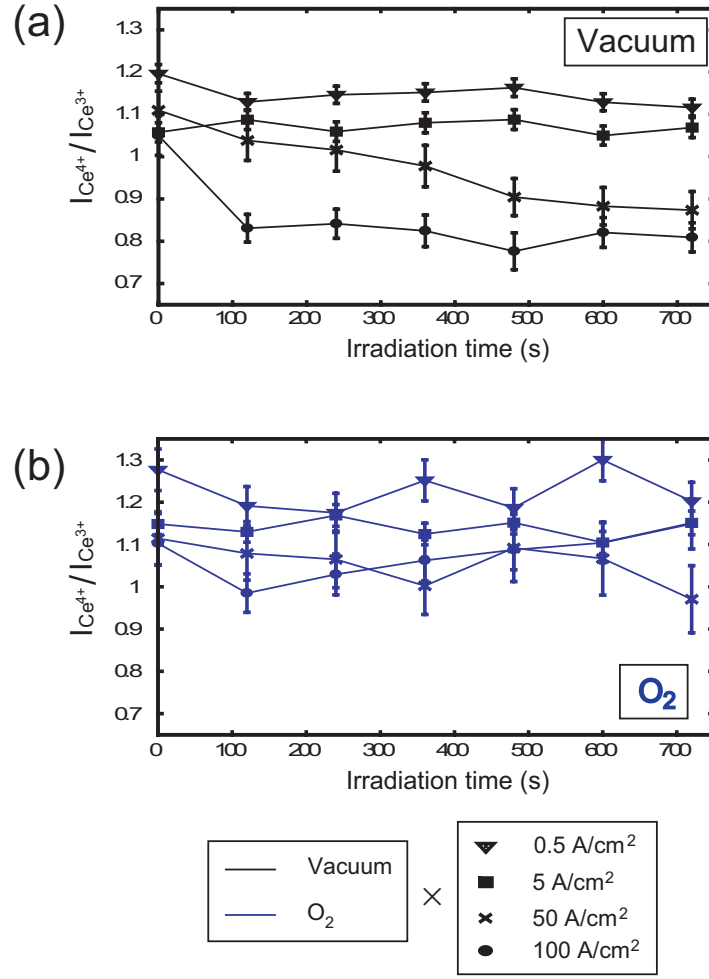
Figure 4.6: Results of EELS measurements of CeO_2 in vacuum and O_2 under electron flux of 0.5, 5, 50 and 100 A/ cm^2. Horizontal axis of the graph is irradiation time. Vertical axis of the graph is a ratio of the peak intensity of Ce^{4+} and Ce^{3+}.
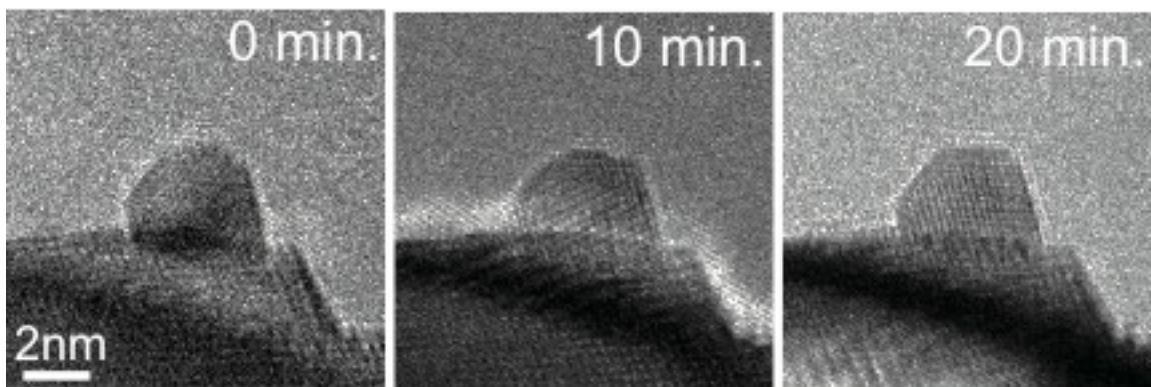
Figure 4.7: Successive TEM images of a AuNP on CeO_2 in vacuum under proper electron beam irradiation. The recording time is shown in each image. Electron flux is equal to 5 A/ cm^2.

4.4.3 Discussion about desorption of CO and O_2 molecules from the surface of AuNPs by electron irradiation

Now, we discuss about desorption of CO and O_2 molecules from the surface of AuNPs by electron irradiation. First, we consider about adsorptions of CO molecules to the surface of AuNPs. On the basis of classical kinetics, in 1vol.% CO/air of 1 mbar at room temperature, the collision rate of CO molecules with a Au atom is about 1773 s^{-1}. Since the initial adsorption probability of CO on Au clusters with average diameter of 3.4 nm is about 0.40 [62], the possible adsorption rate of CO molecules on a Au atom is estimated to be about 709 s^{-1}. This includes the desorption rate of CO molecules from the surface of AuNPs. This is sufficient to initiate reactions.

Second, we will consider about collisions of electrons to the adsorbed molecules. In the ETEM observations, adsorbed molecules are desorbed by 200 keV electrons. As we mentioned in section 4.2, two major processes in desorptions by electron irradiation are electron stimulated desorption (ESD) and knock-on sputtering (Fig. 4.1). We estimate the ESD cross-section (σ_{ESD}) and knock-on cross-section ($\sigma_{knock-on}$) for CO molecules adsorbed on Au. The ESD for CO molecules adsorbed on Au has not been investigated to our knowledge. Thus, we refer to σ_{ESD} for CO adsorbed on Pt by 0.26 keV electrons, which is estimated to be about 10^{-21} cm^2 [63]. In general, electronic excitations decrease with increasing incident electron energy. For example, the ionization cross-section for C atom decreases from 1.3 x 10^{-16} to 5.3 x 10^{-19} cm^2 with increasing incident electron energy from 0.26 to 200 keV [64]. Therefore, σ_{ESD} for CO adsorbed on Au by 200 keV electrons could be roughly estimated to be below 10^{-23} cm^2. Next, we try to estimate $\sigma_{knock-on}$ for CO molecules on Au. The adsorption energy of CO on Au at coverage 0 is about 0.77 eV [65]. On the assumption of the C atoms (not CO molecules) adsorb on Au with 0.77 eV, $\sigma_{knock-on}$ for C atoms from Au is estimated by Mckinley-Feshbach formula [66] to be 1.1 x 10^{-21} cm^2. $\sigma_{knock-on}$ for CO molecules from Au is roughly estimated to be 10^{-21} cm^2 [67]. When the electron flux is 5 A/ cm^2 (3.1 x 10^{19} electrons cm^{-2} · s^{-1}), the ESD and the knock-on rates of CO from Au are 3.1 x 10^{-4} s^{-1} and 3.1 x 10^{-2} s^{-1}, respectively. These values are much smaller than the possible adsorption rate of CO molecules on a Au atom (709 s^{-1}).

We also consider about O_2 adsorption. In 1vol.% CO/air of 1 mbar, partial pressure of O_2 molecules is 21 times larger than the one of CO. Though adsorption site of O_2 molecules seems to be perimeter interface and desorption probability of O_2 molecules is higher than that of CO molecules, the number of adsorbed O_2 molecules will increase. From these considerations, the adsorptions of CO and O_2 molecules to the surface of AuNPs possibly occur in 1vol.% CO/air of 1 mbar at 5 A/ cm^2 at 200kV.

4.5 Summary

ETEM observations and EELS measurements in vacuum, O_2 and CO/air have shown that electron beam gives little influence on AuNPs and CeO_2 support when the electron beam flux is smaller that 5 A/ cm^2. Additionally, desorptions of CO molecules from the surface of AuNPs by electron beam are estimated. From the estimations, CO molecules are most likely adsorbed at the surface of AuNPs under 5 A/ cm^2 electron flux. From these results, it is concluded that proper flux in ETEM observations is smaller than 5 A/ cm^2

Chapter 5

Sample contaminations from CO gases in ETEM

5.1 Introduction

ETEM is gaining popularity as a useful method for direct observation of various gas-solid reactions at the atomic scale. For ETEM to become a quantitative experimental technique used beyond imaging in the physical and chemical sciences, there are several issues to address. One important thing is considering effect of corrosive gases on ETEM observations. Vesborg *et al*. pointed out that a sample may be contaminated by Ni through the formation of Ni carbonyls in CO-containing gases and used a gas purifier for avoiding sample contamination [68]. Nevertheless, the process of contamination under electron irradiation has not yet been revealed. It is known that a CO gas of high pressure react with the inside wall of cylinders and gas supply lines, forming corrosion products (CPs). These CPs may be mixed within the gas being delivered to the ETEM and decomposed by electron irradiation in the ETEM, forming contamination on samples. In this chapter, after examining the contamination process by ETEM, we demonstrate that gas purification is crucially important to observe intrinsic phenomena in CO-rich gases by ETEM and thus to improve the accuracy of ETEM experiments.

5.2 Experimental procedure

The storage, supply and evacuation system of gases with safety protection was constructed for ETEMs, or FEI Tecnai F20 ETEM and Titan ETEM G2. Gatekeeper gas purifiers (made by Entegris) were installed after the mass flow controller of gases in the system. For CO gas, the gas cylinder and supply line were made of Mn steel (JIS G3429, STH12) and SUS316L respectively. Both materials contain Fe, and SUS316L also contains Ni. The nominal CO gas purity was better than 99.95 %. The pressures of CO gas in the gas cylinder and supply line were 9.81 MPa and 0.10 MPa, respectively. The pressure of CO gas was lowered and could be controlled at certain pressures by the mass flow controller in the CO supply line to ETEMs. For the present work, ETEM observations were performed without the gas purifier for CO gas, using FEI Tecnai F20 ETEM. We set the pressure of CO gas at 1 mbar for ETEM observations with and without the gas purifier for CO gas for the sake of comparison. Au/CeO_2 powder was used for observations. The samples were supported on a holey carbon film backed with a Cu or Mo grid. The grid was set on a specimen holder and inserted in an FEI Tecnai F20 ETEM (200 kV) for ETEM observations (electron beam current: 4.4 A/cm^2) at room temperature; measurements were made under CO gas and under vacuum conditions. Before and after ETEM observations, the samples on the grid were examined in vacuum with an FEI Titan ETEM G2 (300 kV) for electron energy loss spectroscopy (EELS) and energy dispersive X-ray spectroscopy (EDX) measurements, and with an FEI Titan 200 kV with ChemiSTEM EDX to attempt to detect small

amounts of impurities on the sample surfaces after ETEM observations. It should be noted that small amount of neither contaminations nor impurities were detected on a surface of the samples after ETEM observation in dilute CO gas mixtures, such as 1 mbar of 1 vol.% CO in air even without a gas purifier. The dilute gases were delivered to ETEMs through a gas supply line that was different from one for CO-rich gases. Residual gases in each ETEM were measured using a quadrupole mass spectrometer. The total pressure of residual gas in the Tecnai ETEM was 6.5×10^{-4} mbar, consisting of 5.9×10^{-4} mbar of H_2O, 0.3×10^{-4} mbar of N_2, 0.1×10^{-4} mbar of O_2, and 0.1×10^{-4} mbar of CO_2.

5.3 Results and discussion

Seven AuNPs on a Mo grid and 11 on a Cu grid were observed. ETEM images acquired without the gas purifier show contamination on all of the AuNP surfaces (Fig. 5.1). The pressure of CO gas was controlled at 1 mbar. After exposure to the CO gas, impurities appeared promptly within a few second on one facet of a AuNP (Fig. 5.1(a)), followed by the other facets (Fig. 5.1 (b) and (c)). The contamination sites then coalesced into one layer (Fig. 5.1(d)) that encapsulated the AuNP (Fig. 5.1(e)) and grew thicker (Fig. 5.1(f)). The contamination accumulated in the CO gas only under electron irradiation. Once formed, the contamination species were stable and remained after returning to vacuum.
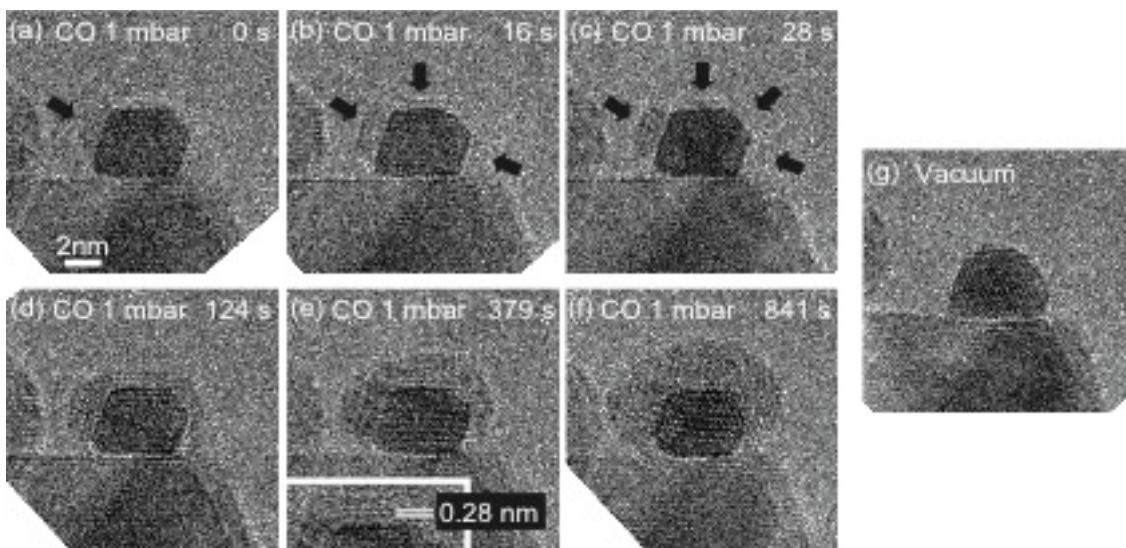
Figure 5.1: (a-f) In situ ETEM observations of a AuNP supported on CeO$_2$ in 100% CO gas. The gas purifier was not used. (a) -(c) A contamination layer appeared just after observation and (d)-(f) continued to accumulate over the observation time, as is evident from the progression of images. The inset in (e) is a magnified image of the CP on top of the AuNP. (g) TEM image of the AuNP in vacuum before the introduction of CO gas, as a reference. The sample was supported on a Mo grid.
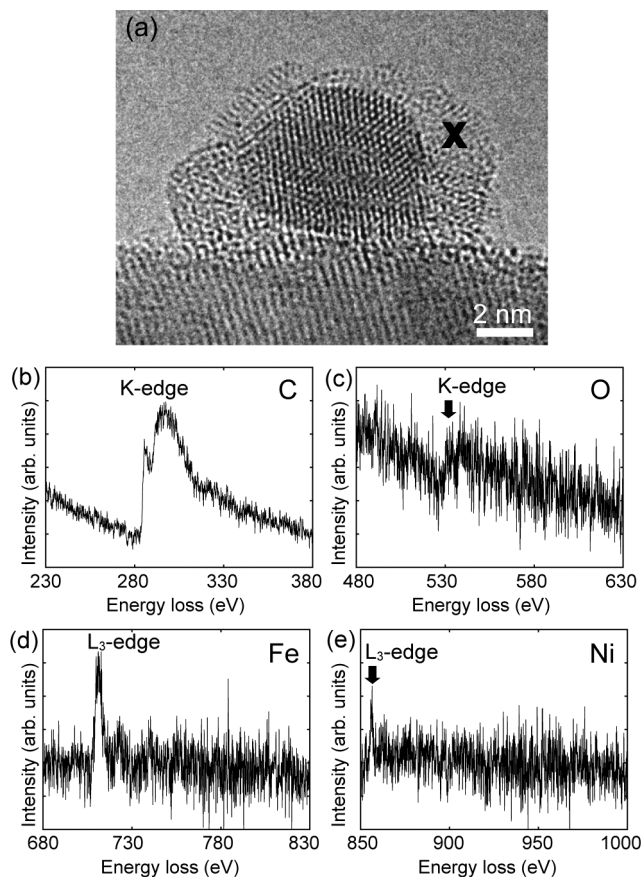
Figure 5.2: An EELS analysis of a contaminant in vacuum after ETEM observation in 100 % CO gas. The gas purifier was not used. (a) TEM image of a AuNP covered by a contamination layer. (b–e) EELS spectra of the contaminant obtained from the point indicated in the TEM image. The spectra were acquired in the energy regions corresponding to C, O, Fe, and Ni. The grid was Cu. C, Fe, and Ni peaks are confirmed.

Chemical analyses of these impurities using EELS in scanning transmission electron microscopy (STEM) mode were performed. The nine contamination sites that we examined all showed an Fe peak. Eight showed a C peak, four showed a Ni peak and three showed an O peak. Figure 5.2 gives the TEM image and EELS

spectra of an impurity showing the Fe L_3-edge, Ni L_3-edge, C K-edge, and O K-edge. EDX analysis also indicated Fe and Ni peaks (Fig. 5.3).
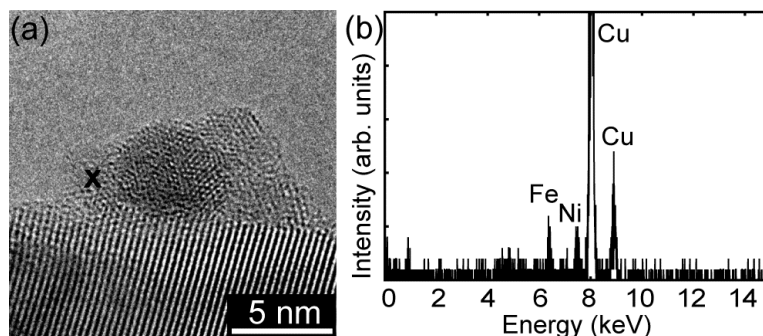
Figure 5.3: EDX analysis of a contaminant in vacuum after ETEM observation in 100 % CO gas. The gas purifier was not used. (a) TEM image of a AuNP covered by a contamination layer. (b) An EDX spectrum of the contaminant obtained from the point indicated in the TEM image. Fe and Ni peaks are confirmed. The Cu peak comes from a Cu grid.

The Fe and Ni contaminations likely come from the gas cylinder and supply line, which contain Fe and Ni. CO is known to corrode Fe and Ni to form iron carbonyls and nickel carbonyls [69,70], and electron-beam-induced deposition (EBID) of $Fe_2(CO)_9$ produces nanoparticles containing C, O, and Fe [71]. EBID of $Fe(CO)_5$ gas has also produced amorphous nanostructures containing Fe, C, and O [72]. In addition to the amorphous-like contamination containing metals (Fe and/or Ni) (Fig. 5.4(a)), some of the contaminants were crystalline. The measured lattice fringe spacings of the contaminants are 0.31, 0.28, 0.26, and 0.25 nm (Figs.

5.1(e), 5.4(b–d)). These are close to the interplanar distances of Fe_2O_3 (0.270 and 0.252 nm for the {104} and {110} planes, respectively), Fe_3O_4 (0.297, 0.253, and 0.242 nm for the {220}, {311}, and {222} planes, respectively), Fe_3C (0.301 and 0.254 nm for the {111} and {020} planes, respectively), Fe_2C (0.301 and 0.252 nm for the {111} and {020} planes, respectively), $FeCO_3$ (0.279 and 0.256 nm for the {104} and {006} planes, respectively), and $NiCO_3$ (0.271 nm for the {104} plane). Though we cannot identify the contaminants that were induced by the decomposition of CPs under electron irradiation, the CPs evidently contain Fe and Ni. The AuNPs were much more contaminated than the CeO_2 support. The metal-containing (Fe and/or Ni) contaminants are possibly unstable under subsequent electron irradiation on the support surface.
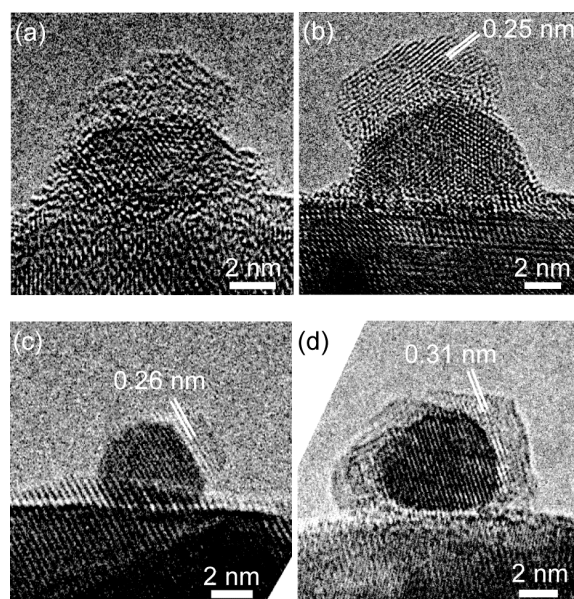
Figure 5.4: Morphology of contaminants on different AuNPs. The gas purifier was not used. The contaminant took on an amorphous structure in (a), while those in (b-d) displayed lattice fringes. The grid for all of these was Cu.

For the sake of comparison, we show ETEM observation of the same sample with a gas purifier. First we selected AuNPs that did not undergo the preceding electron irradiation. We set the pressure of 100% CO gas at 1 mbar. After continuous observation for 10 min, we did not observe the formation of any contaminants on the AuNPs (Fig. 5.5(a)). The AuNPs were well facetted in the 100% CO gas, which was already considered in previous work. EDX analyses of eight AuNPs in STEM mode after evacuating the CO gas (Fig. 5.5(b) and (c)) were performed. No C, Fe, or Ni peaks were found. Therefore, CPs can be removed effectively by a gas purifier. CPs were likely produced mainly in the gas cylinder because the pressure in the cylinder (9.81 MPa) was higher than that in the supply line (0.10 MPa). It is also concluded that the formation of CP is entirely suppressed in CO gas of low pressure (1 mbar) within the accuracy of analyses. Therefore, the contamination on metal surfaces in CO-rich environment originates from the defective gas supply. It was speculated [73] that CO gas is directly decomposed by intense irradiation of high energy electrons at room temperature, giving rise to carbon contamination on the surface of a catalytic material. We did not detect carbon contamination on the surface of AuNPs even after prolonged ETEM observation with an ordinary current intensity of 200 keV electrons (about 5 A/ cm^2) (Fig. 5.5(a)). We think that the crystalline contamination shown in the previous reports (Fig. 6d and Supplementary Movie S6 in ref. [73] and Fig. S3 in ref. [74]) may be identified as iron compounds such as Fe_3O_4, Fe_2O_3 and $FeCO_3$, or CPs rather than crystalline carbon structures. Clearly, the upper-left of Supplementary Movie S6 (18 sec) in ref. [10] is identified to be Fe_3O_4 (Magnetite structure,

F d -3 m, a = 0.8396 nm) observed along the [110] direction. It is most likely that the observed phenomena [73, 74] do not correlate directly with the intrinsic chemical reaction of the catalytic material.
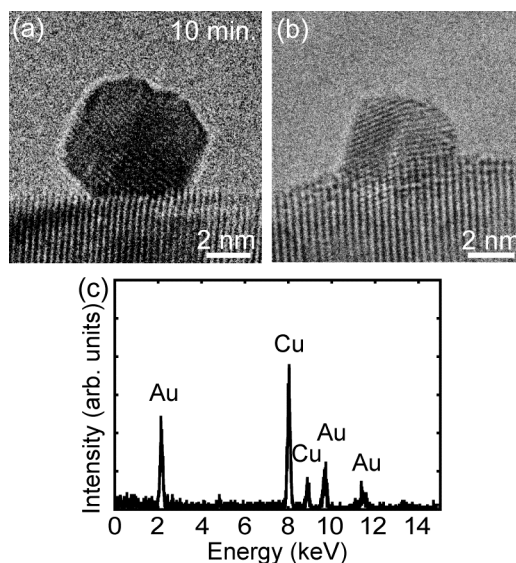
Figure 5.5: (a) In situ ETEM observation of a AuNP in 100 % CO gas using a gas purifier after electron irradiation for 10 min. (b) TEM image of a AuNP observed in 100 % CO gas for 10 min after CO gas evacuation. (c) An EDX spectrum obtained from the AuNP in (b) in vacuum after the ETEM observation. The grid was Cu. No C, Fe, or Ni peaks were seen.

5.4 Summary

In summary, we examined the problem of unintentional sample contamination in ETEM observation when using corrosive gas mixtures, such as those rich in CO. Once gaseous corrosion products are delivered to the ETEM, they are decomposed under electron irradiation, forming metal-containing contaminants (Fe and/or Ni) on the sample surfaces. We revealed the contamination process using ETEM. Installing a gas purifier in the CO supply line was able to effectively prevent CPs from being delivered to the ETEM.

Chapter 6

Systematic observation of Au/CeO$_2$ catalysts in reaction condition

6.1 Introduction

Despite numerous studies, reaction mechanism of CO oxidation by Au catalysts is still unclear. Furthermore, even AuNPs and support structure in catalytic reactions has not been determined yet. To examine behaviors of AuNPs in catalytic reactions, high resolution in situ observation of Au catalysts is indispensable. In this chapter, we observed an active Au/CeO$_2$ catalyst in CO/air mixture by means of ETEM. For comparison, a Au/TiC catalyst which is known to show low catalytic activity in CO oxidation was also observed in CO/air and O$_2$.

6.2 Experimental procedure

A Au/CeO$_2$ catalyst was synthesized as follows [75]. Gold deposited CeO$_2$ was prepared by the DP method [11] (see Appendix A), followed by calcination in air at 300 °C for 4 hours. The Au composition was 5 wt.%. The size distribution of AuNPs was measured by STEM. A mean diameter of AuNPs was estimated to

be 4.1 nm with a standard deviation of 1.3 nm.   Typical orientation relationships between AuNPs and crystalline CeO_2 supports were (111)[1-10]Au//(111)[1-10]CeO_2,   (111)[1-10]Au//(111)[-110]CeO_2 [76].   The activity of Au/CeO_2 catalysts was measured using a fix bed flow reactor by passing 1 vol.% CO in air at a space velocity of 20,000 h^{-1}ml/g_{cat}.   The conversion of CO to CO_2 reached 100% at room temperature.   The rates for CO oxidation per unit catalyst weight and per supported gold (MTY) were measured to be 7.4×10^{-6} mol_{CO} g $^{-1}$ · s^{-1} and 0.081 mol_{CO} $(mol_{Au})^{-1}$ s^{-1}, respectively. The corresponding turnover frequency (TOF), which is normalized to the number of exposed metal (gold) surface atoms, was measured to be 0.24 (mol_{CO} · $(mol_{Ausur.})^{-1}s^{-1}$).   Au/TiC catalyst was prepared as follows.   First, TiC powders were dispersed on carbon microgrids.   Then Au was deposited via vacuum deposition method. The average thickness of Au was 1 nm.   The samples were set in an ETEM (FEI Tecnai F20 equipped with an E-cell) operated at 200 kV (Fig. 6.1).   Gases of pure O_2, pure N_2, 1vol.% CO/air (1vol.% CO, 21vol.% O_2, 78vol.% N_2), 0.01vol.% CO/air (0.01vol.% CO, 20.9vol.% O_2, 79.09vol.% N_2) and air (20vol.% O_2, 80vol.% N_2) were introduced into ETEM.   We observed samples in the gases in sequence at room temperature.   It took about 1200 s to 1800 s to switch the gases in ETEM.   The morphology of AuNPs in the gas did not depend on a sequence of gases.   The reduction of the CeO_2 support by electron irradiation is recovered by residual oxygen.   It has already been confirmed that ETEM images of solids in gases of low pressures are similar to those in vacuum [77].   Using a CCD camera, ETEM images of 512 × 512 pixels were recorded with a

56

rate of 1 frame per 0.65 or 0.73 s. It was reported that CeO_2 supports is much more stable toward electron irradiation than TiO_2 [78]. As shown in chapter 4, to reduce electron irradiation damage, electron flux was set to be smaller than 5.3 A/ cm^2.
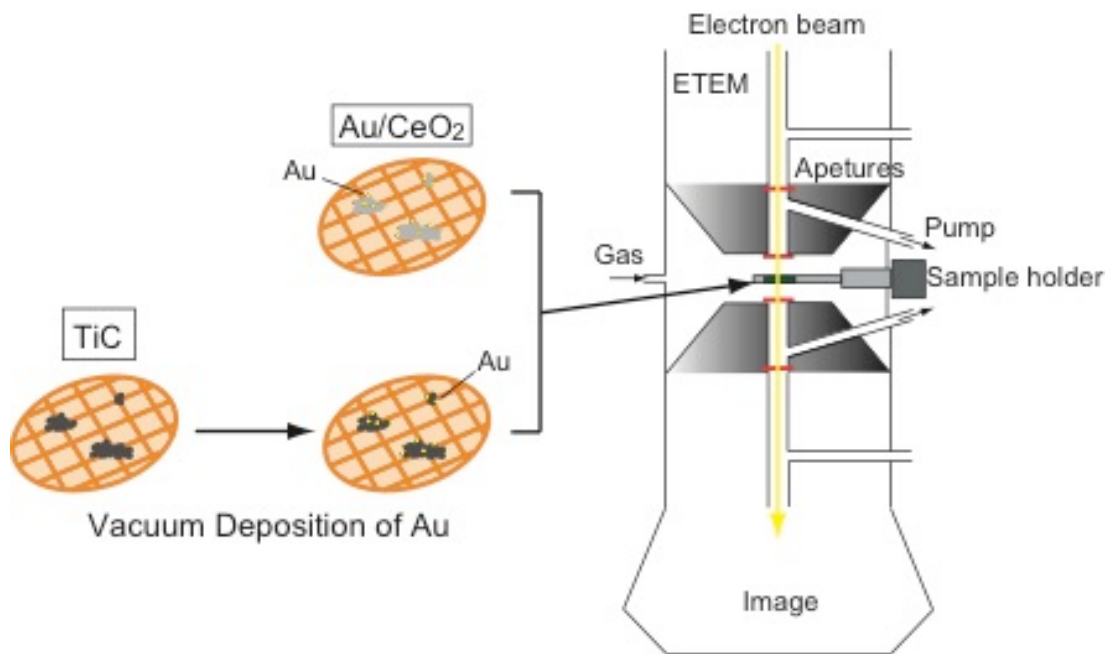
Figure 6.1: Sample preparation for in situ observation of Au catalysts.

6.3 Observation of Au/CeO$_2$ catalysts in various atmosphere

6.3.1 Observation of Au/CeO$_2$ catalysts in air and 1vol.%CO/air

ETEM observations of AuNPs on CeO$_2$ in CO/air and air were carried out. Cross-sectional images and plan-view images of a AuNP on CeO$_2$ obtained in vacuum, air of 3.4 mbar and 1vol.% CO/air of 3.4 mbar are shown in Fig. 6.2. AuNPs clearly show facets such as {111} and {100}. After introducing air, AuNPs turn to be round. Then, we introduced 1vol.% CO/air in ETEM. AuNPs retrieved faceted shape.
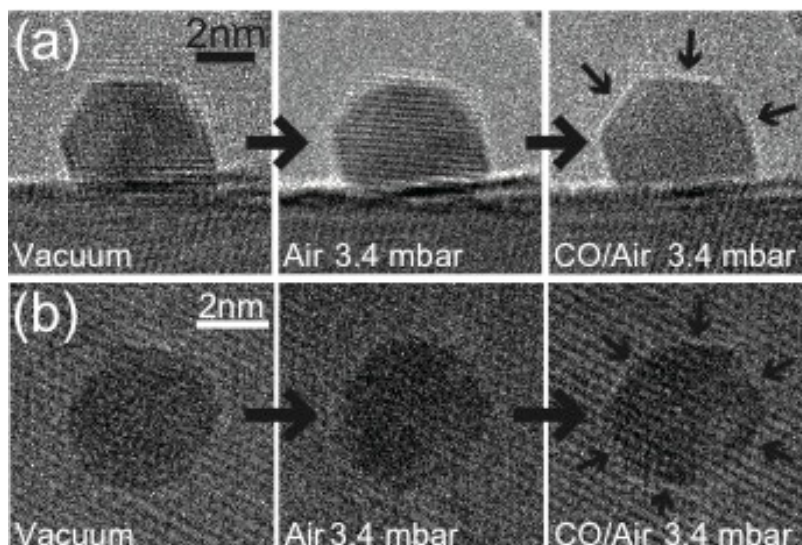
Figure 6.2: (a) cross-sectional images and (b) plan-view images of a AuNP on CeO$_2$ obtained in vacuum, air of 3.4 mbar and 1vol.%

CO/air of 3.4 mbar. The AuNPs show facet shape in vacuum and 1vol.% CO/air. While they are round in air.

6.3.2 Observation of Au/CeO$_2$ catalysts in various ratio of O$_2$ and CO

In order to find out the origin of the morphology change, we changed CO partial pressure of CO/air mixture. The total pressure of the gas was kept at 3 mbar. First, we confirmed that AuNPs showed facet shape in both vacuum and 1vol.% CO/air of 3 mbar (CO: 0.03 mbar, air: 2.97 mbar)(Fig.6.3). Then, we decreased the partial pressure of CO from 0.03 mbar to 0 mbar through 0.01, 0.001, 0.0002 mbar. As shown in Fig.6.3, the facets of the AuNP gradually disappeared. Finally, the AuNP became round. Similar observations using the mixed gas of 0.01vol.% CO/air and air were also carried out. The total pressure of the mixed gas was kept at 3 mbar. AuNPs showed faceted shape in both vacuum and 0.01 vol.% CO/air 3 mbar (CO 0.0003 mbar, Air: 2.9997 mbar) (Fig.6.4). Then, we decrease the partial pressure of CO from 0.0003 mbar to 0 mbar through 0.0001, 0.00001, 0.000002 mbar. AuNPs turned to be round with the decrease of CO partial pressure. It is most likely that the adsorption of CO on the surface of AuNPs stabilize the facets.
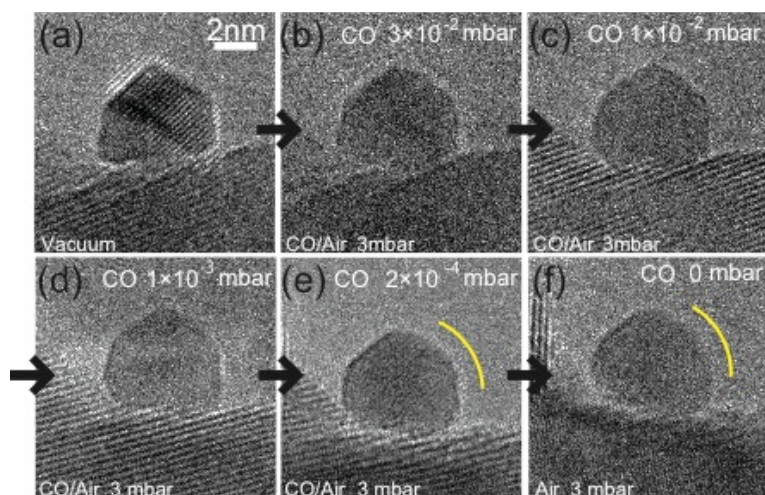
Figure 6.3: ETEM images of a AuNP obtained in the mixture of 1vol.% CO/air and air. The morphology of the AuNP changes with the decrease of the CO partial pressure. The AuNP becomes round with the decrease of the CO partial pressure. The total pressure of gases was kept at 3 mbar.
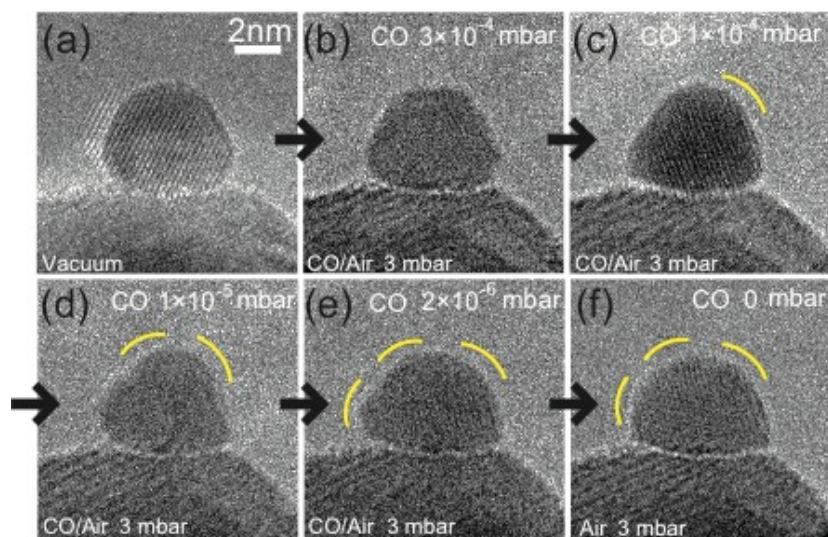
Figure 6.4: ETEM images of a AuNP obtained in the mixture of CO 0.01vol%/air and air. The morphology of the AuNP changes with the decrease of a partial pressure of CO. The Au nanoparticle

becomes round with the decrease of a partial pressure of CO. The total pressure of gases was kept at 3 mbar.

6.3.3 Observation of Au/CeO$_2$ catalysts in N$_2$, O$_2$ and 1vol.%CO/air

To examine the origin of the round shape of AuNPs in air, AuNPs were observed in pure N$_2$, pure O$_2$ and 1vol.% CO/air. As shown Fig. 6.5, a AuNP showed facets such as {111} and {100} in both vacuum and N$_2$ of 1mbar. After evacuation of the N$_2$ gas, a O$_2$ gas of 1 mbar was introduced into ETEM, the AuNPs became round. Then, the O$_2$ was evacuated and a 1vol.% CO/air gas of 1 mbar was introduced. AuNPs showed facets such as {111} and {100} again in 1vol.% CO/air. From these observations, it can be said that O$_2$ molecules make AuNPs round and CO gas molecules stabilize the facetted AuNPs.

To examine the influence of the collisions of gas molecules, detail observation of AuNPs in N$_2$ at 1 mbar and 3 mbar were carried out (Fig. 6.6). It is well known that N$_2$ gas is inactive at room temperature. Before introducing N$_2$ gases, it was confirmed that the shape of a AuNP does not change under proper electron beam irradiation for a long time (Fig. 6.6(a)). Under same electron beam irradiation, the AuNP is also stable in N$_2$ (Fig. 6.6 (b), (c)), though a surface Au atom collides with N$_2$ at the rate of about 6 x 10^5 /s in N$_2$ of 3 mbar. This is consistent with the fact that N$_2$ molecules are not adsorbed and dissociated at the surface of Au.

From these results, it can be concluded that the effect of inert gases on AuNPs can be negligible.
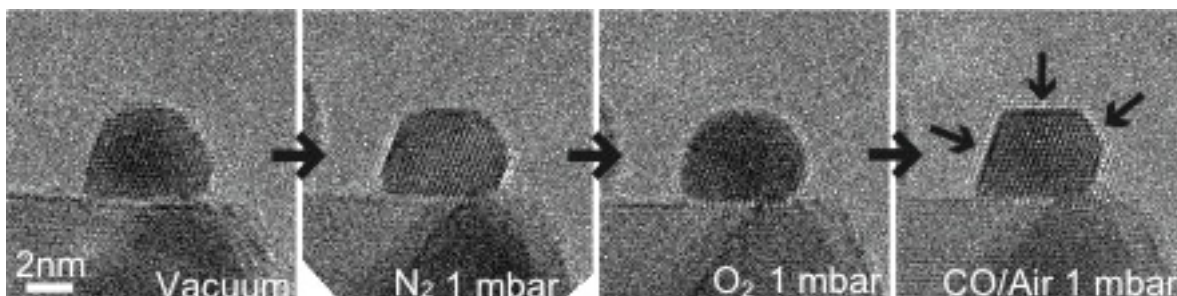
Figure 6.5: Cross-sectional images of Au/CeO$_2$ catalysts obtained in vacuum, N$_2$ of 1 mbar, O$_2$ of 1 mbar and 1vol.% CO/air of 1 mbar.
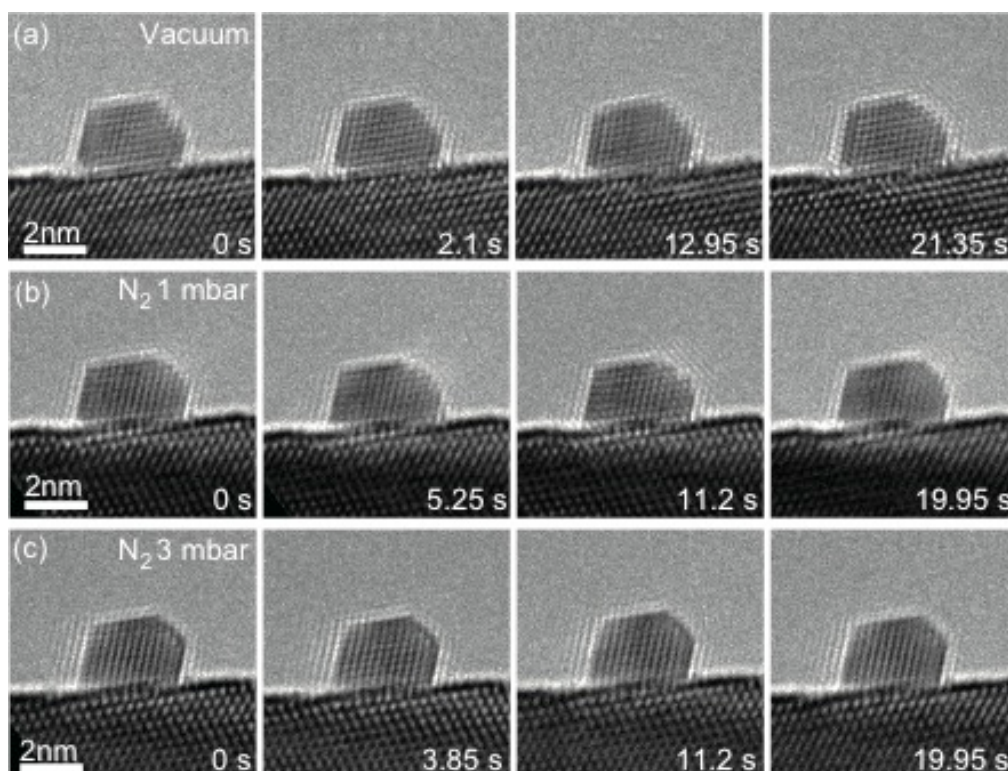
Figure 6.6: ETEM images of a Au nanoparticle on CeO$_2$ in (a) vacuum, (b) N$_2$ at the pressure of 1 mbar and (c) N$_2$ at the pressure of 3 mbar.

Temporal changes on the surface of AuNPs in O_2 (1 mbar), 1% CO/air (1 mbar) and N_2 (1 mbar) are shown in Fig. 6.7. As mentioned above, AuNPs are preferentially round in an O_2 gas, as seen in Fig. 6.7(a). Remarkable finding is that the surface of AuNPs exhibits different facets frame to frame. Especially, the minority {110} surface, which are rarely seen in either vacuum, a N_2 gas or a CO/air gas, appears frequently along with the major {111} and {100} surfaces, as indicated in yellow letters. This switching behavior of facets including the higher order facet such as {110} is the origin of the round morphology of AuNPs in an O_2 gas. On the other hand, the surface of the same AuNP was much more stable in 1vol.% CO/air (1 mbar) and N_2 (1 mbar). It is noteworthy that steps and kinks appear on the surfaces occasionally even in vacuum, as indicated by arrowheads. They are attributed to electron irradiation damage. To examine the shape change of AuNPs depending on partial pressure of CO and O_2 systematically, ETEM observations in various CO and O_2 partial pressure were carried out. Some of the observations are shown in Fig.6.8. The surface of AuNPs became partially rough in O_2 of 0.01 mbar and became round in O_2 of 1 mbar (Fig.6.8(a)). The morphology of AuNPs depends on the ratio of CO partial pressure and O_2 partial pressure (Fig.6.8 (b), (c)). Systematic morphology changes of AuNPs are summarized as morphology diagram in subsection 6. 3. 4.
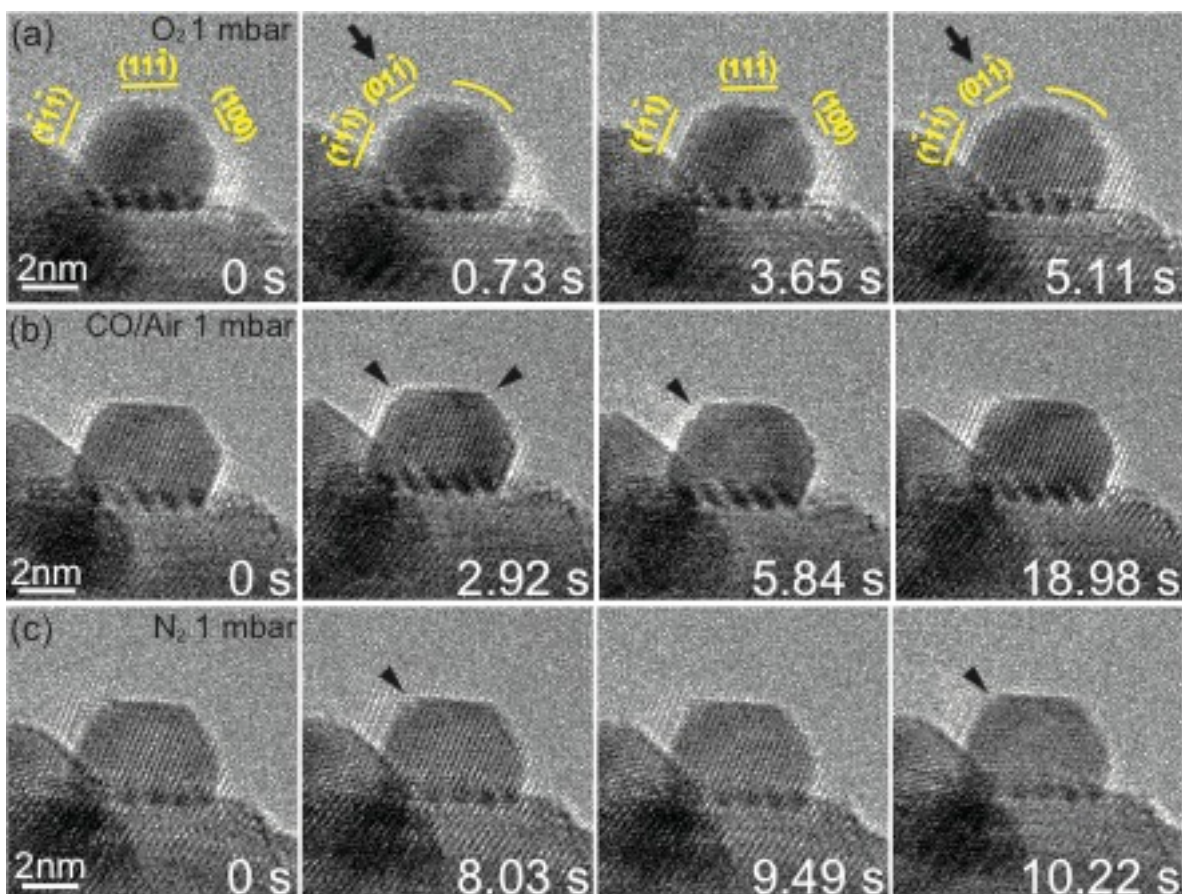
Figure 6.7: In situ observations of a AuNP (a) during CO oxidation in 1vol.% CO/air (1 mbar), (b) in O_2 (1 mbar) and (c) N_2 (1 mbar) gases. In O_2 gas, a AuNP exhibits {111}, {100} and {110} facets dynamically, while in CO/air, the major {111} and {100} facets are stable.
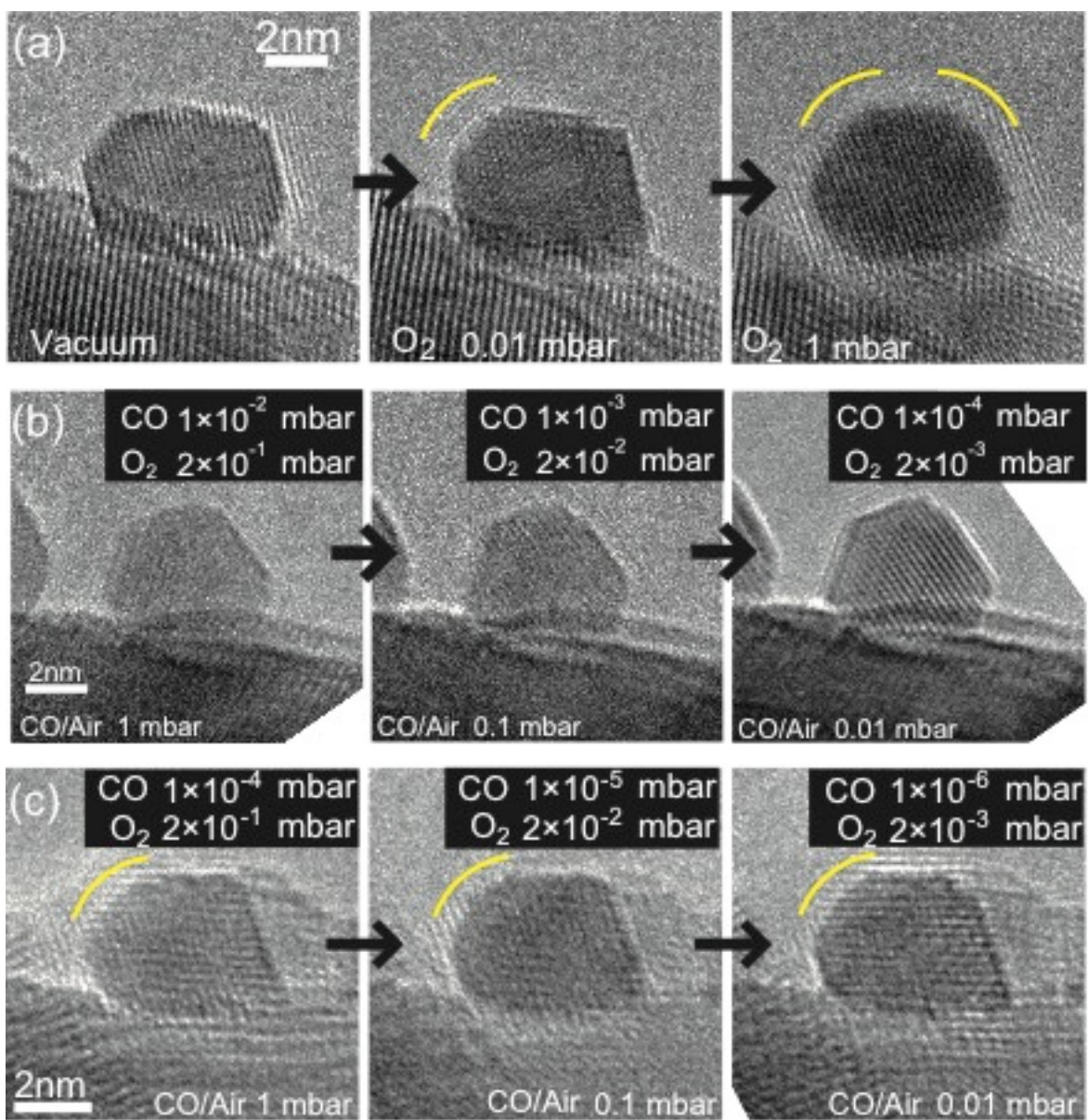
Figure 6.8: (a) Morphology of a AuNP in low pressure of pure O_2. (b), (c) Morphology of a AuNP in various ratio of CO and O_2. The partial pressure of CO and O_2 is shown in the images.

6.3.4 Morphology diagram of AuNPs supported on CeO$_2$ depending on partial pressures of CO and O$_2$

As shown in subsection 6.3.1, 6.3.2 and 6.3.3, the morphology changes are mainly depending on the partial pressure of CO and O$_2$. We purse the morphology of AuNPs on CeO$_2$ by systematically changing the partial pressure of CO and O$_2$ gases. Morphology of a AuNP in a gas is characterized numerically by relative morphology index, M. Details about relative morphology index, M are shown in ref. 50. When M exceeds 0.95, the morphology is classified as facet. When M is below 0.95, the morphology is round (dynamic multi-faceted). In this way, we determined the morphologies of five to fifteen AuNPs in a gas. When more than 70 percent of the AuNPs in a gas are classified by the same morphology. When the morphology of AuNPs in a gas disperse, or the percentage of the AuNPs belonging to the major morphology is smaller than 70 %, it is concluded that the morphology in the gas is represented by statistically mixed. The results are summarized in Fig. 6.9. AuNPs show facets such as {111} and {100} in CO/air with higher CO concentration. AuNPs change their morphology from faceted to round with the decrease of CO partial pressure. AuNPs become round when CO partial pressure is lower than 10^{-5} mbar and O$_2$ partial pressure is higher than 10^{-3} mbar.
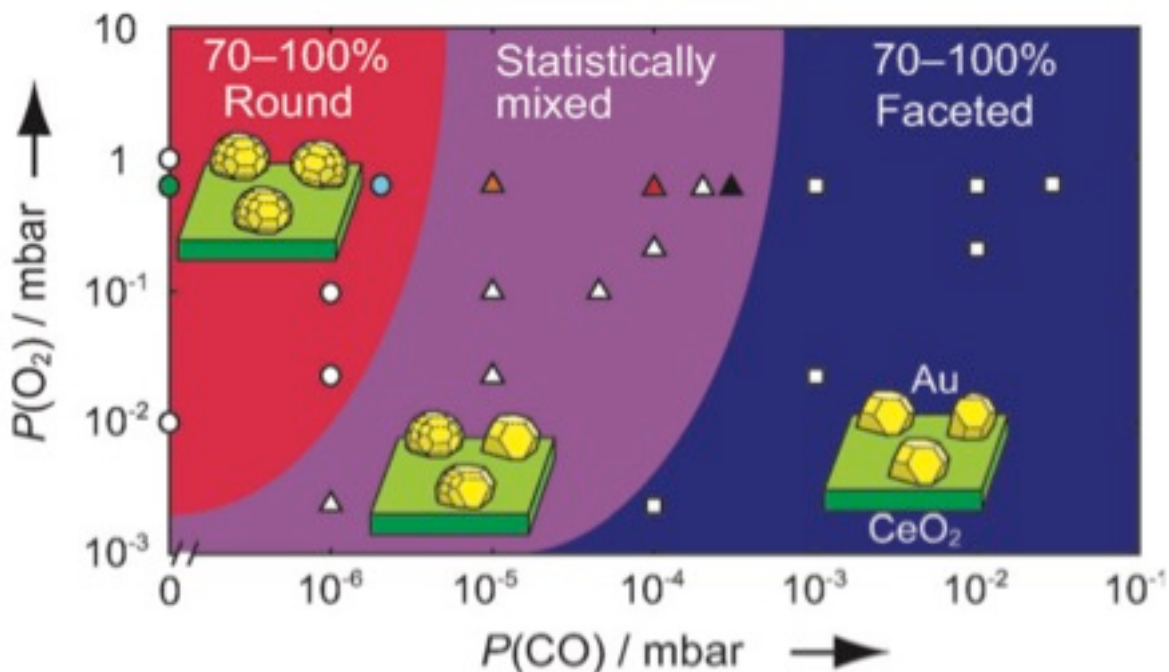
Figure 6.9: Morphology diagram of AuNPs supported on CeO_2 depending on partial pressures of CO and O_2 in mixed gases of CO/air. Squares, triangles and circles represent facet, statistically mixed, and round (dynamic multi-facet) morphology, respectively.

6.4 Observation of Au/TiC catalyst

In order to examine whether morphology of AuNPs in O_2 and CO/air differ depending on support materials, the Au/TiC catalyst were observed in vacuum, N_2, O_2 and 1vol.% CO/air. It is well known that Au/TiC catalysts show much less catalytic activity in CO oxidation [79]. As shown in Fig. 6.10(a), AuNPs are dispersed on TiC supports of several hundred nm in diameter. Fig. 6.10 (b) shows a typical high resolution image of AuNPs on the TiC. The shape of AuNPs is a nearly truncated octahedron enclosed by {100}

67

and {111} facets. As shown in Fig. 6.11, AuNPs showed facets such as {111} and {100} in both vacuum and N_2 of 1mbar. After evacuation of the N_2 gases, we introduced O_2 gases of 1 mbar into ETEM. AuNPs shows a faceted shape even in O_2 gases. They also show a faceted shape in 1vol.% CO/air. 1 out of 10 AuNPs became round in O_2 and became facet in 1vol.% CO/air. 8 out of 10 AuNPs became faceted in both O_2 and 1vol.% CO/air.
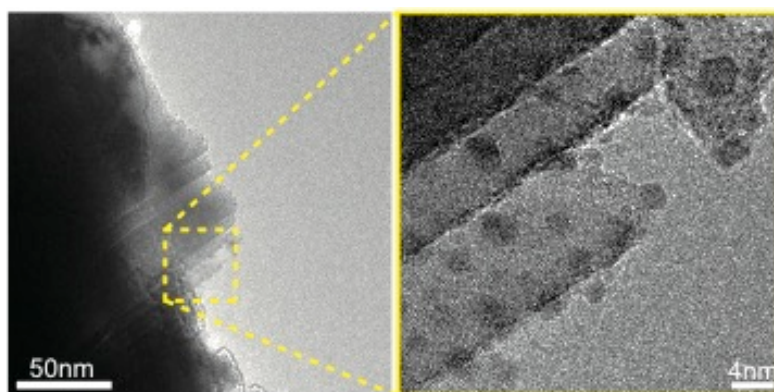
Figure 6.10: (a) Low and (b) high magnification images of Au/TiC catalysts.
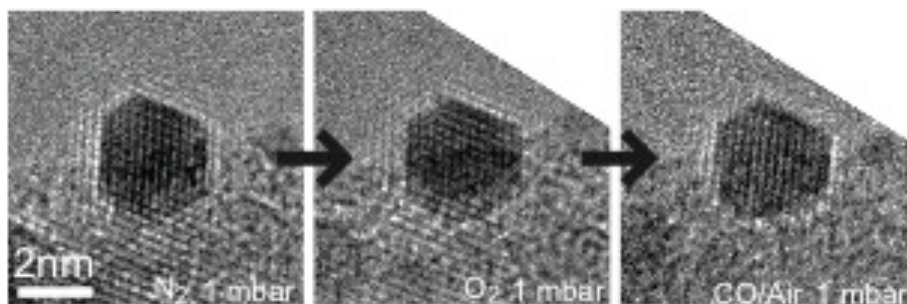
Figure 6.11: ETEM images of a Au nanoparticle on TiC in N_2, O_2 and 1vol.% CO/air.

6.5 Discussion about morphology of AuNPs in O_2 and CO/air

Now, we discuss the origin of the round morphology of AuNPs on CeO_2 in O_2. Mavrikakis *et al.* reported O atoms are possibly adsorbed on both flat and defective surfaces of a AuNP [80, 81]. Shi *et al.* [82] showed that when surface of AuNPs is covered with O atoms, in addition to {111} and {100} facets, {110} facet become stable. These reports are consistent with the round morphology of AuNPs in O_2. In contrast to Au/CeO_2, AuNPs in Au/TiC never showed round morphology in O_2. This result suggests that dissociations of O_2 molecules seemed to occur at the perimeter interface between AuNPs and CeO_2 support [83-85].

Now, we discuss the facet morphology of AuNPs on CeO_2 in CO/air. The morphology diagram in Fig. 6.9 shows that surface of AuNPs is stable in high CO partial pressure. With decrease of the CO partial pressure, AuNPs turned to round morphology from facet morphology as shown in Fig. 6.4. From theoretical studies [80, 84, 86], CO molecules are adsorbed on both terraces and edges. Moreover, adsorbed CO molecules stabilize the surface of AuNPs [86]. From our experiments and these theoretical studies, we concluded that CO molecules stabilize the major {111} and {100} facets of AuNPs.

6.6 Summary

In summary, we have performed the systematic ETEM observation of AuNPs supported on CeO_2 in CO/air mixture for the first time. The ETEM observations have shown the morphology changes of AuNPs depending on the partial pressure of CO and O_2 gases. Establishing the morphology diagram, it is considered that 1) CO molecules are adsorbed on the surface of AuNPs, stabilizing AuNPs of polyhedron shape enclosed by the major {111} and {100} facet surfaces, 2) O_2 molecules are possibly dissociated at the perimeter interface, resulting in round morphology. AuNPs on CeO_2 show round morphology in O_2. On the other hand, AuNPs on TiC show facet morphology in O_2. The difference in morphology may indicate correlation between morphology of AuNPs and support materials. However, catalytic activities of the Au/TiC catalyst used in this experiment are unclear. To examine correlation among morphology of AuNPs in O_2 and CO/air, support materials and catalytic activities, we prepared AuNPs on CeO_2, SiO_2 and TiC and measured catalytic activities, then carried out ETEM observations in O_2 and CO/air. Details are shown in chapter 7.

Chapter 7

Morphology of AuNPs on CeO$_2$, SiO$_2$ and TiC in O$_2$ and CO/air

7.1 Introduction

It is known that the catalytic activities depend on support materials [81 and references therein]. Supports of Au catalysts involved in adsorptions and activations of O$_2$ molecules and supply of them to CO oxidations [11, 87, 88]. From computer simulations, O$_2$ molecules are hardly adsorbed at flat gold surfaces [80, 81], but they are stably adsorbed perimeter interfaces between AuNPs and supports [83, 85, 89]. O$_2$ molecules hardly dissociate into O atoms at the flat surface of gold [83]. Energy barriers of O$_2$ dissociations become lower at perimeter interfaces between AuNPs and supports, O$_2$ molecules easily dissociate into O atoms [83, 90]. As mentioned above, supports of Au catalysts involved in adsorptions and activations of O$_2$ molecules and supply of them to CO oxidations. However, details have been still unclear. To elucidate the origin of high catalytic activity of Au catalysts in CO oxidation, clarifying the role of supports is very important. ETEM observations of active Au/CeO$_2$ catalysts in CO/air and O$_2$ have revealed that AuNPs show facet morphology in CO/air and round

morphology in O_2 under electron irradiation [91] shown in chapter 6. The facet morphology of AuNPs in CO/air is interpreted that CO molecules are adsorbed at the surface of AuNPs and stabilize AuNPs with polyhedral shape enclosed by the major {111} and {100} facets. The round morphology in O_2 suggests O_2 molecules dissociation into O atoms. To examine the role of supports, comparison of morphology of AuNPs on various supports in O_2 and CO/air is a valid approach.

In this chapter, to examine whether AuNPs behavior in gases differ depending on support materials and catalytic activity, ETEM observations of AuNPs on CeO_2, SiO_2, TiC supports, which is known as reducible oxide, irreducible oxide and carbide respectively, in O_2 and CO/air were carried out. Correlations among morphology of AuNPs, support materials and catalytic activities are discussed.

7.2 Experimental procedure

Two Au/CeO_2 catalysts prepared by deposition precipitation (DP) method (Au/CeO_2-1 (sample preparations and a catalytic activity were reported in elsewhere [75]) which is the same sample used in chapter 6 and Au/CeO_2-2 (Haruta Gold Inc., RRCe-2)), a Au/SiO_2 catalyst prepared by deposition reduction (DR) method (Haruta Gold Inc., RR2Si) and a Au/TiC catalyst prepared by solid grinding (SG) method were used in this study. Most AuNPs on each support show polyhedral shape enclosed by the major {111} and {100} facets in vacuum. Au/CeO_2-1 is different from Au/CeO_2-2 in the

Au content and AuNPs size. The Au content was measured by inductively coupled plasma - atomic emission spectroscopy (ICP-AES). The content of Au/CeO_2-1, Au/CeO_2-2, Au/SiO_2 and Au/TiC was 5.00 wt%, 0.98 wt%, 1.00 wt% and 0.92 wt% respectively. The mean diameters of the AuNPs were estimated from HAADF-STEM to be 4.1 ± 1.3 nm for Au/CeO_2-1, 10.4 ± 2.2 nm for Au/CeO_2-2, 6.6 ± 2.7 nm for Au/SiO_2 and 5.7 ± 3.4 nm for Au/TiC respectively. Activities of the catalysts were measured using a fixed-bed flow reactor. A catalyst sample of 150 mg was used for pretreatment and catalytic measurement. Pretreatment gas was 20 vol% O_2 and 80 vol% He mixture and reactant gas was 1vol % CO, 20 vol% O_2 and 79 vol% He mixtuer. In pretreatment, the gas was fed at the rate of 50 ml/min at 250 ℃ for 1h. To prevent TiC support from oxidation, the pretreatment was not carried out in the Au/TiC catalyst. The catalytic activities were measured by passing the reactant gas at the rate of 50 ml/min, which corresponds to space velocity 20000 ml/h·$g_{cat.}$.

The samples were observed using an ETEM (FEI Tecnai F20 equipped with an E-cell) operated at 200 kV. Gaseous 1 vol% CO/air (1 vol% CO, 21 vol%O_2 and 78 vol% N_2) and O_2 were introduced into the environmental cell and the catalysts were observed at room temperature. The pressure of O_2 and CO/air was set at 1 mbar. We have confirmed that AuNPs on CeO_2 show typical morphology changes at the pressure [91] (Chapter 6). Using CCD camera, ETEM images of 1024 × 1024 pixels were recorded at 1 frame per 0.65 s. To minimize electron irradiation damage, samples were irradiated with electron fluxes smaller than 5.0 A/ cm^2 in each atmosphere during acquisition of 40 images (26

s) for Au/CeO$_2$-1, Au/CeO$_2$-2, Au/SiO$_2$ and 20 images (13 s) for Au/TiC.

7.3 Results

7.3.1 Dependency of catalytic activity on supports

To confirm catalytic activities of samples used in this experiment differ depending on support materials, CO to CO$_2$ conversions of Au/CeO$_2$-2, Au/SiO$_2$ and Au/TiC were measured at 30, 40, 50, 60 and 90 ºC (see Appendix B Fig. B.2).   As room temperature differs day to day, we employed not room temperature but 30 ºC which is near room temperature and controllable.   To compare catalytic activities with ETEM images acquired at room temperature, TOFs were calculated at 30 ºC which is near room temperature (Fig. 7.1). We employed the TOF of Au/CeO$_2$-1 measured before [75].   The TOF of Au/CeO$_2$-1 is the highest of the four.   That of Au/CeO$_2$-2 is higher than that of Au/SiO$_2$ and Au/TiC.   That of Au/TiC is the lowest of the four.   As can be seen, catalytic activities of the samples used in this experiment differ depending on support materials.
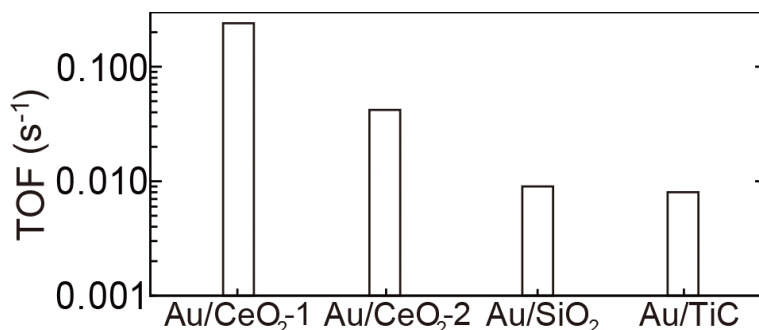
Figure 7.1: Turn over frequency (TOF) calculated from CO to CO_2 conversion at 30 ℃.

7.3.2 Dependency of morphology changes of Au nanoparticles in gases on supports

From ETEM observations of many AuNPs in each sample in O_2 and CO/air, there was a tendency that morphology changes of AuNPs differed depending on support materials (Fig. 7.2).   To examine the morphology changes of AuNPs on each support statically and quantitatively, we evaluated morphology of AuNPs in gases using relative morphology index M as described in chapter 6.   Though TEM images are projection images, we have confirmed that the morphology changes of AuNPs can be estimated using the relative morphology index in chapter 6.   When M of a AuNP is > 0.95, the AuNP is classified as having facet morphology, and round morphology when M is ≤ 0.95.   We determined the morphology of several (15-19) AuNPs in O_2 and CO/air and examined the tendency of morphology changes.   The tendency of morphology changes of AuNPs in O_2 and CO/air depended on support materials (Fig.7.3). The ratio of AuNPs which showed round morphology in O_2 and facet morphology in CO/air tends to be high in the highly active

catalysts.   In Au/CeO$_2$-1, most of AuNPs showed round morphology in O$_2$ and facet morphology in CO/air (75.0 %).   In Au/CeO$_2$-2, 44.4 percent of AuNPs showed round morphology in O$_2$ and facet morphology in CO/air and 38.9 percent of AuNPs showed facet morphology in both O$_2$ and CO/air.   On the other hand, in Au/SiO$_2$, 52.6 percent of AuNPs showed facet morphology in both O$_2$ and CO/air and 26.3 percent of AuNPs showed round morphology in O$_2$ and facet morphology in CO/air.   In Au/TiC, which showed the lowest catalytic activity of the four, most of AuNPs showed facet morphology both in O$_2$ and CO/air (75.0 %). From these results, there is a tendency that the ratio of AuNPs which show round morphology in O$_2$ and facet morphology in CO/air is high in highly active catalysts.   This indicates a possibility that the ratio of AuNPs which take part in catalytic activities differs depending on support materials.
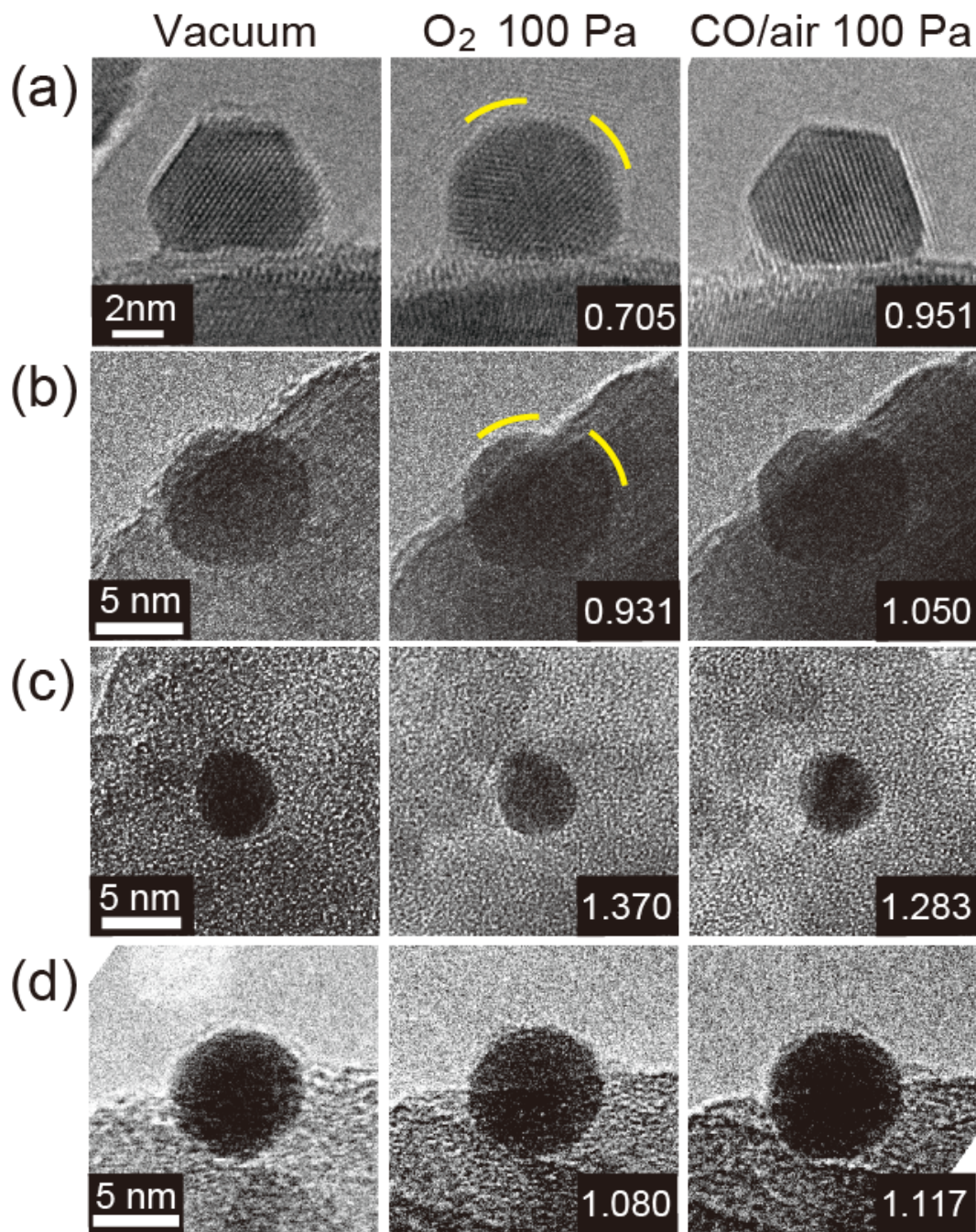
Figure 7.2: ETEM images of (a) Au/CeO$_2$-1 catalyst, (b) Au/CeO$_2$-2 catalyst, (c) Au/SiO$_2$ catalyst and (d) Au/TiC catalyst in vacuum, O$_2$ at 1 mbar and CO/air at 1 mbar. Morphology index M is shown at the bottom right in the images in O$_2$ and CO/air.
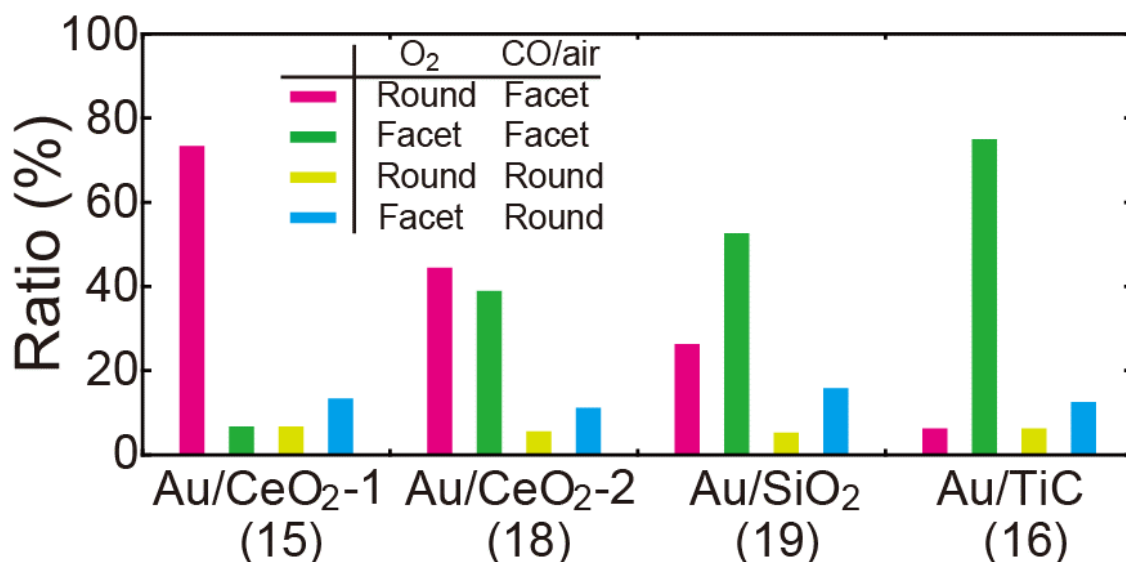
Figure 7.3: Morphology changes tendency of Au/CeO$_2$-1, Au/CeO$_2$-2, Au/SiO$_2$ and Au/TiC in O$_2$ at 1 mbar and CO/air at 1 mbar. The value in the figure shows the number of observed AuNPs.

In addition to the active AuNPs ratio, amount of oxygen supply from supports to AuNPs possibly affect catalytic activities. In that case, the amount of morphology change in O$_2$ is large in highly active catalysts. To investigate whether amount of oxygen supply from support differs depending on support materials, average M and standard deviation of all AuNPs was calculated (Fig. 7.4(a)) and a part of AuNPs which showed round morphology in O$_2$ and facet morphology in CO/air (Fig. 7.4(b)). First, we explain about average M and standard deviation of all AuNPs (Fig. 7.4(a)). Comparing average M in O$_2$, AuNPs of Au/CeO$_2$-1 became the roundest of the four. Average Ms of Au/CeO$_2$-2 and Au/SiO$_2$ were bigger than 0.95, which means AuNPs showed facet morphology. This was attributed to averaging all AuNPs including the AuNPs

which showed facet morphology in O_2.   Average M of Au/TiC was 1.17, which shows a tendency that AuNPs on TiC showed facet morphology in O_2.   Average Ms in CO/air of all samples were larger than 0.95, which corresponded to observations that most AuNPs of all samples showed facet morphology in CO/air.   Second, we explain about average M and standard deviation of the AuNPs which showed round morphology in O_2 and facet morphology in CO/air (Fig. 7.4(b)).   In O_2, average M of Au/CeO$_2$-2 was 0.86, that of both Au/CeO$_2$-1 and Au/SiO$_2$ was 0.81 and that of Au/TiC was 0.62.   The value of Au/TiC which tended to show facet morphology in O_2 was the lowest.   As only one AuNP in the ETEM observation of Au/TiC showed round morphology in O_2 and facet morphology in CO/air, this was attributed to peculiar behavior of the AuNP.   There was small difference in average M in O_2 among Au/CeO$_2$-1, Au/CeO$_2$-2 and Au/SiO$_2$.   In CO/air, there was little difference in average M among the samples.   As average Ms of all samples are almost same (Fig. 7.4(b)), it seems that the ratio of AuNPs which take part in CO oxidation reaction mainly affects catalytic activity.
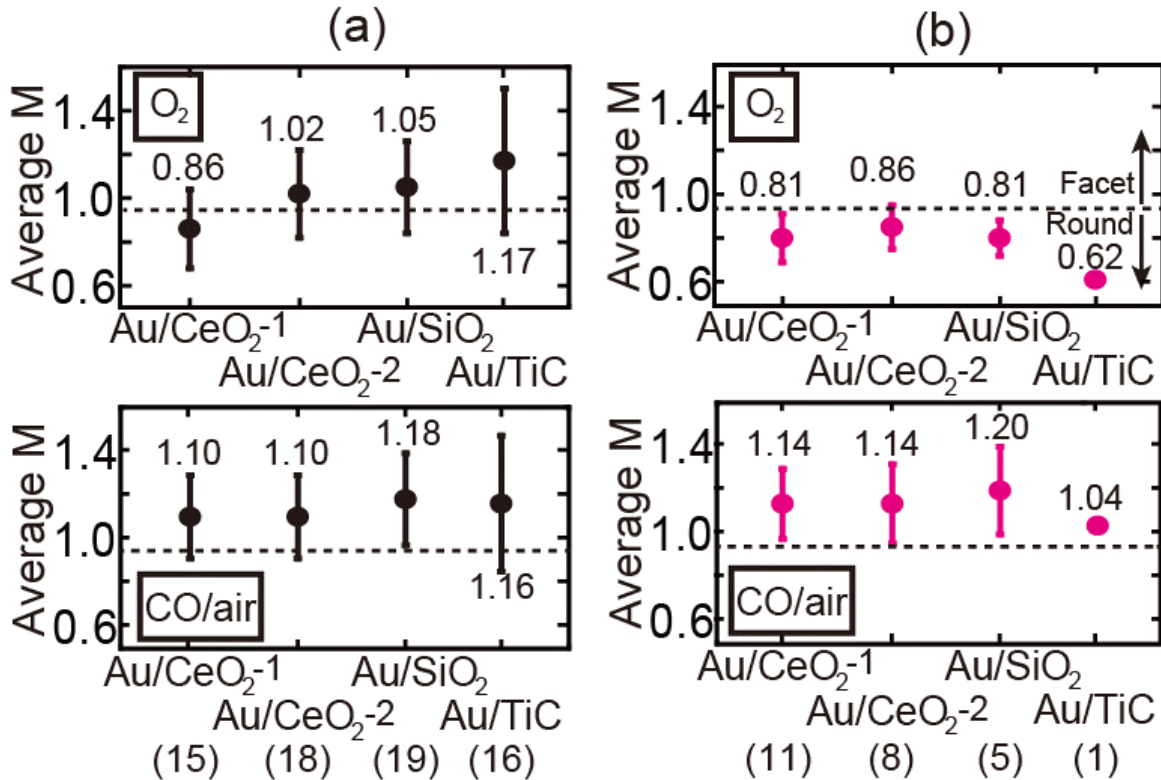
Figure 7.4: Average value of relative morphology index M in O_2 and CO/air of Au/CeO$_2$-1, Au/CeO$_2$-2, Au/SiO$_2$ and Au/TiC . (a) average of all AuNPs, (b) average of the AuNPs which show round morphology in O_2 and facet morphology in CO/air. The value listed below in the figures shows the number of AuNPs of each sample categorized in (a) and (b). Criteria values (M=0.95) which divide AuNPs facet or round is shown in the figures as dashed line.

It is known that activities of Au catalysts increase with the decrease in AnNPs size [11, 88]. To examine the difference in morphology changes in O_2 is derived from support materials by comparing same size AuNPs, Ms of each AuNPs in O_2 and CO/air were plotted against circle equivalent diameter (Fig. 7.5). First, Au/CeO$_2$-1 is compared to Au/SiO$_2$. Size of AuNPs of Au/CeO$_2$-1

and Au/SiO$_2$ was similar. Despite of same size range, the ratio of AuNPs which showed round morphology in O$_2$ of Au/CeO$_2$-1 was higher than that of Au/SiO$_2$. Second, Au/TiC is compared to Au/CeO$_2$-1 and Au/SiO$_2$. Au/CeO$_2$-1, Au/SiO$_2$ and Au/TiC contained 5 – 8 nm size AuNPs. Comparing *Ms* with each other in this size range, Au/TiC tended to show facet morphology in O$_2$. Finally, to examine the difference in the morphology change between Au/CeO$_2$-1 and Au/CeO$_2$-2, *Ms* of them are compared. Fig. 7.5 (a) shows tendencies that size of AuNPs of Au/CeO$_2$-1 was smaller than that of Au/CeO$_2$-2 and small AuNPs showed round morphology. Comparing *M* of round AuNPs between Au/CeO$_2$-1 and Au/CeO$_2$-2, there was little difference in *M* values in each AuNP. This is consistent with the result that average *M* was almost same (Fig. 7.4 (b)). In Au/CeO$_2$ catalysts, small AuNPs tended to show round morphology in O$_2$ and magnitude of the morphology changes was independent of AuNPs size. *M* value in CO/air of each sample was almost same and independent of AuNPs size. From these results, it can be said that the difference in morphology change of AuNPs in O$_2$ among Au/CeO$_2$, Au/SiO$_2$ and Au/TiC is derived from support materials and that of AuNPs in O$_2$ between Au/CeO$_2$-1 and Au/CeO$_2$-2 is derived from AuNPs size.
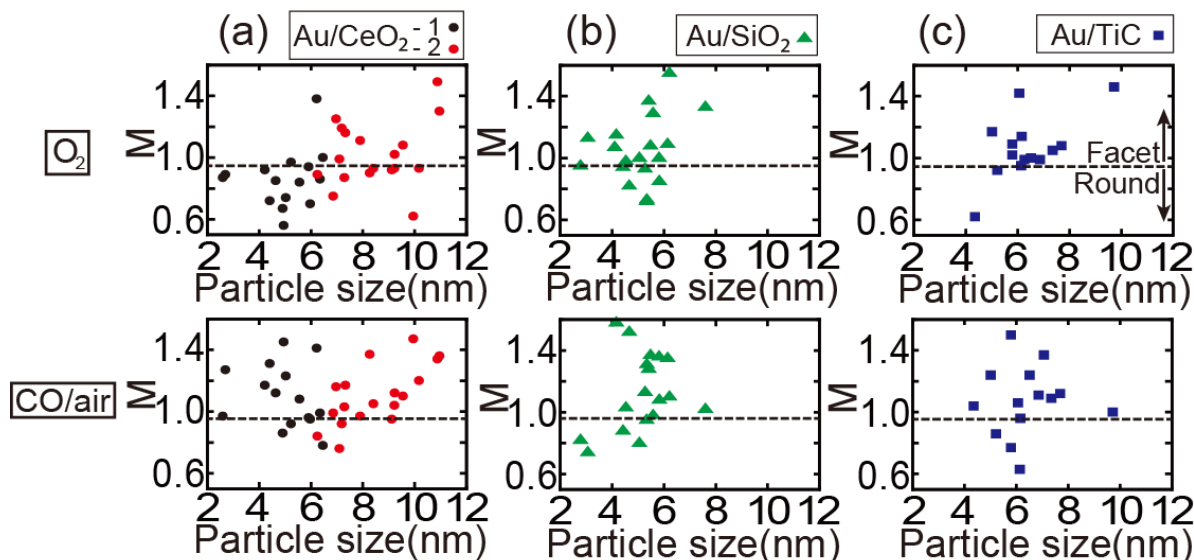
Figure 7.5: Size dependency of relative morphology index M in O_2 and CO/air. (a) Au/CeO$_2$-1 and Au/CeO$_2$-2 , (b) Au/SiO$_2$ (c) Au/TiC. The criteria value (M=0.95) which divides AuNPs facet or round is shown in the figures as dashed line. The mean diameters of the AuNPs are 4.1 ± 1.3 nm for Au/CeO$_2$-1, 10.4 ± 2.2 nm for Au/CeO$_2$-2, 6.6 ± 2.7 nm for Au/SiO$_2$ and 5.7 ± 3.4 nm for Au/TiC respectively.

7.4 Discussion

7.4.1 Correlation of catalytic activities, active Au nanoparticles and supports

Now, we discuss correlations among catalytic activities, morphology of AuNPs and support materials. The experiments clearly showed a tendency that the higher catalytic activity is, the higher the ratio of AuNPs which show round morphology in O_2 and facet morphology in CO/air is. It can be considered that active AuNPs show round morphology in O_2 and facet morphology in CO/air. Though

dissociation of O_2 molecules into O atoms in Au catalysts has been discussed [77, 84, 86-90], round morphology in O_2 is considered to arise from covering AuNPs surface with O atoms [82, 91]. AuNPs on any support show facet morphology in CO/air (Fig. 7.4). On the other hand, in highly active catalysts, the ratio of AuNPs which show round morphology in O_2 and facet morphology in CO/air is high (Figs. 7.3, 7.5). These results indicate that supply capabilities of oxygen, especially O atoms, from supports to AuNPs influences morphology changes in O_2 and catalytic activities.

7.4.2 Origin of support dependent catalytic activity

Now, we discuss non-uniform morphology changes of AuNPs in each sample. O vacancies in support, charge transfer between AuNPs and supports and coherency between AuNPs and supports possibly relate to non-uniform morphology changes of AuNPs in each sample. Computational simulations have revealed that O vacancies in the vicinity of AuNPs help supports to bound AuNPs strongly [98-101]. In that case, electrons transfer from support to AuNPs [98, 99, 101]. The negatively charged AuNPs tend to adsorb CO and O_2 molecules strongly [98]. Strong O_2 adsorptions at O vacancies lower O_2 dissociation barrier [85, 89]. It has been proposed that if AuNPs and support are coherent, AuNPs are adsorbed to supports strongly and become hemisphere, resulting in maximization of perimeter interface and high catalytic activities [11]. Typical orientation relationship between AuNPs and supports has been reported in Au/CeO_2 and Au/TiO_2 catalysts [76, 102, 103]. Furthermore, there may exist an interfacial structure which promotes adsorptions and dissociations of O_2 molecules and CO oxidation.

AuNPs which have the structure are active and show round morphology in O_2 and facet morphology in CO/air. Au/CeO$_2$ catalysts may tend to have the structure in typical orientation relationship, resulting in high ratio of active AuNPs. Considering the Au/SiO$_2$ catalyst, as SiO$_2$ is amorphous structure, it seems to be no specific interfacial structure. There is some possibility of existence specific interfacial structure which promotes adsorptions and dissociations of O_2 molecules and CO oxidation, resulting in moderate ratio of active AuNPs. Considering the Au/TiC catalyst, orientation relationship of Au/TiC catalysts was also reported [104]. The interfacial structure of Au/TiC hardly promotes adsorptions and dissociations of O_2 molecules and CO oxidation, resulting in little ratio of active AuNPs. In sample preparations, Au/CeO$_2$, Au/SiO$_2$ and Au/TiC tend to take the interfacial structures as described above, resulting in difference in the ratio of active AuNPs. However, correlation between the coherency and catalytic activities remains uncertain. There is some possibilities that amount of O vacancies at the support surfaces and stoichiometry at interface between AuNPs and support change depending on sample preparation method and calcination conditions such as atmosphere and temperature, details have been still unclear. As described above, O vacancies in support, charge transfer between AuNPs and supports and coherency between AuNPs and supports may be related to non-uniform morphology changes of AuNPs in each sample. However, it is difficult to conclude the cause of the non-uniform morphology changes of AuNPs from our experimental results. Further insight into these aspects is left to future work.

7.5 Summary

Our ETEM observations of AuNPs on CeO_2, SiO_2 and TiC support in O_2 and CO/air has shown the tendency that morphology changes of AuNPs differ depending on support materials. The ratio of AuNPs which show round morphology in O_2 and facet morphology in CO/air tends to high in highly active catalysts. On the other hand, the ratio tends to low in low active catalysts. Round morphology in O_2 possibly correlates to O atoms adsorptions on AuNP surface. It is considerable from these results that not all AuNPs but parts of AuNPs contribute to catalytic reactions, and the ratio of AuNPs which take part in catalytic reactions affects catalytic activity. Interfacial structure of AuNPs and supports possibly relate to the ratio. However, further insight into these aspects is left to future work. Elucidating factors which determine each AuNP active or not lead to investigate more active Au catalysts. Moreover, these findings may bring general understanding of support role, especially its role in oxygen activation and supply in CO oxidation.

Chapter 8

Discussion about the reaction mechanism of Au catalysts

In this chapter, we will compare the results shown in chapter 6 and 7 with three reaction models which have been proposed. Theoretical studies of Au catalysts are also reviewed. Then, we will discuss the reaction mechanism of CO oxidation of Au catalysts more deeply.

8.1 Brief review of reaction models of Au catalysts

First, we will explain the reaction models which have been proposed before. There is a controversy over the reaction mechanism. There are three models for the reaction mechanism of Au catalysts [11,31–34]. Features of these three models are summarized in Table 8.1. Haruta and his coworkers propose that the perimeter interface between AuNPs and the support is active sites [11] (perimeter model). For more details, CO molecules are adsorbed at edges and corners of AuNPs [74], and O_2 molecules are adsorbed at the perimeter interface between AuNPs and support [99–101]. Adsorbed CO molecules diffuse from the surface of AuNPs to the perimeter interface, and CO oxidation occurs at the perimeter interface. It is also said that O vacancies of support contribute to

adsorption of O_2 molecules and CO oxidation. Goodman and his coworkers claimed that a bilayer structure of Au on a highly reduced TiO_2 surface exhibits a significantly higher catalytic activity for CO oxidation than AuNPs [31,32] (two layers model). They suggest that the charge and quantum size effects in a Au bilayer, especially at low-coordinated gold atoms, contribute to the catalytic activities. Defects in the metal oxide support are thought to play an important role in anchoring the AuNPs and in transformation of electrons from the support to AuNPs. Stephanopoulos and her coworkers propose that Au cations promote reactions [33,34] (Au cation model). They deposited Au on a nanometer-sized La-doped CeO_2. Though they removed metallic AuNPs on the CeO_2 by cyanide leaching, the catalytic activity remains almost the same before and after cyanide leaching. From the result, they suggested that Au cations play an important role in the catalytic activities. The surface defects of ceria support are thought to play a key role in anchoring Au and turn as the active sites.

Now, we compare these models in terms of adsorption sites and active sites. First, adsorption sites of O_2 molecules are compared. In perimeter model, O_2 molecules seem to be adsorbed at perimeter interface between AuNPs and support [11]. It is also said that O vacancies contribute to adsorptions of O_2 molecules. In two layers model and Au cation model, adsorption sites of O_2 molecules are not written clearly [31–34]. However, in two layers model, two layer Au cluster tends to become (1 x 3) structure [32]. O_2 molecules are possibly adsorbed at perimeter interface (Fig.6 of [32]). Next, we compare these models in terms of adsorption sites of CO molecules.

In perimeter model, CO molecules seem to be adsorbed at edges and corners of AuNPs [11]. As Au atoms at edges and corners of AuNPs are low coordination number, they tend to adsorb CO molecules [80, 87, 107, 108]. In two layers model and Au cation model, adsorption sites of CO molecules are not written clearly [31–34]. However, in two layers model, two layer Au cluster tends to become (1 x 3) structure [32]. CO molecules are possibly adsorbed at edges and corners of two layer Au cluster (Fig.6 of [32]). In perimeter model, active sites seem to be perimeter interface between AuNPs and support [11]. In two layers model, adsorption sites of active sites are not written clearly [31–34]. As two layer Au cluster tends to become (1 x 3) structure [32], CO oxidation possibly occurs at perimeter interface between two layer Au cluster and support (Fig.6 of [32]). In Au cation model, they claimed that strongly bound Au on ceria is active site.

Now, we explain contributions of O vacancies, charge transfer, size effects and low coordination number sites of AuNPs which are relate to catalytic activity in each model. First, we will explain the contributions of O vacancies and charge transfer to CO oxidation. In perimeter model, O vacancies relate to adsorption of O_2 molecules and CO oxidation. Charge transfer to AuNPs also seems to occur and relate to catalytic activity. However, charge transfer is not necessary to the reaction in this model. In two layers model, defects in the oxide support are thought to play an important role in anchoring the AuNPs and in transformation of electrons from the support to AuNPs. They claimed that Au becomes $Au^{\delta-}$ [32]. In Au cation model, the surface defects of ceria support are thought to play a key role in anchoring Au and turn as the active sites. They

claimed that Au^+ and Au^{3+} relate to CO oxidation [33,34]. Second, we will explain the contributions of size effect and low coordination number sites of AuNPs to CO oxidation. When the size of AuNPs become small, the density of corner, edge and surface Au atoms increases. It is also reported that when AuNPs become two layers, the electronic state of AuNPs change [31]. In perimeter model, the density of corner, edge, or surface Au atoms increases with decreasing particle size. As a result, more CO molecules tend to be adsorbed. In two layers model, the electronic state of AuNPs change. Moreover, Au (1 x 3) structure has much edges and corners (Fig.6 of [32]). In Au cation model, the necessities of size effect and low coordination number sites of AuNPs were not written.

Here, we want to clear things to be solved. Experimental results using FTIR [105] and computer simulations support that CO molecules are adsorbed at edges and corners of AuNPs [80,84,107,108]. Adsorptions of O_2 molecules are hard to occur at the surface of AuNPs [74] and possibly occur at the perimeter interface [83-85,106,109,110]. Moreover, it was reported by theoretical studies that energy barrier of the reaction become lower at the perimeter interface [83-85,89]. These results support perimeter model. However, it has not been concluded that O_2 molecules are really adsorbed at perimeter interface. There are arguments that O_2 molecules dissociate into O atoms or not in adsorption. This is very important to elucidate the reaction mechanism of CO oxidation. Moreover, it has not been concluded that active sites are perimeter interface.

Table 8.1: Features of perimeter model, two layers model and Au cation model.

	Perimeter model [7]	Two layers model [28,29]	Au cation model [30,31]
O adsorption sites	Perimeter interface	——	——
CO adsorption sites	Edges and corners	——	——
Active sites	Perimeter interface	——	Strongly bound gold in support
Contributions of support defects	Yes (espetially O vacancies)	Yes	Yes
Charge transfer	Not necessary	Yes (Negatively charged)	Yes (Positively charged)
Size effect	Yes	Yes	——
Contributions of low coordination number sites	Yes	Yes	——

—— Not clearly written in papers

8.2 Brief review of theoretical studies of Au catalysts

To understand the reaction mechanism of Au catalysts, many theoretical studies have been carried out. Here, we will summarize these results to discuss the reaction mechanism of Au catalysts in section 8.3.

8.2.1 Adsorption of CO molecules

Adsorption of CO molecules at the surface of Au

First, we will show computer simulation results of adsorption of CO molecules to the surface of Au. Mavrikakis *et al*. have considered the three models shown in Fig.8.1 [80]. They have calculated binding energies of CO, O and O_2 to Au surfaces. The results are shown in Table 8.2. CO molecules bind stronger on Au(211) as a model for a stepped Au surface than a four-layer Au(111) slab and a two-layer Au cluster with a total of 18 Au atoms.

Lopez *et al*. have calculated the binding energies of CO, O and O_2 on Au(111), Au(211) and a small Au cluster [107]. The results are shown in Fig.8.2. When the coordination number of Au atoms is low, CO molecules are adsorbed strong. From these results, they conclude that support-independent increase in the catalytic activity with AuNPs size is the concentration of low-coordinated sites.
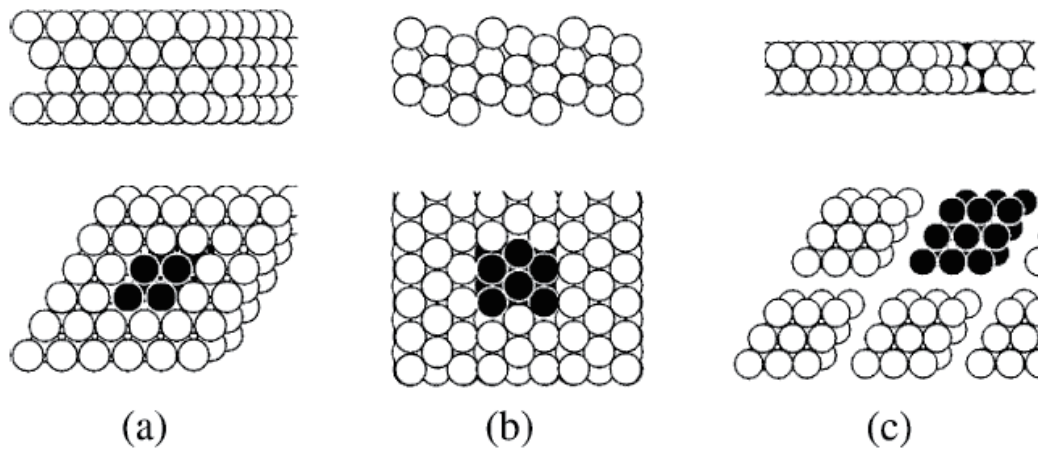
Figure 8.1: (a) a four layer Au(111) model, (b) a nine layer Au(211) model and (c) a Au cluster model used in calculations [80].

Table 8.2: Binding energies for CO, O and O_2 on Au(111), Au(211) and a small Au cluster [80].

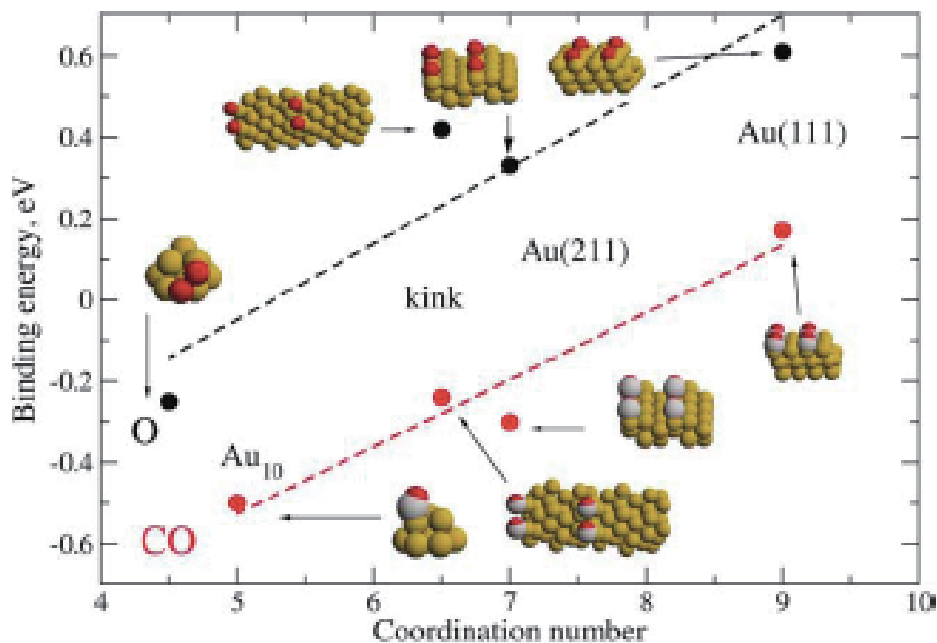|	CO/Au	O/Au	O_2/Au
Au(111)	−0.30 (t)	+0.18 (f)	No adsorption
Au(211)	−0.66 (b)	+0.02 (f)	−0.12 (2-fold, ∥)
Au cluster	−0.07 (t)	+1.54 (f)	No adsorption

Figure 8.2: Dependency of the binding energies of CO molecules and O atoms on the coordination number of Au atoms [107].

Adsorption of CO molecules at the surface of Au clusters on support

Next, we will show computer simulation results of adsorption of CO molecules to the surface of AuNPs on support. Molina and Hammer used Au rod/MgO (100) model and Au_{34} cluster/MgO(100) model. They have calculated adsorption energy of CO to edge of Au rod and edges ([86], [111]) and corners of Au_{34} cluster [84]. Fig. 8.3 and Table 8.3 show the results using Au rod/MgO(100) model and Fig. 8.4 shows the results using Au_{34} cluster/MgO(100) model. In both models, CO molecules are adsorbed stronger at edges than at facet.
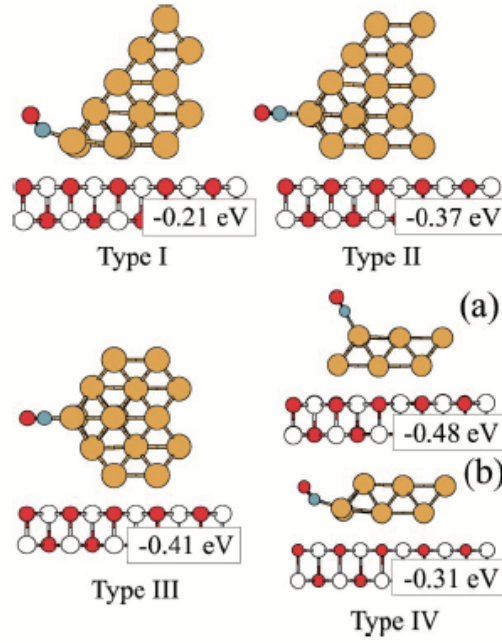
Figure 8.3: Calculation results of stable sites and energies of CO [86].

Table 8.3: Adsorption energies of CO (in eV) [86]

	Type I	Type II	Type III	Type IV (a)
RPBE	−0.21	−0.37	−0.41	−0.48
PW91	(−0.50)	(−0.69)	(−0.72)	−0.80

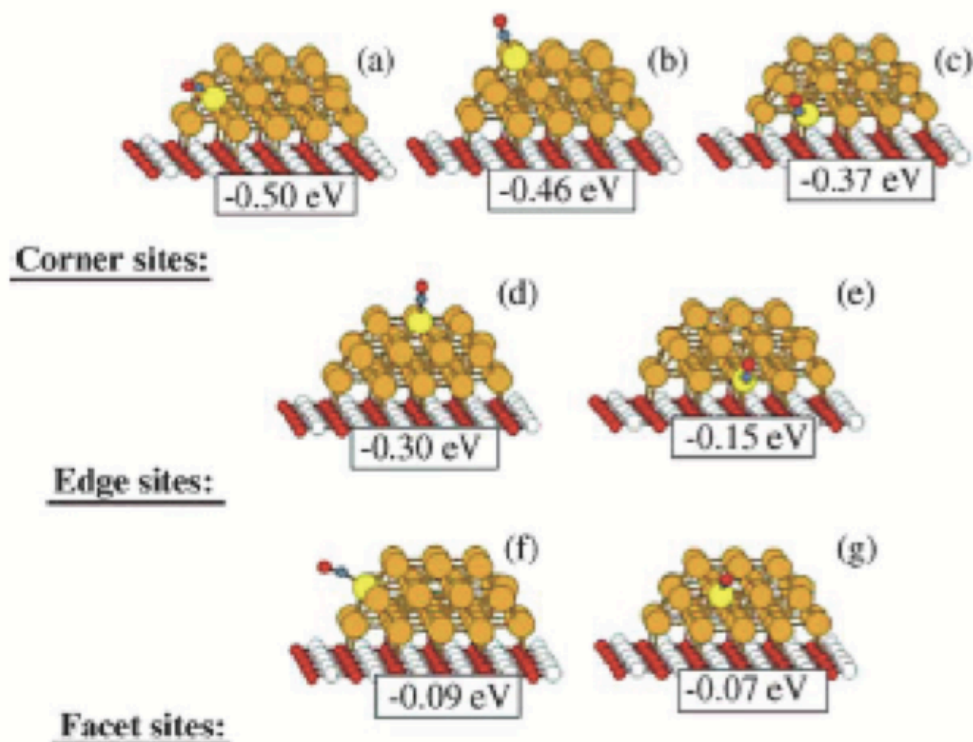|	Type IV (b)	2 ML Au/MgO	Au(100)	Au(111)
RPBE	−0.31	−0.21	−0.21	+0.02
PW91	(−0.61)	(−0.62)	(−0.60)	(−0.26)

Figure 8.4: Adsorption energies of a CO molecule on Au$_{34}$ cluster [84].

Summary of adsorption of CO molecules

Calculation results for CO adsorptions of each paper are summarized in Table 8.4. CO molecules are adsorbed at edges and corners strongly, which are low coordination number. On the other hand, they are adsorbed at (111) and (100) planes weakly.

Table 8.4: CO adsorption energy shown in each paper.   Unit is eV.
t: top, b: brige site

	Au surface			Au cluster		
	Au(111)	Au(100)	Au(211)			
Au	-0.30 (t)	—	-0.66 (b)	-0.07 (t) (Au_{18} cluster)		
Au	-0.28	-0.38	-0.54			
Au/TiO_2				-1.69 (no layer)	-1.24 (TiO_2 6 layers)	-1.38 (TiO_2 9 layers)
Au_{34}/MgO				-0.37 – -0.50 (corner)	-0.15/-0.30 (edge)	-0.07/-0.09 (facet)

8.2.2 Adsorption of O_2 molecules and O atoms

Adsorption of O_2 molecules and O atoms to the surface of Au

Mavrikakis *et al*. have calculated the adsorption energy of O_2 molecules and O atoms to various surface of Au.   They have reported that O_2 molecules and O atoms tend to be adsorbed at Au (211) which correspond to step or edge site (Fig. 8.2) [111].   Xu *et al*. also have reported same results (Table. 8.5) [112].   According to Mills *et al*. [113], O_2 molecules are not adsorbed at flat surface of Au.

Table 8.5: Adsorption energy of O atoms and O_2 molecules to {111} and {211} surfaces of Au. n/a: not adsorbed [112]

| | | Atomic Oxygen | | | |
surface	stretched (%)	site	E_b (eV)	z (Å)	d_{Au-O} (Å)
(111)	0	fcc	−2.54	1.33	2.16
(111)	10	fcc	−3.14	1.03	2.14
(211)	0	f0	−2.77	0.91	2.03
(211)	10	f2	−3.07	1.06	2.13

| | | Molecular Oxygen | | | |
surface	stretched (%)	E_b (eV)	z (Å)	d_{O-O} (Å)	μ (μ_B)
(111)	0	n/a			
(111)	10	−0.08	2.13	1.29	1.2
(211)	0	−0.15	2.07	1.29	1.2
(211)	10	−0.26	1.93	1.30	1.0

Adsorption of O_2 molecules to the surface of Au cluster on support

Molina and Hammer used Au rod/MgO(100) model and Au_{34} cluster/MgO(100) model. They have calculated adsorption energy of O_2 molecules to edges and corners of Au_{34} cluster [84]. Fig.8.3 and Table 8.3 shows the results using Au rod/MgO(100) model and Fig.8.5 shows the results using Au_{34} cluster/MgO(100) model. O_2 molecules are adsorbed on Au_{34} cluster weakly. Adsorption energy of O_2 molecules ranged 0 to +0.4 eV.
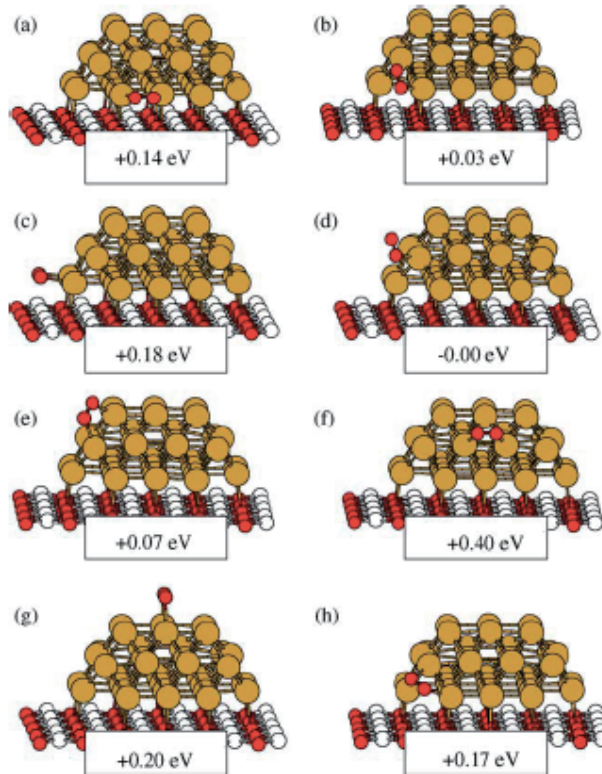
Figure 8.5: Adsorption energies of an O_2 molecule on Au_{34} cluster [84].

Adsorption of O_2 molecules at the perimeter interface between AuNPs and metal oxide support

Liu *et al.* used Au/TiO_2 (110) model and calculated the adsorption of CO molecules to Au atoms and O_2 molecules to perimeter interface. They also calculated CO oxidation [83]. O_2 molecules are adsorbed at perimeter interface of Au/TiO_2(110) stronger about 0.6 eV than at Au without support. Fig.8.6 and Table 8.6 show the results.

Table 8.6: Adsorption energies of CO and O_2 molecules at the perimeter interface of Au/rutile-TiO_2(110) and at Au without support. Unit is eV [83].

	Nonsupported Au	Au/TiO$_2$(110)	
		Six-layer TiO$_2$	Nine-layer TiO$_2$[a]
$E_{ad}(O_2)$	0.07 (0.00)	0.86 (1.03[a])	0.60
$E_{ad}(CO)$	1.69	1.24	1.38
$E_a(O_2 \rightarrow 2O)$	> 2	0.52	
$E_a(CO + O_2 \rightarrow CO_2 + O)$	0.78 (0.73)	0.10	0.17

Molina *et al.* also calculated the adsorption of O_2 molecules at the surface of Au rod /TiO_2(110) model [108]. When Au does not exist, O_2 molecules cannot be adsorbed at the surface of TiO_2(110). On the other hand, O_2 molecules are adsorbed at the perimeter interface of Au/TiO_2(110) strongly. Remediakis *et al.* calculated adsorption of O_2 molecules at the perimeter interface of Au_{10} cluster /rutile-TiO_2(110) [85, 108]. When O_2 molecules bond to Au(5) and Ti(7) shown in Fig.8.7, O_2 molecules are adsorbed most stably. That is, O_2 molecules are adsorbed at perimeter interface more stably than at Au atoms of low coordination number.

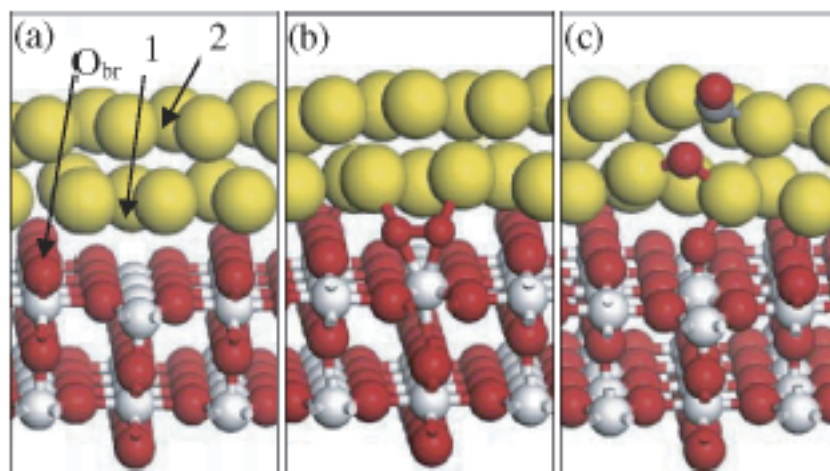Figure 8.6: (a) Au/rutile-TiO$_2$(110) model and adsorption site of it. Site 1 and site 2 show perimeter interface and Au atom respectively. (b) Adsorption of O$_2$ molecules to perimeter interface. (c) Reaction process of adsorbed CO and O$_2$ molecules [83].
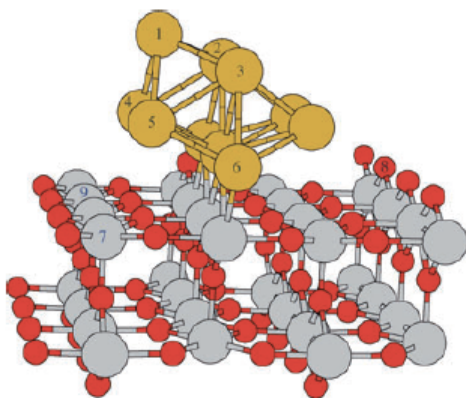

Figure 8.7: A model of an Au$_{10}$cluster supported on reduced rutile TiO$_2$(110). Yellow, gray, and red spheres correspond to Au, Ti, and O atoms, respectively [108].

Morphology changes of AuNPs by the adsorption of O atoms

Shi *et al.* carried out density-functional theory calculations to investigate the adsorption of oxygen at the Au(100), Au(111) and Au(110) surfaces (Fig. 8.8) [82]. The results are summarized as follows. They used the Wulff construction to predict the nanoparticle morphology. The oxygen chemical potential depends on pressure p and temperature T. At low chemical potential value (-0.5 eV), the (111) and (100) facets are dominant. With increasing the value, the (111) facets become covered with O, and the (110) regions with the (2 x 1)-2O/ (110) surface become larger and finally dominate. Shi *et al.* proposed from their calculations that the oxidized structures on the (111) and (110) surfaces possibly correlate with low temperature oxidation reactions.
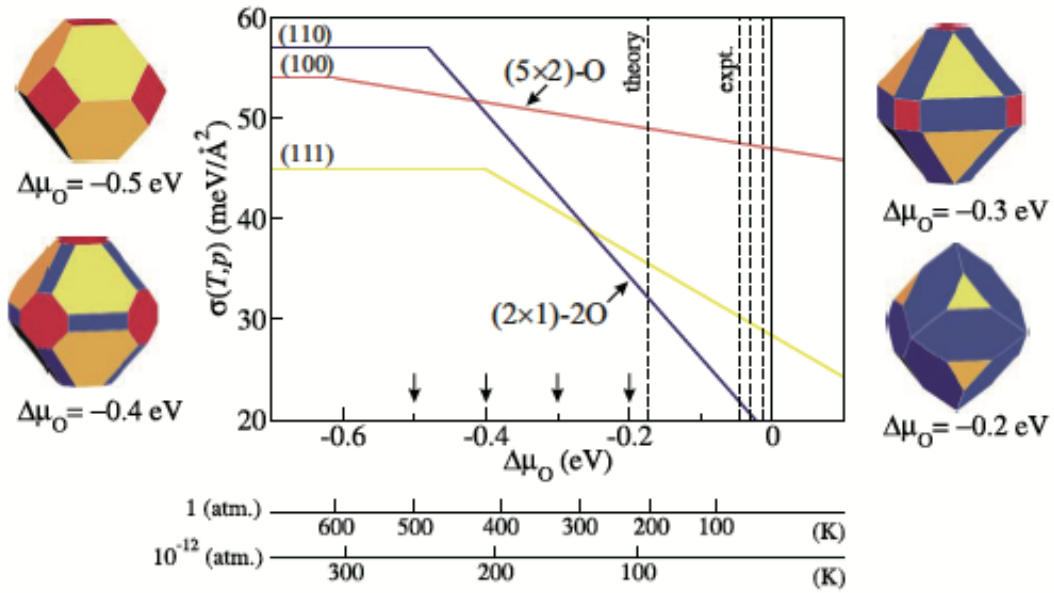
Figure 8.8: Dependency of surface free energies for O at Au (100), Au (110) and Au (111) on the oxygen chemical potential. The predicted nanoparticle shapes of -0.5, -0.4, -0.3 and -0.2 eV of the oxygen chemical potential are also shown. The facets are colored as red for (100), blue for (110) and orange for (111) [82].

Summary of adsorption of O_2 molecules

O_2 molecules are hardly adsorbed at flat surface of Au. On the other hand, they tend to be adsorbed at step edge such as (211) surface. Moreover, they are adsorbed stably at the perimeter interface between AuNPs and support.

Table 8.7: O_2 adsorption energy shown in each paper. Unit is eV.

	Au surface			Au cluster		
	Au(111)	Au(100)	Au(211)			
Au	no adsorption	—	-0.12 (2-fold)	no adsorption (Au_{18} cluster)		
Au	no adsorption	—	-0.15			
Au/TiO_2				-0.07 (no layer)	-0.86 (TiO_2 6 layers) (Interface)	-0.60 (TiO_2 9 layers) (Interface)
Au/TiO_2				-0.10 – -0.45 (Interface)	-0.64 – -1.65 (Interface) (O vacancy)	
Au rod /MgO				+0.05 – +0.21 (edge)		
Au_{34}/MgO				-0.00 – +0.40		

8.2.3 CO oxidation

Au/rutile-TiO_2(110) models used in three groups are shown in Fig.9.9((a) Molina *et al*. [108] (b) Liu *et al*. [83] (c) Remediakis *et al*. [85]). In these papers, O_2 molecules are adsorbed at perimeter interface, and CO molecules are adsorbed at Au cluster. Then, adsorbed CO molecules diffuse to perimeter interface and react with O_2 molecules.
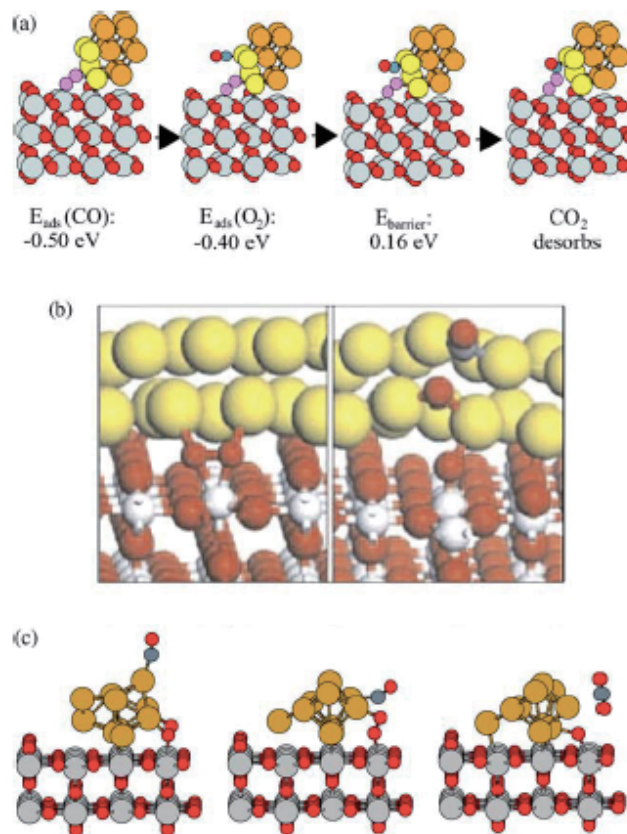
Figure 8.9: Au/rutile-TiO$_2$(110) model shown in each papers (a) Molina *et al.* [108] (b) Liu *et al.* [83] (c) Remediakis *et al.* [85]. Au,Ti,O atoms are represented by yellow, grey and red sphere respectively.

Chen *et al.* summarized catalytic cycle of CO oxidation at the perimeter interface of Au/m oxide considering these three models shown above and energy barrier in reaction (Fig.8.10) [115].

1. A CO molecule is adsorbed at Au cluster.

2. An O$_2$ molecule is adsorbed at perimeter interface

3. A CO molecule reacts with an O_2 molecule to produce a CO_2 molecule. Then the CO_2 molecule desorbs.

4. Remaining an O atom react with another CO molecule. One cycle for CO oxidation finishes.
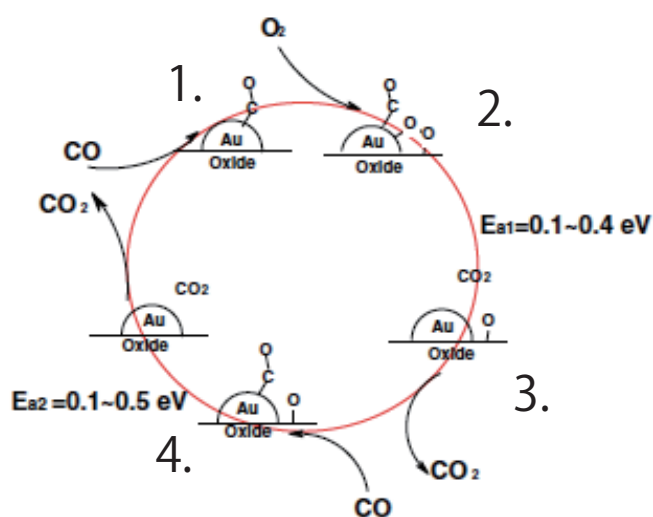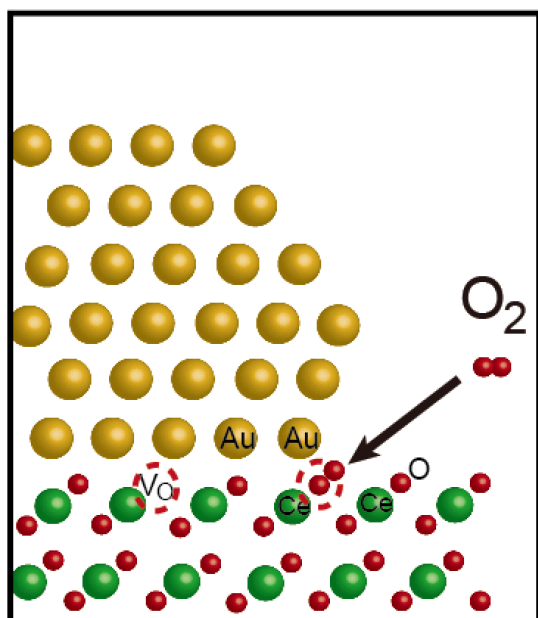

Figure 8.10: Proposed model by Chen *et al.* [115].

8.3 Discussion about reaction mechanism of CO oxidation over Au catalysts

In this section, we will compare our experimental results with previous studies and discuss the reaction mechanism of CO oxidation over Au catalysts.

Adsorption sites of O_2 molecules

We observed active Au/CeO_2 catalysts in O_2 and CO/air. We have found that AuNPs on CeO_2 become round in O_2 and faceted in CO/air. Adsorption sites of O_2 molecules are considered as follows. Some experimental results that O_2 molecules are adsorbed at perimeter interface have been reported [104–106]. However, in these reports, it is unclear whether O_2 molecules dissociate into O atoms or not. Some theoretical results that O_2 molecules tend to be adsorbed at perimeter interface also have been reported [83–85,89]. In addition, there are same arguments that O_2 molecules are captured at O vacancies of the support. From our observations and both experimental and theoretical reports, we think adsorptions of O_2 molecules are as follows; $O_2 + [Vo]^- \rightarrow Vo[O_2]^-$ (Fig.8.11).

Figure 8.11: Schematic illustration of O_2 adsorption. Captions in the schematic illustration show grounds. The color means as follows. Green: our experiments, Blue: referred experimental studies, Red: referred theoretical studies.

The origin of rounded morphology is considered as follows. Shi *et al*. reported that when the surface of AuNPs is covered with O atoms, (110) planes of AuNPs become stable [82]. Liu *et al*. also reported that energy barrier of dissociation of O_2 molecules adsorbed at perimeter interface becomes lower [83]. From our experimental results and these papers, we consider that high index planes also become stable when the surface of AuNPs is covered with O atoms. AuNPs show multi faceted shape. Therefore, they looks round. On the other hand, in Au/TiC catalysts which show much less activity in CO oxidation, AuNPs on TiC show faceted shape in O_2.

From these results, the role of support is adsorption of O_2 molecules and dissociation of them into O atoms. It can be relate to the origin of support effects. It possibly seems that O vacancies of support contribute to the adsorption and dissociation of O_2 molecules. Now, it may happen that trapped $[O_2]^-$ ions can be dissociated by the aid of electron irradiation as follows; $Vo[O_2]^- + 2\ e^- \rightarrow Vo + 2\ [O]^-$ (Fig.8.12).
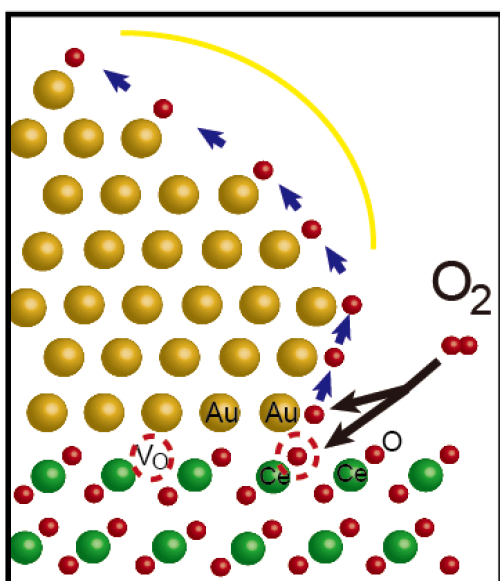
It may happen that trapped $V_o[O_2]^-$ ions can be dissociated by the aid of electron irradiation.

$$V_o[O_2]^- + 2\ e^- \longrightarrow V_o + 2[O]^-$$
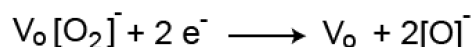
Our observation of Au/CeO$_2$ and Au/TiC in O$_2$.

H. Shi et al. [82]

Figure 8.12: Schematic illustration of dissociations of O_2 molecules. Captions in the schematic illustration show grounds. The color means as follows. Green: our experiments, Red: referred theoretical studies.
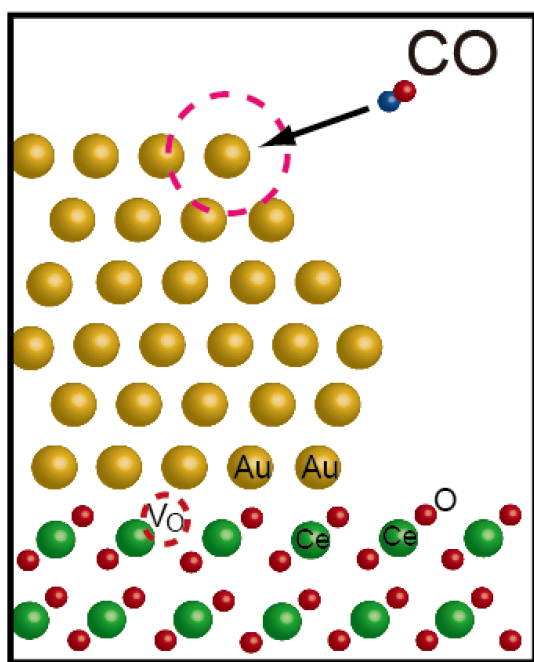
In perimeter model, adsorption sites of O_2 molecules seem to be perimeter interface between AuNPs and support. In two layers model and Au cation model, adsorption sites of O_2 molecules are not

clearly written. However, in two layers model, two layer Au cluster tend to become (1 x 3) structure [32]. In that structure, O_2 molecules are possibly adsorbed at perimeter interface (Fig.6 of [32]). Therefore, our experimental results related to adsorption sites of O_2 molecules are consistent with perimeter model.

Adsorption sites of CO molecules

In order to find out the origin of morphology change, following observations were carried out in chapter 6. We gradually decreased CO partial pressure in the mixed gas of 1vol.%CO/air and air. The total pressure of the mixed gas was kept at 3 mbar. First, we confirmed that AuNPs showed faceted shape in both vacuum and 1vol.% CO/air of 3 mbar (CO 0.03 mbar, air: 2.97 mbar)(Fig.6.3). Then, we decreased the partial pressure of CO from 0.03 mbar to 0 mbar through 0.01, 0.001, 0.0002 mbar. As shown in Fig.6.3, the facets of AuNPs gradually disappeared and turned to be round. We carried out similar observations using the mixed gas of 1vol.% CO/air and air. The total pressure of the mixed gas was kept at 3 mbar. First, we confirmed that AuNPs showed faceted shape in both vacuum and 1vol.% CO/air of 3 mbar (CO 0.0003 mbar, air: 2.9997 mbar)(Fig.6.4). Then, we decreased the partial pressure of CO from 0.0003 mbar to 0 mbar through 0.0001, 0.00001, 0.000002 mbar. As shown in Fig. 6.4, we obtained same results. That is, the facets of AuNPs gradually disappeared and turned to be round with the decrease of CO partial pressure. From these observations, we conclude that AuNPs are round in air while they are faceted in CO/air when the partial pressure of CO was higher than a certain

pressure. It is most likely that the adsorption of CO molecules on the surface of AuNPs stabilizes the facets. As reported before [68], CO molecules are adsorbed at the edge of AuNP. Theoretical studies also reported that CO molecules tend to be adsorbed at edges and corners of AuNPs [80,84,94,97,107,108]. From the observations and both experimental and theoretical reports, we think adsorptions of CO molecules are as follows; $CO + Au^{edge} \rightarrow CO(a)$ (Fig.8.13).
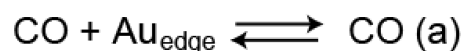
Figure 8.13: Schematic illustration of CO adsorption. Au_{edge} and CO(a) show Au atoms at edge of AuNPs and adsorbed CO molecules respectively. Captions in the schematic illustration show grounds. The color means as follows. Green: our experiments, Blue: referred experimental studies, Red: referred theoretical studies.

In perimeter model, adsorption sites of CO molecules seem to be edges and corners of AuNPs. In two layers model and Au cation model, adsorption sites of CO molecules are not clearly written. CO molecules are possibly adsorbed at edges and corners of two layer Au cluster with (1 x 3) structure (Fig.6 of [32]). Therefore, our experimental results related to adsorption sites of CO molecules are consistent with perimeter model.


Active sites

Our experimental results clearly show that AuNPs show faceted shape in CO oxidation. We carried out systematic observations of Au/CeO$_2$ catalysts in various ratios of CO molecules and O$_2$ molecules. The facets of AuNPs gradually disappeared and turned to be round with the decrease of CO partial pressure. From these observations, it was concluded that AuNPs are round in air while they are faceted in CO/air when the partial pressure of CO was higher than a certain pressure. It is most likely that the adsorption of CO on the surface of AuNPs stabilizes the facets. We consider that O atoms are used in CO oxidation at the perimeter interface, they cannot cover whole surface of AuNPs. According to theoretical studies, CO oxidation is examined using Au/rutile-TiO$_2$(110) models shown in Fig.8.9 ((a) Molina *et al*. [108] (b) Liu *et al*. [83] (c) Remediakis *et al*. [85]). In these papers, O$_2$ molecules are adsorbed at perimeter interface, and CO molecules are adsorbed at Au cluster. Then, adsorbed CO molecules diffuse to perimeter interface and react with O$_2$ molecules. From our

observations and both experimental and theoretical reports, we think that CO oxidation occurs as follows (Fig.8.14). Reaction of $Vo[O_2]^-$ with CO molecule at the perimeter interface; $Vo[O_2]^- + CO \rightarrow CO_2$ (Fig.8.14).

In perimeter model, active sites seem to be perimeter interface between AuNPs and support [11]. In two layers model, active sites are not written clearly [31–34]. However, CO oxidation possibly occur at perimeter interface between two layer Au cluster with the (1 x 3) structure and support (Fig.6 of [32]). In Au cation model, they claimed that strongly bound gold on ceria is active site. Our experimental results are consistent with perimeter model.
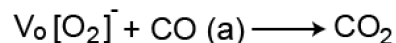
Figure 8.14: Schematic illustration of CO oxidation. Au_{edge} and CO(a) show Au atoms at edge of AuNPs and adsorbed CO molecules respectively. Captions in the schematic illustration show grounds. The color means as follows. Green: our experiments, Red: referred theoretical studies.

8.4 Reaction models in O_2 and CO/air
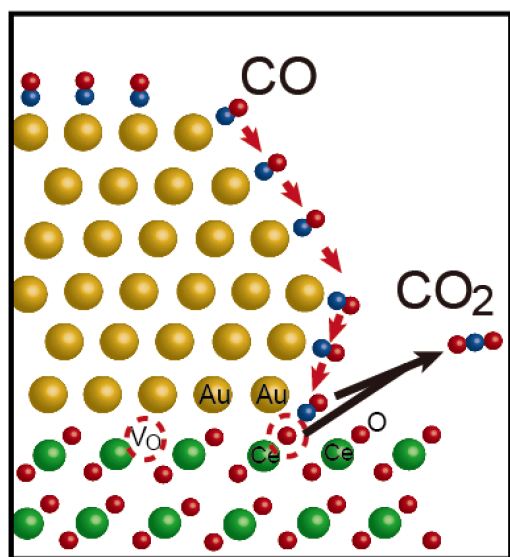
From these results, reaction models in O_2 and CO/air were considered (Fig.8.15). The reaction of Au/CeO_2 catalysts in O_2 is as follows.

1. O_2 molecules are adsorbed at the perimeter interface and dissociate.

2. O atoms cover the surface of AuNPs.

3. AuNPs become round.

The reaction of Au/CeO_2 catalysts in CO/air is as follows.

1. CO molecules are adsorbed at edges and corners of AuNPs.

2. O_2 molecules are adsorbed at the perimeter interface and dissociate.

3. Adsorbed CO molecules move to the perimeter interface through the surface of AuNPs.

4. CO molecules react with O_2 molecules (or O atoms) at the perimeter interface and become CO_2 molecules.

We recall the existing models for the CO oxidation by AuNP catalysts (without electron irradiation). There are a few possible processes by which oxygen molecules are activated on AuNPs supported on metal oxides. It was suggested that O_2 molecules are adsorbed at the perimeter interface and dissociate into O atoms with

rather small dissociation energy [83]. More recently, a probable pathway has been proposed. This pathway consists of the several primary processes. For CO molecules: (I) Adsorption of CO molecules on the surface of AuNPs. (II) Migration of CO molecules on the surface of AuNPs. (III) Capture of CO molecules at the perimeter interface. For O_2 molecules: (IV) Formation of lattice vacancies at the oxygen sites in CeO_2 supports, Vo especially at the periphery interface, in which CO molecules play a role; $CO \rightarrow CO_2 + [Vo]^-$. (V) Capture of O_2 molecules at $[Vo]^-$, i.e., $O_2 + [Vo]^- \rightarrow Vo[O_2]^-$. For oxidation of CO molecules: (VI) Reaction of $Vo[O_2]^-$ with CO molecule at the perimeter interface; $Vo[O_2]^- + CO \rightarrow CO_2$. The pathway is iterative. In the left panel of Fig. 8.15(a), the pathway is depicted concisely. ETEM observation during CO oxidation never conflicts with this model pathway. As mentioned above, we have concluded that process (I) actually occurs (Fig.6.5 and Fig.6.7). Since lighter oxygen atoms in metal oxide supports are displaced more frequently by electron irradiation, the supports are slightly reduced. Therefore, process (IV) and accordingly process (V) may be promoted by electron irradiation. Suppose that only O_2 gas exists around Au/CeO_2 catalysts during electron irradiation. (IV') Electron irradiation substitutes the role played by CO molecules in the process (IV). Vo can surely be introduced by electron irradiation without CO gas. (V') Once Vo is formed, O_2 molecules are trapped by Vo via process (V). (VII) Now, it may happen that trapped $[O_2]^-$ ions can be dissociated by the aid of electron irradiation as follows, $Vo[O_2]^- + 2 e^- \rightarrow Vo + 2 [O]^-$. Active atomic oxygen spout from the perimeter interface, cover the

114

surface of AuNPs and cause dynamic multi-faceted, or round morphology, as depicted in Fig. 8.15(b). During CO oxidation under electron irradiation, processes (IV') and (V') are expected to proceed as well as processes (IV) and (V). Processes (IV') and (V') are depicted in the left panel of Fig. 8.15(a), while processes (IV) and (V) in the right panel of Fig. 8.15(a). Though we cannot rule out other possible pathways, it is emphasized that the morphology of AuNPs directly found in ETEM observation surely corresponds to the catalytic activity of AuNPs supported on CeO_2. Especially, ETEM observations have led a conclusion that O_2 molecules are possibly dissociated at the perimeter interface and accordingly the catalytic site is the perimeter interface as well.
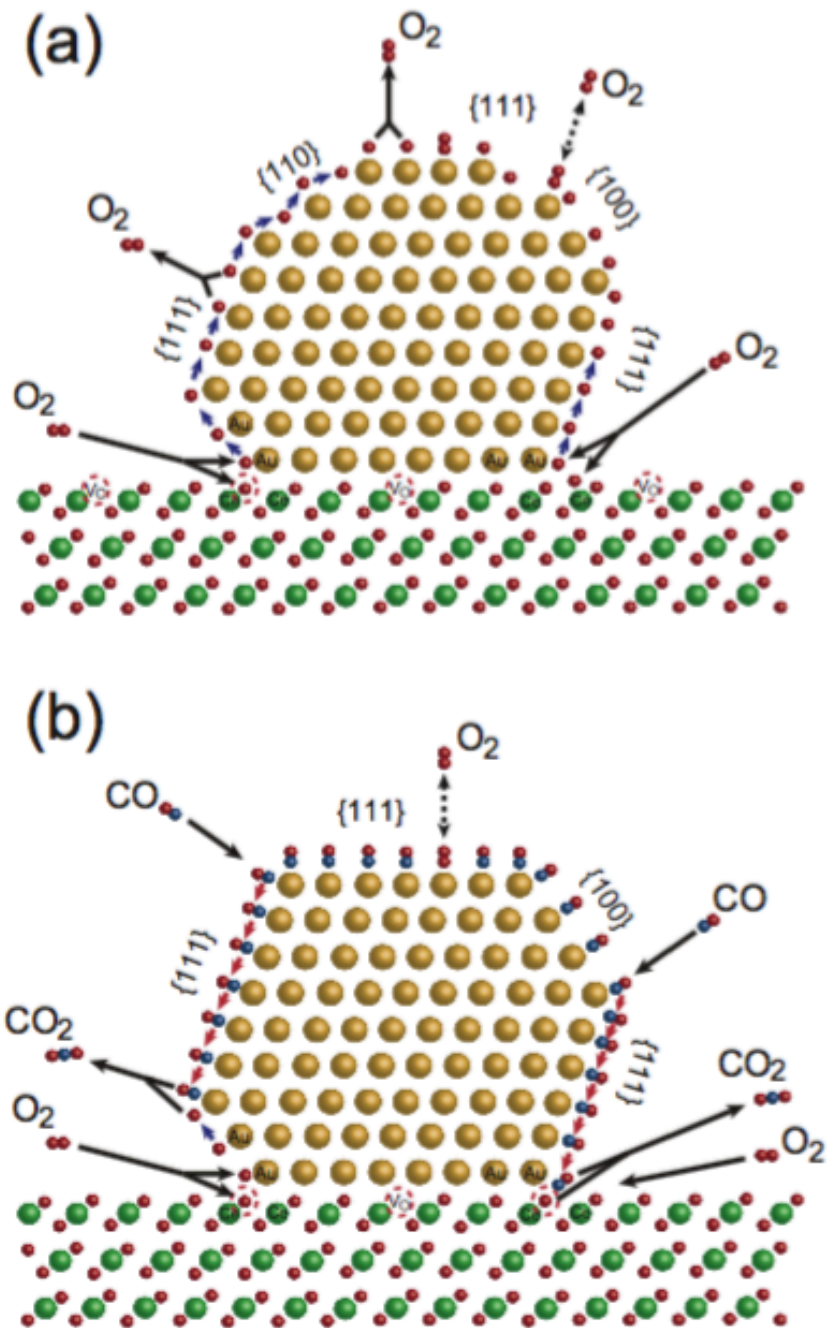
Figure 8.15: Reaction models in (a) O_2 and (b) CO/air.

8.5 Conclusions

We have performed systematic ETEM observations of AuNPs supported on metal oxides in various gas environment including the catalytic reaction condition. Our ETEM observations have uniquely shown the systematic change in the morphology of AuNPs depending on the partial pressure of CO and O_2 gases at atomic scale. Establishing the morphology diagram, we have concluded as follows.

1. CO molecules are adsorbed at edges and corners of AuNPs, stabilizing AuNPs of polyhedron in shape enclosed by the major {111} and {100} facet surfaces.

2. O_2 molecules are possibly adsorbed and dissociated at the perimeter interface. Then the O atoms diffuse on the AuNPs surface, resulting in round morphology of AuNPs.

We have also carried out ETEM observations of AuNPs on CeO_2, SiO_2, TiC supports, which is known as reducible oxide, irreducible oxide and carbide respectively, in O_2 and CO/air. Our ETEM observations have shown the tendency that morphology changes of AuNPs differ depending on support materials. We conclude as follows.

3. The ratio of AuNPs which show round morphology in O_2 and facet morphology in CO/air tends to high in highly active catalysts.

4. There is a possibility that not all AuNPs but parts of AuNPs contribute to catalytic reactions, and the ratio of AuNPs which take part in catalytic reactions affects catalytic activity.

Interfacial structure of AuNPs and supports possibly relate to the ratio. However, further insight into these aspects is left to future work. Elucidating factors which determine each AuNP active or not lead to investigate more active Au catalysts. Moreover, these findings may bring general understanding of support role, especially its role in oxygen activation and supply in CO oxidation.

Finally, we want to show future prospects. To understand the reaction mechanism of CO oxidation over Au catalysts, following questions should be solved.

1. How is oxygen supplied to CO oxidation reactions? (1) Do O_2 molecules convert to active oxygen species or peroxo-like (or superoxio-like) species, then react with CO molecules? or (2) Do O_2 molecules dissociate into O atoms and react with CO molecules?

2. How do adsorbed CO molecules and O_2 molecules and/or O atoms react each other and become CO_2?

3. What determine AuNPs active or not? Are there any optimum interface structure between AuNPs and supports?

One approach to understand these matters is theoretical study. The shape of AuNPs in O_2 and CO/air has been determined from our experiments. Reliable models can be made based on our

experimental results. We hope that theoretical studies using this model contribute to understand these matters. The other approach is in situ observation of the reaction using a Cs corrected ETEM. It has a potential to observe the reactions of molecules directly.

One useful way to study metal nanoparticle catalysts has shown in this study. We think that our observations will induce further experiments and computer simulations to elucidate the reaction mechanism of Au catalysts and other metal nanoparticle catalysts.

Chapter 9

Application of ETEM to understanding the growth mechanism of CNTs

9.1 Introduction

Carbon nanotubes (CNTs) are expected as nanomaterials for future nanodevices. Their electronic properties can be varied from metal to semiconducting depending on their atomic structure [115]. CNTs grow from nanoparticle catalysts (NPCs) such as Fe, Co and Ni by chemical vapor deposition (CVD) method. To employ CNTs for nanodevices, it is essential to produce CNTs of desired atomic structure selectively. However, no one has yet succeeded in selective growth of CNTs. For the selective growth, it is very important to understand their growth mechanism. Especially, NPCs state in the growth is discussed. It is also known that addition of some kind of metal to Fe affects yield of CNTs. Molybdenum is known for affecting yield of CNTs. Though, pure molybdenum is inactive as NPCs, adding a certain amount of molybdenum to iron increase the yield of CNTs [116, 117]. The role of Mo was unclear. To investigate growth mechanism of CNTs from NPCs and role of the Mo, we observed CNTs growth by ETEM.

9.2 Experimental procedure

Fe (99.999%) of 1nm thick was deposited on the thin SiO_2 surface layer of silicon substrates or Silicon nanowires (SiNWs) by vacuum evaporation (Fig. 9.1).   For examining Mo role, Mo (99.5%) was also deposited on the substrates.   The substrates were set in the ETEM and then heated to 600 ℃ in a vacuum.   Subsequently, a mixture of C_2H_2 : H_2 = 1 : 1 was introduced into the ETEM.   The pressure of the gas and the temperature of the substrates were 0.1 mbar and 600 ℃ in the CVD conditions.
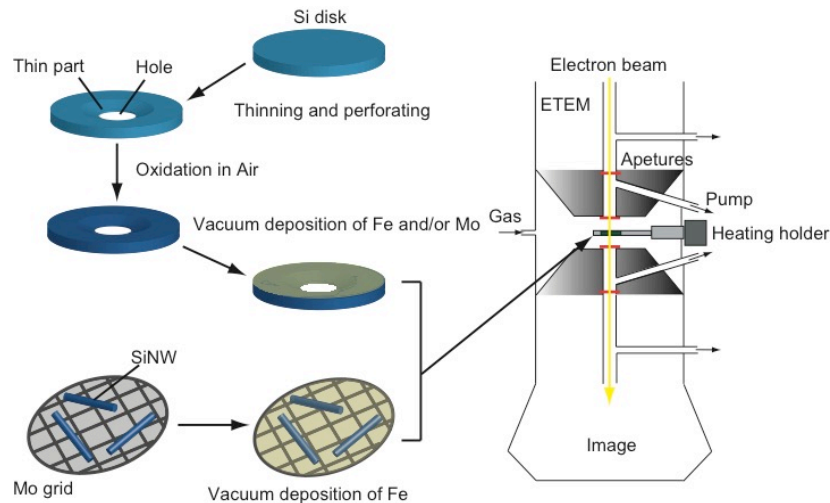
Figure 9.1: Specimen preparation for the in situ observation of the CNT growth.

9.3 Results and discussion

9.3.1 ETEM observation of carbon nanotube growth from iron catalyzed nanoparticles

First, we show that catalytically active NPCs in CNTs growth are structurally fluctuating Fe carbide. Fig. 9.2 shows ETEM images of a MWNT growth viewed nearly normal to the growth direction. The position of the NPC did not change during the growth. Therefore, crystal orientation of the NPC changes without physical rotation in the growth process. All lattice images of the images correspond to iron carbide (Fe_3C) structure. From the ETEM observations, it can be concluded that NPCs are fluctuating crystalline cementite nanoparticles. Carbon atoms are seemed to migrate via bulk diffusion in NPCs.
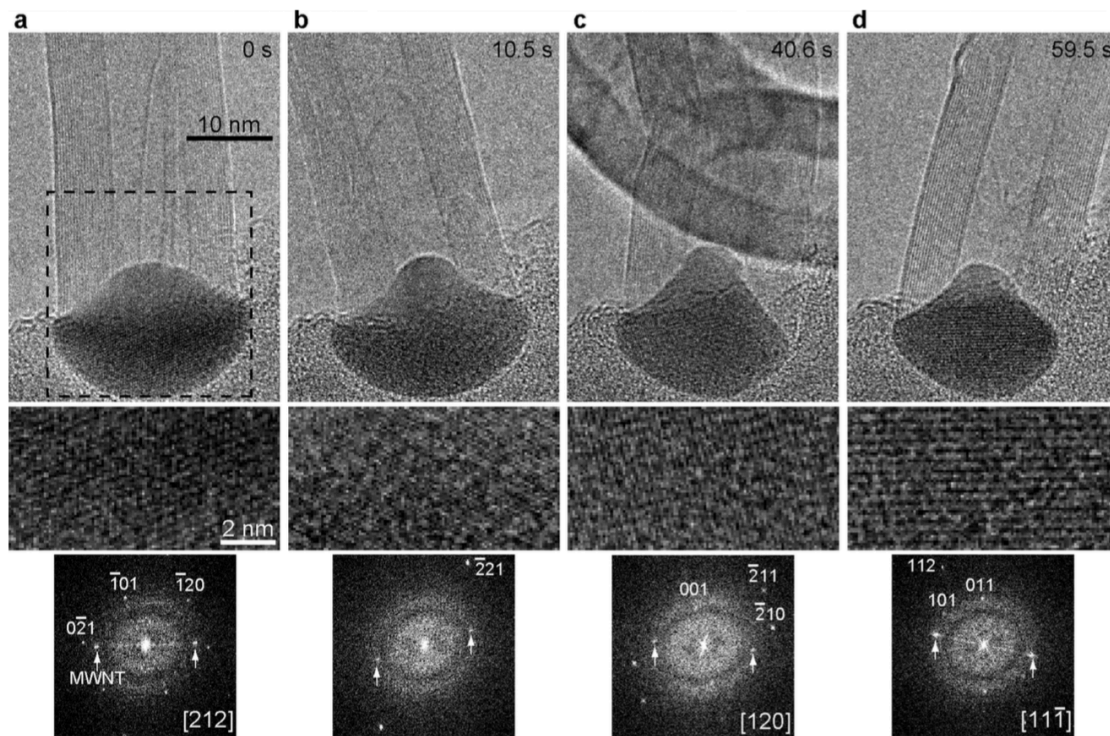
Figure 9.2: Successive ETEM images of a MWNT growth from an iron carbide nanoparticle [28].

9.3.2 ETEM analysis of the role of molybdenum addition to carbon nanotube growth

To examine the synergetic role played by Mo in iron catalyzed growth of CNTs, ETEM observations of Fe-Mo codeposit substrates in CVD growth condition were carried out. In situ ETEM images of the growth of a MWNT from a NPC is shown in Fig. 9.3. Lattice images of the NPC correspond to $(Fe, Mo)_{23}C_6$ type structure and the crystalline axis change with regard to the viewing direction. Electron diffraction analyses of Fe-0, 28.7 and 37.6 at% Mo codeposit substrates before and after CVD process were also carried out. From the electron diffraction analyses, without Mo addition, iron silicate which is known as inactive for the growth of CNTs appears in CVD process. On the other hand, with Mo addition, iron silicate nucleation is suppressed.

From the results, we conclude that deposition of proper amount of Mo on substrates promotes nucleation of Fe-Mo carbide NPCs of $(Fe, Mo)_{23}C_6$ structures as well as Fe_3C. It is also suggested that the nucleation of inactive iron silicate was suppressed by Mo addition.
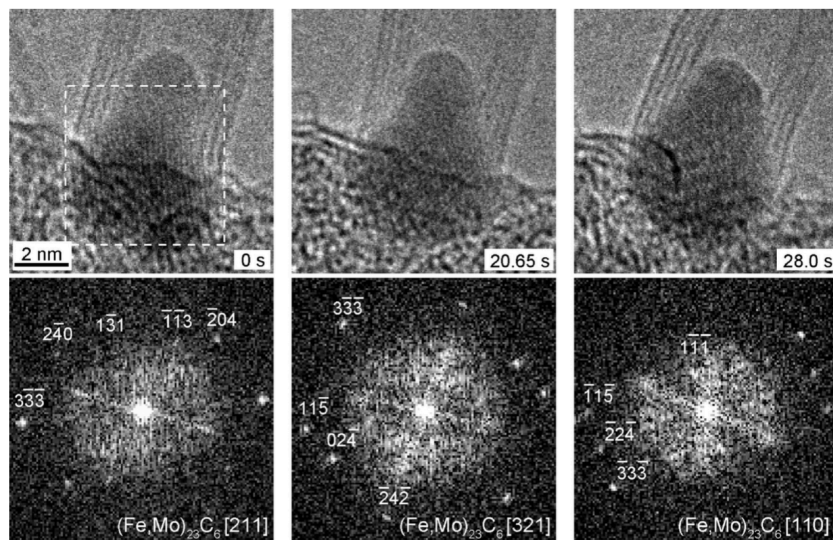
Figure 9.3: Growth process of a MWNT from a $(Fe, Mo)_{23}C_6$ nanoparticle [118].

9.4 Summary

ETEM was applied to examine CNT growth mechanism. ETEM observations clearly showed that (1) NPCs are fluctuating crystalline nanoparticles, (2) the NPCs are cementite Fe_3C and (3) carbon atoms migrate through NPC bulk and (4) nucleation of inactive iron silicate was suppressed by Mo addition, resulting in increase in CNTs yield. As described above, ETEM is a useful method to examine solid-gas reaction at atomic scale in real time. It is expected that ETEM will be applied to other solid-gas reactions such as catalytic reactions and nanomaterial fabrications.

Chapter 10

General conclusion

To examine peculiar catalytic activities of Au catalysts, correlations among morphology changes of AuNPs in gases, support materials and catalytic activities have been studied systematically by means of ETEM.

Metal catalysts have been reviewed in chapter 2. Brief history of ETEM and the ETEM study of metal nanoparticle catalysts have been reviewed in chapter 3.

In chapter 4 and 5, precautions for ETEM observations have been described. In chapter 4, irradiation damage on AuNPs and CeO_2 support and desorptions of CO molecules from the surface of AuNPs by electron irradiation are investigated. From these results, we conclude that proper flux of electron beam for observations is smaller than 5 A/ cm^2. In chapter 5, sample contaminations from CO-rich gases are examined. It is known that CO gas of high pressure reacts with the inside wall of cylinders and gas supply lines, forming CPs. These CPs may be mixed within the gas being delivered to the ETEM and decomposed by electron irradiation in the ETEM, forming contamination on samples. After examining the contamination process by ETEM, it is demonstrated that gas purification is crucially important. Our investigation clearly shows that reducing the unintentional effects of electron irradiation and

corrosive gases is very important to observe intrinsic phenomena of catalytic activities by ETEM.

In chapter 6, systematic ETEM observations of AuNPs supported on CeO_2 in various partial pressures of CO and O_2 are carried out for the first time. Our ETEM observations have shown the systematic change in the morphology of AuNPs depending on the partial pressure of CO and O_2 gases. Comparing Au/CeO_2 catalysts with Au/TiC catalysts in O_2 and CO/air, we have found that AuNPs in the active Au/CeO_2 catalyst tend to show round morphology in O_2. Establishing the morphology diagram, we have concluded that 1) CO molecules are adsorbed on the surface of AuNPs, stabilizing AuNPs of polyhedral shape enclosed by the major {111} and {100} facet surfaces, 2) O_2 molecules possibly dissociate into O atoms, resulting in round morphology of AuNPs.

In chapter 7, to examine whether AuNPs behavior in gases differ depending on support materials and catalytic activity, ETEM observations of AuNPs on CeO_2, SiO_2, TiC supports in O_2 and CO/air were carried out. From the ETEM observations, we found that morphology changes of AuNPs differ depending on support materials. The ratio of AuNPs which show round morphology in O_2 and facet morphology in CO/air tends to high in highly active catalysts. Round morphology in O_2 possibly correlates to O atoms adsorptions on AuNP surface. It is considerable from these results that not all AuNPs but parts of AuNPs contribute to catalytic reactions, and the ratio of AuNPs which take part in catalytic reactions affects catalytic activity.

In chapter 8, CO oxidation reaction mechanism of Au catalysts is discussed in terms of adsorptions of CO and O_2 molecules, dissociations of O_2 molecules and CO oxidation on the basis of our experimental results and previous reports. Our study supports the perimeter model.

Application of ETEM to the growth mechanism of CNT is shown in chapter 9. ETEM observations clearly showed that NPCs are fluctuating crystalline Fe_3C nanoparticles and carbon atoms migrate through NPC bulk. ETEM is also useful to observe nanomaterial fabrications.

Our observations will induce further experiments and computer simulations to elucidate the reaction mechanism of Au catalysts. Our ETEM observations clearly showed the structure of active Au/CeO_2 catalysts in O_2 and CO/air. It is expected that more accurate simulations using model structure based on our observations will be held. In addition, our observations suggest a renewed focus on the importance of examining dissociation of O_2 molecules in CO oxidation reaction. We also present the possibility that not all AuNPs but parts of AuNPs contribute to catalytic reactions and the ratio of AuNPs which take part in catalytic reactions affects catalytic activity. Oxygen vacancies in a crystalline support, the charge transfer between AuNPs and supports, and the structural coherency between AuNPs and supports are considered to affect activation of oxygen even below room temperature and catalytic activity. From these perspectives, controlling interfacial structure of AuNPs and supports in sample preparations possibly increase the active AuNPs ratio on various

supports.   Moreover, these findings may bring general understanding of support role, especially its role in oxygen activation and supply in CO oxidation.   Further more, we have shown an effective approach of the ETEM to study the reaction mechanism of metal nanoparticle catalysts.   We are convinced that this work stimulates the study to reveal various solid-gas reactions at atomic scale.

Appendix A

Preparation methods of Au catalysts

Catalytic activity of Au catalysts depends on preparation methods. Contact between AuNPs and support and the size distribution of AuNPs vary depends on preparation methods [11]. Here, we want to explain about three major methods i.e. deposition precipitation (DP) method, solid grinding (SG) method and impregnation (IP) method.

A.1 DP method

Fig. A.1(a) shows a detailed procedure for DP method. The pH of aqueous $HAuCl_4$ solution is adjusted at a fixed point in the range from 6 to 10. Careful control of the concentration, pH (6-10), and temperatures (50-90 ℃) of aqueous $HAuCl_4$ solution can lead to the selective deposition of $Au(OH)_3$ only on the surface of support metal oxides. Then, the precursor is calcined in air and become Au/support catalyst.

A.2 SG method

Fig. A.1(b) shows a detailed procedure for SG method. Dimethyl gold acetylacetonate is used as precursors in SG method. Under ordinary pressure at room temperature, the precursor and a support

are mixed by mechanical friction. As the saturated vapor pressure of precursors is high, AuNPs disperse on the surface of the support.

A.3 IP method

Fig. A.1(c) shows a detailed procedure for IP method. A metal oxide support is immersed in an aqueous solution of $HAuCl_4$ and then water is evaporated to disperse Au^{3+} and Cl^- ions over the support surfaces. The dried precursor is calcined in air, usually at temperatures above 200 ℃. Then, the precursor is washed by water to get rid of Cl. After drying, AuNPs disperse on the surface of the support.

Features of AuNPs deposited on support by the methods are summarized in Table A.1 [74]. In Au catalysts, strong contact between AuNPs and support and small size distribution of AuNPs are required. From this point of view, DP method is a most remarkable method.

Table A.1: Features of AuNPs deposited on support by DP method, SG method and IP method. Representative example of contact between AuNPs and support and size distribution of AuNPs of Au/CeO$_2$ catalysts are shown in each method [74].

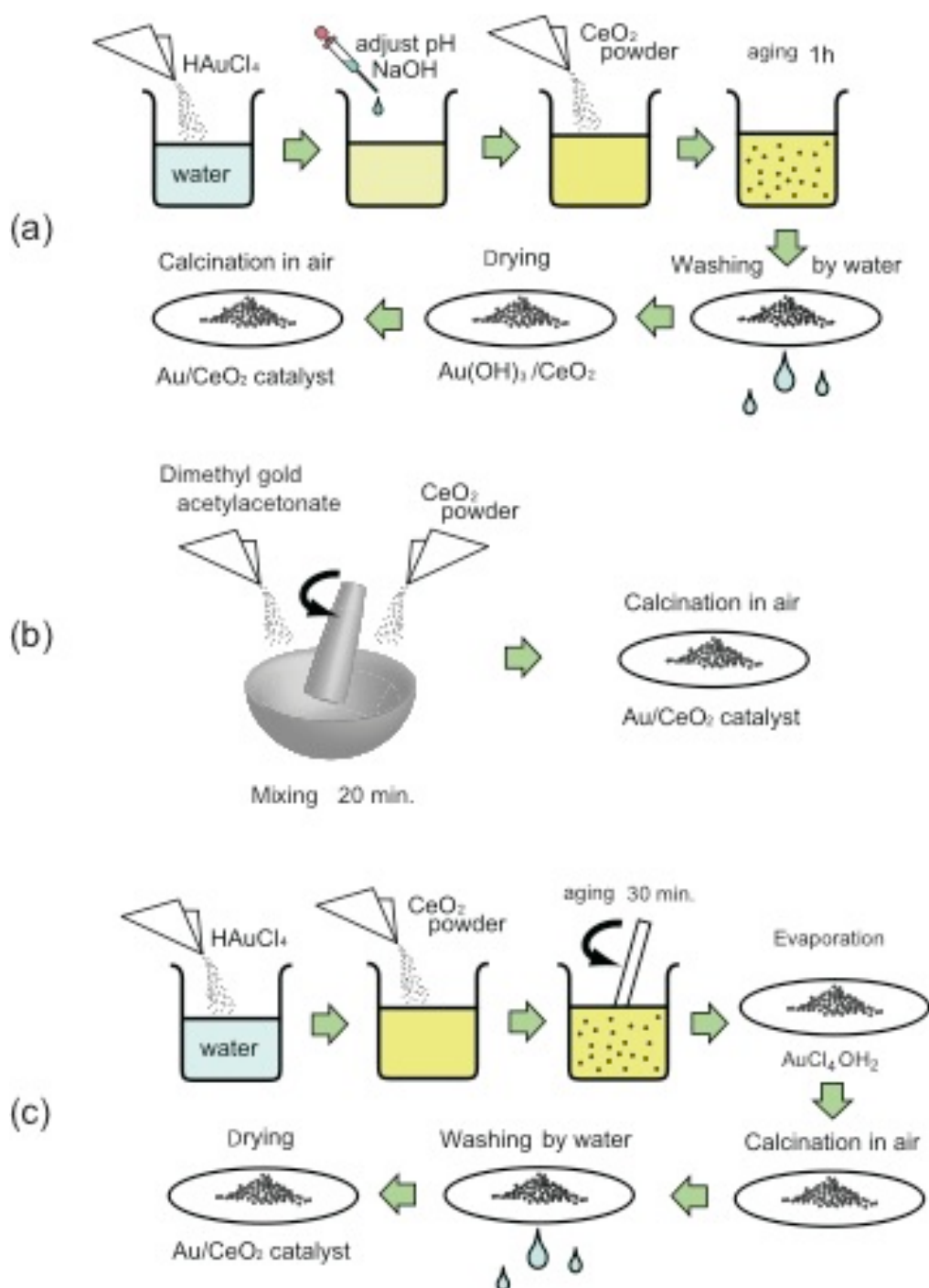|	DP method	SG method	IP method
Size of GNPs	4.1 nm	10.6 nm	53 nm
Contact to the support	Strong	Strong	Weak

Figure A.1: Procedure of (a) DP method, (b) SG method and (c) IP method.

Appendix B

Supporting information of examinations of AuNPs on CeO$_2$, SiO$_2$ and TiC

B.1 Sample preparations

Au/CeO$_2$-1 was prepared by the deposition precipitation (DP) method and characterized by Shimada *et al*. [74] and observed using environmental transmission electron microscopy (ETEM) by our group [92]. Au/CeO$_2$-2 and Au/SiO$_2$ were commercially available a Au/CeO$_2$ catalyst (Haruta Gold Inc., RRCe-2)) prepared by the DP method and a Au/SiO$_2$ catalyst (Haruta Gold Inc., RRCe-2)) prepared by the deposition reduction (DR) method respectively. A Au/TiC catalyst was prepared by the solid grinding (SG) method [74]. Mixture of $(CH_3)_2Au(C_5H_7O_2)$ (Gas-Phase Growth LTD.) of 0.01656 g and TiC powders (The Nilaco corporation, TI-457202) of 1.00001 g were ground in a mortar for 20 minutes. Generally, precursors of Au catalysts are calcined in air at 300 ℃ for 4 hours. In consideration of TiC support oxidation, the calcination was not carried out in the Au/TiC catalyst.

To confirm TiC support of the Au/TiC catalyst was not oxidized, we carried out an X-ray diffraction (XRD) measurement and structural analyses by means of high resolution transmission

electron microscopy (HRTEM) and EELS measurements on O K-edge (Fig. B.1). In the XRD measurement (Fig. B.1 (a)), diffraction peaks derived from Au and TiC were confirmed. On the other hand, peaks derived from anatase or rutile TiO_2 were not confirmed. The fast Fourier transformation (FFT) image of TiC support in the HRTEM image (Fig. B.1 (b)) was consistent with the TiC (NaCl structure) viewed along a <011> direction. Moreover, O K-edge peak at 532 eV was not confirmed in the EELS spectrum (Fig. B.1 (d)). From these results, we concluded that TiC support of the Au/TiC catalyst is not oxidized within the detection limit of these methods.
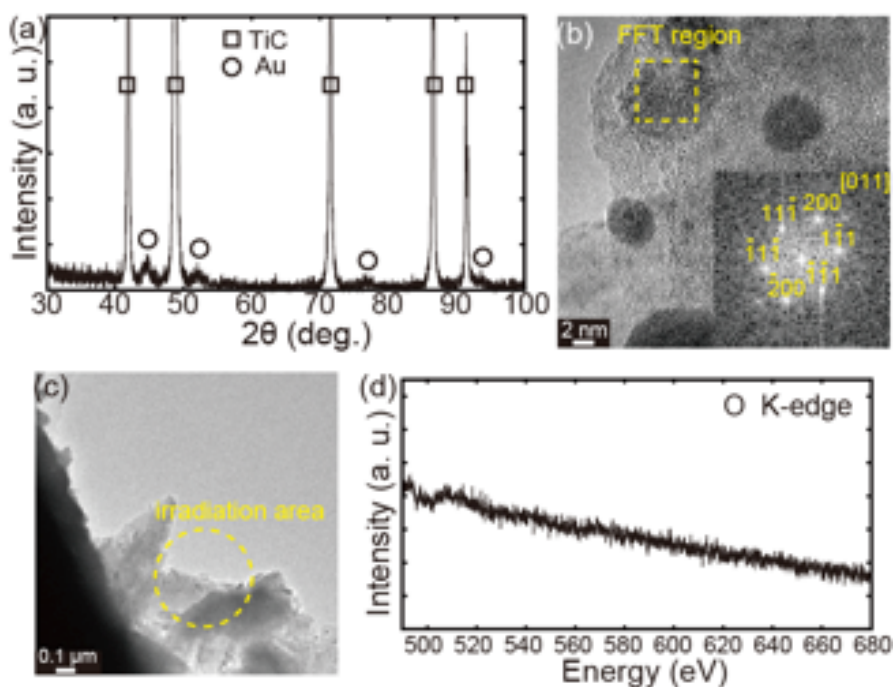

Figure B.1 (a) a XRD pattern, (b) a HRTEM image with a fast Fourier transformation (FFT) image of the region enclosed by a square, (c) a region of an EELS measurement, (d) an EELS spectrum at O K-edge.

B.2 CO to CO_2 conversion rates

Activities of the catalysts were measured using a fixed-bed flow reactor. A catalyst sample of 150 mg was used for a pretreatment and a catalytic measurement. Pretreatment gas was 20 vol% O_2 and 80 vol% He mixture and reactant gas was 1vol % CO, 20 vol% O_2 and 79 vol% He mixtuer. In the pretreatment, the gas was fed at the rate of 50 ml/min at 250 ºC for 1h. In consideration of TiC support oxidation, the pretreatment was not carried out in the Au/TiC catalyst. The catalytic activities were measured by passing the reactant gas at the rate of 50 ml/min, which corresponds to space velocity 20000 ml/h・$g_{cat.}$. Usually, ETEM observations are carried out at room temperature. As room temperature differs depending on seasons, temperature control in measurements of catalytic activities is difficult. Therefore, we measured CO to CO_2 conversion rates of Au/CeO_2-2, Au/SiO_2 and Au/TiC at 30, 40 50, 60 and 90 ºC (Fig. B.2). A catalytic activity of Au/CeO_2-1 is shown in Ref. 74. It was confirmed that a CO to CO_2 conversion rate of Au/CeO_2-1 reaches 100 % at 30 ºC [74]. The CO to CO_2 conversion rate of Au/CeO_2-2 reached 5.2 % at 30 ºC, then it increased sharply with the increase in temperature and reached 41.3 % at 60 ºC and finally reached 94.4 % at 90 ºC. The CO to CO_2 conversion rate of Au/SiO_2 gradually increased with the increase in temperature. It reached 1.3 %, 8.7 % and 10.3% at 30, 60 and 90 ºC respectively. The CO to CO_2 conversion rate of Au/TiC is nearly constant with temperature. It showed 1.1 %, 0.2 % and 0.3% at 30, 60 and 90 ºC respectively. The rate of Au/CeO_2-1 is the highest of the four. That of Au/CeO_2-2 is higher than that of Au/SiO_2 and Au/TiC. That of Au/TiC is the lowest of

the four.
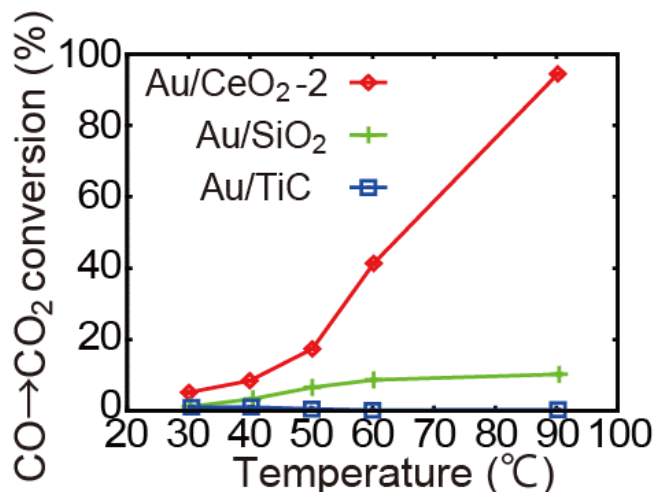
Figure B.2 CO to CO_2 conversion rates of Au/CeO$_2$-2, Au/SiO$_2$ and Au/TiC.

B.3 ETEM observations

B.3.1 ETEM images of AuNPs in each sample

We chose three AnNPs from observed AuNPs which showed typical morphology changes in gases in each sample (Fig. B.3). Two AuNPs which showed round morphology in O_2 and facet morphology in CO/air and one AuNP which showed facet morphology in both O_2 and CO/air of Au/CeO$_2$-1 and Au/CeO$_2$-2 are shown in Fig. B.3 (a) and (b). Two AuNPs which showed facet morphology in both O_2 and CO/air and one AuNP which showed round morphology in O_2 and facet morphology in CO/air of Au/SiO$_2$ and Au/TiC are shown in Fig. B.3 (c) and (d).

Figure B.3 ETEM images of (a) Au/CeO$_2$-1, (b) Au/CeO$_2$-2, (c) Au/SiO$_2$, and (d) Au/TiC in vacuum, O$_2$ at 1 mbar and CO/air at 1 mbar. Relative morphology index M is also shown in the ETEM images in O$_2$ and CO/air.
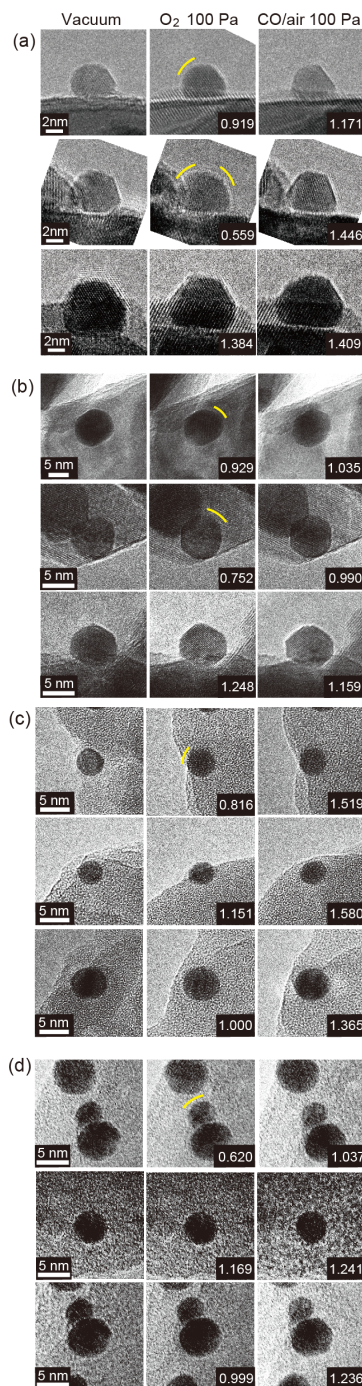
138

B. 3.2 Confirmation of unoxidized stat of TiC support of the Au/TiC catalyst before and after ETEM observations

To confirm TiC support of Au/TiC was not oxidized in ETEM observations interacting with O_2 and CO/air under electron irradiation, we carried out EELS measurements before and after ETEM observations (Fig. B.4). O K-edge at 532 eV was not confirmed before and after ETEM observations. It can be concluded that TiC support is not oxidized in ETEM observations within detection limit of EELS.
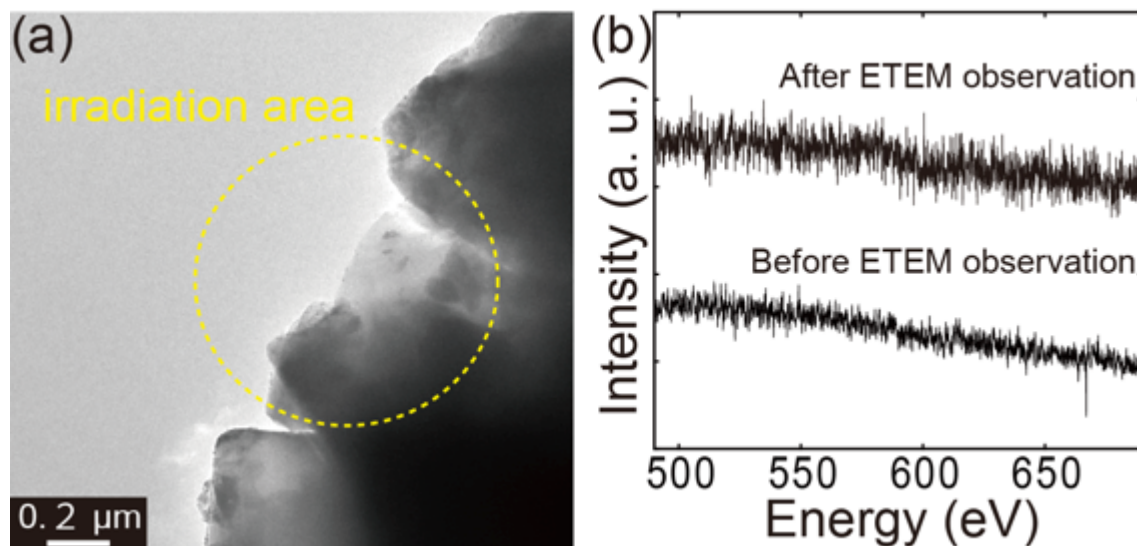

Figure B.4 (a) Electron beam irradiation area in ETEM observations and EELS measurements. (b) EELS spectra of O K-edge before and after ETEM observations. O K-edge peak at 532 eV was not confirmed before and after ETEM observations.

References

[1] H. S. Gandhi, G. W. Graham and R. W. McCabe: J. Catal. **216** (2003) 433.

[2] M. Shelef and R. W. McCabe: Catal. Today **62** (2000) 35.

[3] M. S. Wilson and S. Gottesfeld: J. Electrochem. Soc. **139** (1992) L28.

[4] D. R. Rolison, P. L. Hagans, K. E. Swider and J. W. Long: Langmuir **15** (1999) 774.

[5] M. Rønning, F. Huber, H. Meland, H. Venvik, D. Chen and A. Holmen: Catal. Today **100** (2005) 249.

[6] S. Iijima: Nature **354** (1991) 56.

[7] S. Iijima and T. Ichihashi: Nature **363** (1993) 603.

[8] P. Buffat and J.-P. Borel: Phys. Rev. A **13** (1976) 2287.

[9] Y. Yamamoto, T. Miura, M. Suzuki, N. Kawamura, H. Miyagawa, T. Nakamura, K. Kobayashi, T. Teranishi and H. Hori: Phys. Rev. Lett. **93** (2004) 8410.

[10] S. Link and M. A. El-Sayed: J. Phys. Chem. B **103** (1999) 8410.

[11] M. Haruta: CATTECH **6** (2002) 102.

[12] D. Takagi, Y. Homma, H. Hibino, S. Suzuki and Y. Kobayashi: Nano Lett. **6** (2005) 2642.

[13] J. Kikkawa, Y. Ohno and S. Takeda: Appl. Phys. Lett. **86** (2005) 123109.

[14] M. Haruta, N. Yamada, T. Kobayashi and S. Iijima: J. Catal. **115** (1989) 301.

[15] S. D. Gardner and G. B. Hoflund: Langmuir **7** (1991) 2135.

[16] Q. Fu and M. Flytzani-Stephanopoulos: Catal. Lett. **77** (2001) 87.

[17] W. Liu and M. Flytzani-Stephanopoulos: J. Catal. **153** (1995) 304.

[18] T. Hayashi, K. Tanaka and M. Haruta: J. Catal. **178** (1998) 566.

[19] S. Nettesheim, A. von Oertzen, H. H. Rotermund and G. Ertl: J. Phys. Chem. **98** (1993) 9977.

[20] J. Wintterlin, S. Völkening, T. V. W. Janssens, T. Zambelli and G. Ertl: Science **278** (1997) 1931.

[21] E. D. Boyes and P. L. Gai: Ultramicroscopy **67** (1997) 219.

[22] T. W. Hansen, J. B. Wanger, P. L. Hansen, S. Dahl, H. Topsøe and C. J. H. Jacobsen: Science 294 (2001) 1508.

[23] S. Helveg, C. López-Cartes, J. Sehested, P. L. Hansen, B. S. Clausen, J. R. Rostrup-Nielsen, F. Ablid-Pedersen and J. K. Nørskov: Nature **427** (2004) 426.

[24] R. Sharma and Z. Iqbal: Appl. Phys. Lett. **84** (2004) 990.

[25] P. L. Gai and E. D. B. andJ. C. Bart: Phil. Mag. A **45** (1982) 531.

[26] P. L. Gai, B. C. Smith and G. Owen: Nature **348** (1990) 430.

[27] P. L. Gai, K. Kourtakisa and E. D. Boyes: Catal. Lett. **102** (2005) 1.

[28] H. Yoshida, S. Takeda, T. Uchiyama, H. Kohno and Y. Homma: Nano. Lett. **8** (2008) 2082.

[29] P. L. Hansen, J. B. Wanger, S. Helveg, J. R. Rostrup-Nielsen, B. S. Clausen and H. Topsøe: Science **295** (2002) 2053.

[30] S. Giorgio, S. S. Joao, S. Nitsche, D. Chaudanson, G. Sitja and C. R. Henry: Ultramicroscopy **106** (2006) 503.

[31] M. S. Chen and D. W. Goodman: Science **306** (2004) 252.

[32] M. S. Chen and D. W. Goodman: Acc. Chem. Res. **39** (2006) 739.

[33] H. S. Q. Fu and M.Flytzani-Stephanopoulos: Science **301** (2003) 935.

[34] W. Deng, J. D. Jesus, H. Saltsburg and M.Flytzani-Stephanopoulos: Appl. Catal. A Gen. **291** (2005) 126.

[35] A. Taniguchi, T. Akita, K. Yasuda and Y. Miyazaki: J. Power Sources **130** (2004) 42.

[36] Y. Hayamizu, T. Yamada, K. Mizuno, R. C. Davis, D. N. Futaba, M. Yumura and K. Hata: Nature Nanotech. **3** (2008) 289.

[37] G. Ertl: Angew. Chem. Int. Ed. **47** (2008) 3524.

[38] G. Ertl: J. Mol. Catal. A **5** (2002) 182.

[39] L. M. Marks: Rep. Prog. Phys. **57** (1994) 603.

[40] K. Koga, T. Ikeshoji and K. Sugawara: Phys. Rev. Lett. **92** (2000) 115507.

[41] S. Iijima and T. Ichihashi: Phys. Rev. Lett. **56** (1986) 616.

[42] G. C. Bond and P. A. Sermon: Gold Bull. **6** (1973) 102.

[43] G. C. Bond and P. A. Sermon: J. C. S. Chem. Comm. (1973) 444.

[44] D. Y. Cha and G. Parravano: J. Catal. **18** (1970) 200.

[45] S. Galvano and G. Parravano: J. Catal **55** (1978) 178.

[46] T. Hayashi, K. Tanaka and M. Haruta: J. Catal. **178** (1998) 566.

[47] S. Biella, L. Prati and M. Rossi: J. Catal. **206** (2002) 242.

[48] M. Okumura, Y. Kitagawa, K. Yamaguchi, T. Akita, S. Tsubota and M. Haruta: Chem. Lett. **32** (2003) 822.

[49] M. Valden, X. Lai and D. W. Goodman: Science **281** (1998) 1647.

[50] H. Yoshida, K. Matsuura, Y. Kuwauchi, H. Kohno, S. Shimada, M. Haruta and S. Takeda: Appl. Phys. Express **4** (2011) 065001.

[51] S. Giorgio, M. Cabié and C. R. Henry: Gold Bull. **41/2** (2008) 167.

[52] Y. Kuwauchi, H. Yoshida, T. Akita, M. Haruta and S. Takeda: Angew. Chem. Int. Ed. **51** (2012) 7729.

[53] S. Takeda, Y. Kuwauchi and H. Yoshida, Ultramicroscopy **151** (2015) 178.

[54] H. Yoshida, Y. Kuwauchi, J. R. Jinschek, K. Sun, S. Tanaka, M. Kohyama, S. Shimada, M. Haruta and Seiji Takeda: Science **335** (2012) 317.

[55] S Y. Kuwauchi, S. Takeda, H. Yoshida, K. Sun, M. Haruta and H. Kohno: Nano Lett. **13** (2013) 3073.

[56] H. Yoshida, H. Omote and S. Takeda: Nanoscale **6** (2014) 13113.

[57] R. F. Egerton, *Electron-Loss Spectroscopy in the Electron Microscope, 2nd ed.*, Plenum Pub Corp, New York, 1996.

[58] D. A. Muller and C. B. Carter, *Transmission Electron Microscopy;* A Text Book for Materials Science Springer, New York, 2009.

[59] T. Akita, M. Okumura, K. Tanaka, M. Kohyama and M. Haruta: Catal. Today **117** (2006) 62.

[60] L. Garviea and P. Buseck: J. Phys. Chem. Solids **50** (1999) 1943.

[61] T. Manoubi, C. Colliex and P. Rez: J. Electron. Spectrosc. Relat. Phenom. **50** (1990) 1.

[62] E. Kadossov, J. Justin, D. Rosenmann, L. E. Ocola, S. Cabrini and U. Burghaus: Chem. Phys. Lett. **483** (2009) 250.

[63] A. Szabo, M. Kiskinova and J. T. Y. Jr.: J. Chem. Phys. **90 (8)** (1989) 4604.

[64] W. Lotz: Zeitschrift fur Physik **216** (1968) 241.

[65] S. Derrouiche, P. Gravejat and D. Bianchi: J. Am. Chem. Soc. **126** (2004) 13010.

[66] W. A. M. Jr. and H. Feshbach: Phys. Rev. **74** (1948) 1759.

[67] F. Banhart: Rep. Prog. Phys. **62** (1999) 1181.

[68] P. C. K. Vesborg, I. Chorkendorff, I. Knudsen, O. Balmes, J. Nerlov, A. M. Molenbroek, B. S. Clause and S. Helveg: J. Catal. **262** (2009) 65.

[69] H. Inouye and J. H. Devan : J. Mater. Energy Syst. **1** (1979) 52.

[70] M. Mihaylov, K. Hadjiivanov and H. Knözinger: Catal. Lett. **76** (2001) 59.

[71] R. Sharma, R. Moore, P. Rez and M. M. J. Treacy: Nano Lett. **7** (2009) 689.

[72] M. Shimojo, W. Zhang, M. Takeguchi, M. Tanaka, K. Mitsuishi and K. Furuya: J. Appl. Phys. **44** (2005) 5651.

[73] T. Fujit, P. Guan, K. McKenna, X. Lang, A. Hirata, L. Zhang, T. Tokunaga, S. Arai, Y. Yamamoto, N. Tanaka, Y. Ishikawa, N. Asao, Y. Yamamoto, J. Erlebacher and M. Chen: Nature Mater. **11** (2012) 775.

[74] T. Fujita, T. Tokunaga, L. Zhang, D. Li, L. Chen, S. Arai, Y. Yamamoto, A. Hirata, N. Tanaka, Y. Ding and M. Chen: Nano Lett. **14** (2014) 1172.

[75] S. Shimada, T. Takai, S. Takeda and M. Haruta: Stud. Surf. Sci. Catal. **175** (2010) 843.

[76] T. Akita, M. Okumura, K. Tanaka, M. Kohyama and M. Haruta: J. Mater. Sci. **40** (2005) 3101.

[77] H. Yoshida and S. Takeda: Phys. Rev. B **72** (2005) 195428.

[78] M. I. Buckett, J. S. D. E., Luzzi, J. P. Zhang, B. W. Wessels and L. D. Marks: Ultramicroscopy **29** (1989) 217.

[79] L. K. Ono, D. Sudfeld and B. R. Cuenya: Surf. Sci. **600** (2006) 5041.

[80] M. Mavrikakis, P. Stoltze and J. K. Norskøv: Catal. Lett. **64** (2000) 101.

[81] Y. Xu and M. Mavrikakis: J. Phys. Chem. B **107** (2003) 9298.

[82] H. Shi and C. Stampfl: Phys. Rev. B **77** (2008) 094127.

[83] Z. Liu, X. Gong, J. Kohanoff, C. Sanchez and P. Hu: Phys. Rev. Lett. **91** (2003) 266102.

[84] L. M. Molina and B. Hammer: Appl. Catal. A: General **291** (2005) 21.

[85] I. N. Remediakis, N. Lopez and J. K. Nørskov: Angew. Chem. Int. Ed. **44** (2005) 1824.

[86] L. Molina and B. Hammer: Phys. Rev. B **69** (2004) 155424.

[87] M. M. Schubert, S. Hackenberg, A. C. van Veen, M. Muhler, V. Plzah and R. J. Behm: J. Catal. **197** (2001) 113.

[88] M. Haruta: Catal. Today **36** (1997) 153.

[89] I. Remediakis, N. Lopez and J. Nørskov: Appl. Catal. A: General **291** (2005) 13.

[90] K. Sun, M. Kohyama, S. Tanaka and S. Takeda: ChemCatChem **5** (2013) 2217.

[91] T. Uchiyama, H. Yoshida, Y. Kuwauchi, S. Ichikawa, S. Shimada, M. Haruta and S. Takeda: Angew. Chem. Int. Ed. **123** (2011) 10339.

[92] M. Kotobuki, R. Leppelt, D. A. Hansgen, D. Widmann, R. J. Behm: J. Catal. **264** (2009) 67.

[93] D. Widmann and R. J. Behm: Angew. Chem. Int. Ed. **50** (2011) 10241.

[94] N. Lopez and J. K. Nørskov: J. Am. Chem. Soc. **124** (2002) 11262.

[95] A. Sanchez, S. Abbet, U. Heiz , W. D. Schneider , H. Häkkinen , R. N. Barnett and U. Landman: J. Phys. Chem. A **103** (1999) 9573.

[96] D. Stolcic, M. Fischer, G. Ganteför, Y. D. Kim, Q. Sun, and P. Jena: J. Am. Chem. Soc., **125** (2003) 2848.

[97] Y. D. Kim , M. Fischer and G. Ganteför: Chem. Phys. Lett. **377** (2003)170.

[98] B. Yoon, H. Hakkinen, U. Landman, A. S. Worz, J. M. Antonietti, S. Abbet, K. Judai and U. Heiz: Science **307** (2005) 403.

[99] K. Okazaki, Y. Morikawa, S. Tanaka, K. Tanaka and M. Kohyama: Phys. Rev. B **69** (2004) 235404.

[100] E. Wahlsröm, N. Lopez, R. Schaub, P. Thostrup, A. Ronnau, C. Afirch, E. Lægsgaard, J. K. Nørskov and F. Besenbacher: Phys. Rev. Lett. **90** (2003) 026101.

[101] A. Vittadini and A. Selloni: J. Chem. Phys. **117** (2002) 353.
75 T. Akita, M. Okumura, K. Tanaka, M. Kohyama, M. Haruta: J. Mater. Sci. **40** (2005) 3101.

[102] T. Akita, K. Tanaka, S. Tsubota and M. Haruta: J. Electron Microscopy **49(5)** (2000) 657.

[103] T. Akita, M. Kohyama and M. Haruta: Acc. Chem. Res. **46 (8)** (2013) 1773.

[104] S. Ichikawa: Microscopy **45** (2010) 147.

[105] F. Boccuzi, A. Chiorino, M. Manzpli, P. Lu, T. Akita, S. Ichikawa and M. Haruta: J. Catal. **202** (1997) 256.

[106] M. Olea, M. Kunitake, T. Shido and Y. Iwasaki: Phys. Chem. Chem. Phys. **3** (2001) 627.

[107] N. Lopez, T. V. W. Janssens, B. S. Clausen, Y. Xu, M. Mavrikakis, T. Bligaard and J. K. Nørskov: J. Catal. **223** (2004) 232.

[108] L. M. Molina, M. D. Rasmussen and B. Hammer: J. Chem. Phys. **120** (2004) 7673.

[109] H. Liu, A. I. Kozlov, A. P. Kozlov, T. Shido, K. Asakura and Y. Iwasaki: J. Catal. **185** (1999) 252.

[110] M. Okumura, J. M. Coronado, J. Soria, M. Haruta and J. C. Conesa: J. Catal. **203** (2001) 168.

[111] L. M. Molina and B. Hammer: Phys. Rev. Lett. **90** (2003) 206102.

[112] Y. Xu and M. Mavrikakis: J. Phys. Chem. B **107** (2003) 9298.

[113] G. Mills, M. S. Gordon and H. Metiu: J. Chem. Phys. **118** (2003) 4198.

[114] Y. Chen, P. Crawford and P. Hu: Catal. Lett. **119** (2007) 21.

[115] N. Hamada, S. Sawada and A. Oshiyama: Phys. Rev. Lett. **68** (1992) 1579.

[116] A. M. Cassell, J. A. Raymakers, J. Kong and H. Dai: J. Phys. Chem. B **103** (1999) 6484.

[117] H. M. Christen, A. A. Puretzky, H. Cui, K. Belay, P. H. Fleming, D. B. Geohegan, and D. H. Lowndes: Nano Lett. **4** (2004) 1939.

[118] H. Yoshida, T. Shimizu, T. Uchiyama, H. Kohno, Y. Homma and S. Takeda: Nano Lett. **9** (2009) 3810.

List of publications

[1] Systematic Morphology Changes of Gold Nanoparticles Supported on CeO_2 during CO Oxidation, T. Uchiyama, H. Yoshida, Y. Kuwauchi, S. Ichikawa, S. Shimada, M. Haruta and S. Takeda: Angew. Chem. Int. Ed. **50** (2011) 10157-10160.

[2] Correlation of catalytic activity with the morphology change of Au nanoparticles in gas, T. Uchiyama, H. Yoshida, N. Kamiuchi and S. Takeda: submitted to Surface Science.

[3] Revealing the heterogeneous contamination process in metal nanoparticulate catalysts in CO gas without purification by *in-situ* environmental transmission electron microscopy, T. Uchiyama, H. Yoshida, N. Kamiuchi, H. Kohno and S. Takeda: accepted for publication in Microscopy (2016).

[4] Atomic-Scale In-situ Observation of Carbon Nanotube Growth from Solid State Iron Carbide Nanoparticles, H. Yoshida, S. Takeda, T. Uchiyama, H. Kohno and Y. Homma: Nano Lett. **8** (2008) 2082-2086.

[5] Atomic-Scale Analysis on the Role of Molybdenum in Iron-Catalyzed Carbon Nanotube Growth, H. Yoshida, T. Shimizu, T. Uchiyama, H. Kohno, Y. Homma and S. Takeda: Nano Lett. **9** (2009) 3810-3815.

[6] An attempt to characterize phase Q: Noble gas, Raman spectroscopy and Transmission Electron Microscopy in Residues Prepared from the Allende Meteorite, J. Matsuda, K. Morishita, H.

Tsukamoto, C. Miyakawa, M. Nara, S. Amari, T. Uchiyama, S. Takeda: Geochimica et Cosmochimica Acta, **74** (2010) 5398-5409.